DTU Wind and Energy Systems

Modelling wake effects between wind turbines with varying hub heights

Author:
Ioannis Paraskevopoulos
DTU Wind-M-0759
August 2024

Author:
Ioannis Paraskevopoulos

Title:
Modelling wake effects between wind turbines with varying hub heights

DTU Wind-M-0759

ECTS: 45

Education: Master of Science

Supervisors:

Paul van der Laan
DTU Wind & Energy Systems

Simon Watson
TUDelft

Mikkel Kiilerich Østerlund
Vestas Wind Systems

Remarks:
This report is submitted as partial fulfillment of the requirements for graduation in the above education at the Technical University of Denmark.

DTU Wind & Energy Systems is a department of the Technical University of Denmark with a unique integration of research, education, innovation and public/private sector consulting in the field of wind energy. Our activities develop new opportunities and technology for the global and Danish exploitation of wind energy. Research focuses on key technical-scientific fields, which are central for the development, innovation and use of wind energy and provides the basis for advanced education at the education.

Technical University of Denmark
Department of Wind and Energy Systems
Frederiksborgvej 399
4000 Roskilde
Denmark
www.wind.dtu.dk

Modelling wake effects between wind turbines with varying hub heights

by

Ioannis Paraskevopoulos

to obtain the degrees of

Master of Science
in Wind Energy
at Technical University of Denmark

Master of Science
in Aerospace Engineering
at Delft University of Technology

To be defended on the 20th of September 2024

Supervisors:	Maarten Paul van der Laan	DTU
	Simon Watson	TU Delft
	Mikkel Kiilerich Østerlund	Vestas Wind Systems A/S
Defence committee:	Dominic von Terzi	TU Delft
	Richard Dwight	TU Delft
Start date:	November 1, 2023	
End date:	August 31, 2024	
Student numbers:	TU Delft:	5851025
	DTU:	s223597

An electronic version of this thesis is available at
`https://repository.tudelft.nl` and `https://findit.dtu.dk`

The code written for this thesis is partly available on *Github*

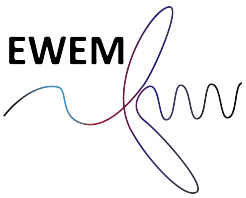

Abstract

The ever-increasing need for improving the energy yield in wind farms while minimising fatigue loads has created the need for exploring new concepts in the wind sector. One is the notion of wind farms with turbines of varying hub heights, often called vertically-staggered (VS) configurations. Multiple studies have demonstrated the potential benefits of such arrangements, yet the effect of erecting larger-scale wind turbines into an already existing control wind farm has not been explored. This concept has gained remarkable industrial attention, particularly in the German onshore market, as it simplifies the grid connection and land acquisition, among other benefits. Understanding the implications of vertical staggering on turbine performance is therefore essential. In addition, fast and accurate modelling of the inflow conditions modulated by the atmospheric boundary layer (ABL), is crucial in predicting the flow properties and energy yield in wind farms. A novel steady-state, RANS-based inflow model has recently been proposed, yet it lacks detailed validation. The present research aims to assess the reliability of that model in large wind farm flow simulations and subsequently apply it to identify flow patterns and power production characteristics in VS configurations representative of the German onshore wind standards through numerical simulations. RANS modelling combined with the actuator disk method in the PyWakeEllipSys software was employed to demonstrate that despite the inability of that inflow model to yield accurate prediction of the turbulence intensity, the computed velocity field is in fair agreement with LES results in conventionally neutral boundary layer conditions. This is evident, especially for deeper ABL cases. This study argues for the complexity of the flow caused by the collocation of different turbine scales in the investigated VS configurations. It is also highlighted that rotor overlap negatively impacts the power production of both turbine types in VS wind farms. Hence, it is suggested that optimal performance in VS setups can be achieved by minimising the rotor vertical overlap through appropriate adjustments of the hub height.

Contents

List of Figures

List of Tables

CHAPTER 1

Introduction

Wind energy has emerged as a crucial component in the global renewable energy agenda as a result of growing consciousness for global warming. The inflation from commodity price increases and the Russian invasion in Ukraine, have also caused turbulence in the global energy planning, emphasizing the necessity for renewables. To put into perspective, as much as 117 GW of wind power was installed in 2023 - a 50% increase compared to the year before [17]. Hence, the optimisation of the design, operation, maintenance and integration of wind turbine systems is profound.

An important aspect of wind farm flows is the wake effect. Wind turbine wakes are characterised by increased turbulence levels and decelerated mean flow compared to the unperturbed free stream, leading to amplified fatigue loads and power losses to downstream wind turbines respectively, with the latter ranging approximately from 10 to 20% [36]. Therefore, understanding the underlying mechanisms of wind turbine and wind farm wakes from a fluid mechanical perspective is of cardinal importance, in order to proceed with further optimisation.

In recent years, the rapid growth in computational capabilities has encouraged the use of computational fluid dynamics (CFD) for that purpose, predominantly Reynolds-Averaged Navier-Stokes (RANS) and Large Eddy Simulations (LES), for simulating wind turbine and wind farm wakes. The steady-state RANS approach is favourable for wind energy applications, since it is approximately three orders of magnitude faster than LES, as in van der Laan et al. [58].

Furthermore, the inflow conditions modulated by the atmospheric boundary layer (ABL), are crucial in wind turbine or wind farm wake studies. Reliable modelling of those conditions is therefore necessary. A number of 1D steady-state RANS-based atmospheric inflow models have initially been developed and implemented in van der Laan et al. [54]. Yet, these models can produce non-physical wake recovery when applied to a 3D wind farm domain. Subsequently, an improved model was proposed by van der Laan et al. [56], which may overcome this problem for tall ABLs, however it exhibits considerable shortcomings in shallow ABL cases. Finally, a novel inflow model has recently been proposed by van der Laan et al. [57], yet its efficiency in flow field predictions remains unknown, particularly in large wind farms. Therefore, a quantitative comparison to higher fidelity simulated data (e.g. LES) or field observations is necessary to obtain insights into its capabilities.

On the other hand, the ever-increasing need for improving the annual energy production (AEP) in wind farms while minimising fatigue loads has created the need for exploring new concepts, one of which is the notion of wind farms with turbines of varying hub heights, often denoted in the literature as vertically-staggered (VS) configurations. From a fluid mechanical perspective, alternating the hub height may minimise the wake overlap between consecutive turbines, thereby improving their performance and avoiding excessive fatigue loading. To date, several configurations have been studied, yet the effect of erecting larger-scale (i.e. rotor diameter and hub height) horizontal axis wind turbines (HAWT) than the already existing ones in a control wind farm has not been explored. In addition, as per the assessment by the industrial partner of the current project (Vestas Wind Systems A/S), there is a remarkable demand for such setups within the German onshore market.

1.1 State-of-the-art

The aim of the present section is two-fold; firstly to present and review latest research advancements in the field of wake modelling using CFD and analytical modelling as well as the effect of vertical staggering on the wakes. Secondly, this section aims to establish firm connections with common state-of-the-art practices employed in the industry.

1.1.1 Inflow modelling considerations

Wind farm simulations require apriori knowledge of the atmospheric inflow conditions; to that end, precursor simulations are typically employed for the calculation of ABL profiles, which are then introduced to the wind farm flow domain. In RANS, generating 1D steady-state ABL profiles has been found 3 to 4 orders of magnitude faster than their 3D counterparts, while the resulting profiles have been found almost identical, as indicated in van der Laan & Sørensen [55]. Thus, in the remainder of this report, 1D RANS-based, steady-state inflow models are reviewed and implemented.

The existing 1D RANS-based inflow models can be classified to atmospheric surface layer models (ASL) and ABL models. The former comprises models that reflect the structure of the ASL, occupying approximately the first 10% of the ABL. The simplest ASL inflow model is the analytical logarithmic profile, which assumes constant Reynolds stresses in the vertical direction and neglects Coriolis or thermal effects i.e. the ABL height is infinite in that case.

Analytical profiles such as the one described above, are inadequate for representing the ABL and are solely indicative of flow phenomena within the ASL. However, modern wind turbines tend to operate above the ASL. Even in relatively deep ABL cases (i.e. around 1000m), as for instance in Lanzilao & Meyers [25], the ASL covers about the first 100m above the ground. Yet, large-scale contemporary turbine towers often extend to higher altitudes, meaning that a substantial part of the rotor swept area may be subjected to the flow above the ASL, as in VS wind farms (refer to chapter 5), where this effect is

exaggerated. Therefore, reliable modelling of the full ABL is vital for understanding and optimising wind turbine performance.

State-of-the-art $k-\varepsilon$ ABL models in RANS can be categorized according to the way by which the ABL height is determined. Firstly, a widely used method comprises models that set the ABL height through a global turbulence length scale limiter (ABL-ℓ_{max}), as in Apsley and Castro [5], incorporated in the transport equations for turbulence dissipation (ε), while neglecting the turbulence production due to buoyancy. The approach proposed by van der Laan et al. [61], can model the neutral and stable ABL, accounting also for the effects of Coriolis-induced wind veer. A stable ABL (SBL), in particular, may be represented by reducing the maximum turbulence length scale, i.e. obtaining relatively shallower ABL. On the contrary, some issues are encountered in modelling convective ABL (CBL) conditions; although the profiles compare well with measurements within the ASL, the obtained ABL height is unphysically large and further modifications are required.

Nevertheless, the ABL-ℓ_{max} approach to set the ABL height may lead to unreasonable wake recovery when 3D wind farm domains are initialised with this model in wind farm simulations as shown by van der Laan et al. [60]. This is attributed to the use of a global turbulence length scale limiter (ℓ_{max}); that is, the implementation of a maximum turbulent length scale for the ABL profile should also be the case in the 3D wind farm domain, in order ensure consistency between the two. However, this may produce numerical solutions where the wakes do not recover downstream [56]. Furthermore, a relatively strong inversion at the top of ABL is implicitly set in the ABL-ℓ_{max} model, which can be problematic giving rise to numerical instabilities.

The model later proposed in the work of van der Laan et al. [56] namely ABL-θ, has been shown to mitigate the numerical instability issue, since the turbulence length scale limiter (ℓ_{max}) is not used. Instead, it relies on a prescribed analytical expression of the potential temperature, as function of the inversion strength and ABL height, similar to the formulation of Rampanelli & Zardi [38]. This expression is incorporated into the turbulent buoyancy sink/source term in the turbulence transport equations, which contrary to the ABL-ℓ_{max} model, is non-zero. Explicitly setting the inversion strength in the model may therefore eliminate, to some extent, the associated numerical problems discussed previously. This model is intended to model conventionally neutral ABL (CNBL), i.e. a neutral ABL developed against a stably stratified free atmosphere, as defined in Zilitinkevich & Esau [72]. However, a reasonable combination of the input parameters (i.e. inversion height, inversion strength) should be chosen, particularly for shallow ABL cases, since an unphysical double ABL height profile may be obtained otherwise, as demonstrated in van der Laan et al. [57].

Eventually, ABL-N, a novel ABL model has recently been derived by van der Laan et al. [57]. The ABL height is now defined through a constant Brunt-Väisälä frequency (N) and thus a constant potential temperature gradient therein, contrary to the ABL-θ model

where the potential temperature gradient varies with height. The ABL-N suppresses the double ABL height behaviour of the ABL-θ, since the inversion height is not an explicit input to the model. Besides, a global turbulence length scale limiter is not required in the 3D wind farm domain, as in the case of ABL-ℓ_{max}, hence the non-physical behaviour of the wakes may be avoided.

A comparison to LES results for a single wake, subjected to CNBL and stable ABL (SBL) conditions in van der Laan et al. [57] has shown that the ABL-N model resembles the effect of a shallow SBL better than the ABL-ℓ_{max} and ABL-θ. However, although the work mentioned above analysed the effectiveness of the model in single wake conditions, its capabilities in large-scale wind farm simulations have not been yet assessed. Therefore, analysis of the predicted velocity and turbulence fields at the wakes between wind turbines in realistic wind farm setups should be carried out, in order to obtain further insights into the capabilities and limitations of the model. This can be realisable through quantitative comparisons with higher fidelity simulated data e.g. LES, or field observations.

1.1.2 Implications of vertical-staggering

The AEP and turbine loads are two of the cardinal design and operation drivers of wind farms. These are highly affected by aerodynamics, in particular wakes, and can be controlled through proper layout optimization. Horizontal staggering has been traditionally one of the most common wind farm layout optimisation techniques aiming to minimise wake-induced losses and fatigue loads. Extensive research efforts experimentally (e.g. by Markfort et al. [31] and Chamorro et al. [11]) and numerically (e.g. by Porte-Agel et al. [36] and Stevens et al. [46]) have been undertaken, in order to understand the flow phenomena occurring in such configurations. On the other hand, vertical staggering has emerged as a relatively new advancement with increasing academic and industrial interest, within the context of layout optimisation. In the following paragraphs, the state-of-the-art understanding and application of vertical staggering and its fluid mechanical implications is reviewed.

The work of Herbert-Acero et al. [20] was one of the first studies highlighting the benefits of vertical-staggering. They used optimization algorithms in a horizontally aligned row of turbines to prove the minimization of wake losses owing to the hub height variation. Similar deductions have been made in the experimental study by Vested et al.[66] using stereographic PIV. In particular, a 25% percent increase in the power output has been witnessed in the last row of an alternating hub height setup, with the hub height of the tall wind turbines being 50% larger than the standard ones.

Likewise, Vasel-Be-Hagh and Archer[64] carried out an AEP analysis on a realistic wind farm layout, namely the Lillgrund wind farm in Sweden, varying the hub heights of consecutive rows of turbines. They employed a greedy search algorithm to optimise the hub heights and the results demonstrated that vertical-staggering may boost the AEP by 2% in some cases. Zhang et al. [71] estimated the effect of vertical staggering on

the different regions of a wind farm by means of LES simulations. That study suggests that the entrance region, i.e. the first couple of rows, is highly benefited by the varied hub heights, recovering up to 20% of the aerodynamic power losses that would occur in a vertically-aligned setup. Conversely, vertical staggering is not as favourable in the fully-developed region of the wind farm; that is, in some cases even lower power production has been recorded than the standard layout. They attribute this feature to diminished performance of the short turbines, since downward kinetic energy fluxes responsible for wake recovery are negatively impacted by the low kinetic energy wakes generated by the tall turbines. In other words, the wakes of the tall turbines block the momentum diffusion from the more energetic unperturbed flow above the wind farm towards the wakes of the short turbines.

In addition, several studies demonstrate that the effects of vertical staggering on wind farm AEP are correlated to other parameters. Zhang et al.[71] investigated the variations of the average power with respect to turbine spacing, rotor diameter and hub height difference. Firstly, the benefits of VS configurations are more pronounced for offshore cases where the streamwise distance between consecutive wind turbines is small, namely less than 5 rotor diameters and the surface roughness is minimal. On the contrary, the spanwise spacing has insignificant influence on the performance of turbines in the VS setup. Furthermore, consistently to Herbert-Acero et al. [20] and Vasel-be-Hagh [64], it has been mentioned that when the hub height difference between consecutive rows of turbines is at its maximum, the gain in power production is maximised, while relatively smaller rotor diameters can make such setup more feasible. From a fluid mechanical perspective, two competing effects are identified; reducing the hub height of downstream machines would allow a larger fraction of the rotor area to perceive the unperturbed flow, yet the wind speed in smaller altitudes is lower due to shear. Nevertheless, Herbert-Acero et al. [20] highlighted recovery in terms of aerodynamic power losses up to roughly 24% when the hub heights of the two layers of turbines are at their maximum difference, owing to diminished rotor overlap.

1.1.3 Projections to the German onshore wind market

According to the industrial partner of the present work, there is a high demand for VS wind farms within the German onshore wind market in the form of erecting new turbines in already existing wind farms. This may simplify challenges not only related to fluid mechanics but also associated with grid connection and land leasing, as the already existing ones may be exploited. That market is particularly interested in installing larger-scale wind turbines i.e. both in rotor size and hub height in already existing wind farms; the latter can be beneficial, since taller turbines perceive higher wind speeds and can entrain more energy from the undisturbed flow, as discussed in Vested et al.[66]. Eventually, the streamwise spacing in such sites is typically restricted to less than 5 rotor diameters.

It has to be noted that all the abovementioned studies reviewed in subsection 1.1.2 use

identical rotors for the tall and short wind turbines. In addition, they solely vary the hub heights of downstream wind turbines without comparing the results to a fixed reference wind farm layout. This may be useful for new wind farm designs, yet it is not relevant for the German onshore market, where wind turbines are already commissioned.

To date very few studies have provided insights on the effects of vertical staggering with respect to a control wind farm; Chatterjee and Peet [13] investigated the installation of small-scale HAWT into a fixed layout, whereas Xie et al. [70] explored the potential of collocating short VAWT within a reference wind farm consisted of large-scale HAWT, both using LES simulations.

The latter study reports that in the VS setup, comprising 20 small VAWTs around each large-scale HAWT, a 10% increase in mean power of the large HAWTs is recorded compared to the control wind farm. The former research documents that in absence of geometrical overlap between the two layers of turbines, a 4% power increase was captured for the small HAWTs compared to the control wind farm, whereas partial geometrical overlap leads to a corresponding 9% drop. Nevertheless, the numerical setup of that study introduces significant artificial blockage with the blockage ratio being in the order of 10%. The associated acceleration of the flow around and above the wind farm causes faster wake recovery, hence these numbers may not be fully relied on. Both studies, however, suggest that augmented turbulence attributed to the multi-scale configuration has considerable implications predominantly to the wake recovery of the large-scale turbines and the associated power fluctuations.

Eventually, the effect of adding HAWT with larger rotor and hub height into a realistic control wind farm remains unknown. Investigating the topic from an aerodynamical perspective may improve the current understanding around vertical staggering. It can also provide useful insights tailored to the onshore wind market in Germany, which is characterised by tight turbine interspacing, emphasising the relevance of such arrangements.

1.1.4 Implementation of analytical wake modelling

Fast and reliable modelling is required for industrial applications. Engineering wake models, i.e. analytical expressions for the wake-induced velocity deficits and added turbulence, can be employed for fast calculations of wind farm flows [18]. The accuracy of three engineering wake models in terms of wind farm power production has been assessed in Wang et al. [67], namely the Larsen [27], PARK [24] and Bastankhah [6] models, for constant and variable hub height wind farms. It has been found that with proper calibration of the roughness length, the PARK model can predict well the performance of the turbines in the VS case, whereas the Bastankhah model overpredicts the power output particularly for the onshore wind farm. By comparison, the Larsen model also yields fairly accurate results and it performed better in the case of variable hub height wind farms compared to the regular ones of constant hub height. Other studies have

implemented the Jensen model [23] to account for wake losses in optimisation algorithms of VS layouts as in Chen et al.[14] and Chen et al. [15].

Nevertheless, the effectiveness of engineering wake models in VS wind farms, representative of German sites has not been explored. Quantifying the deviations between those models and higher-fidelity approaches, as for instance CFD, in such setups may improve the current understanding and enhance the use of analytical modelling with higher confidence.

1.2 Scope & research questions

The present study is confined to focus majorly on the aerodynamical implications of the concept of vertical staggering. Technical challenges related to loads, structures, materials, control or system dynamics are neglected. Likewise, further challenges related to logistics and noise of the tall turbines are equally important for the feasibility of realising such configurations, yet they are as well overlooked for the purposes of the present study.

The following research questions (RQ) arise from the literature review, presented in the preceding section.

RQ1: *To what extent can the newly developed 1D steady-state ABL-N inflow model be used for modelling wake effects between turbines in large-scale wind farm flow simulations?*

- How does the velocity and turbulence intensity field predicted by ABL-N compare with LES-simulated results for different ABL heights in such setups?

RQ2: *What is the effect of adding larger turbines both in rotor size and hub height on the already existing wind turbines of a wind farm indicative of the German onshore sites?*

- How does the power production vary between the control wind farm and the VS wind farm for different hub heights of the tall turbines?
- How does the turbulence field vary between the control wind farm and the VS wind farm for different hub heights of the tall turbines?
- What are the differences in wake recovery and convection downstream?

1.3 Report outline

The remainder of the present report is organised into five chapters. In chapter 2 the theoretical background required for the present work is presented, focusing on two major topics. Firstly, the fundamental characteristics of the ABL including its vertical morphology and the underlying physical mechanisms in such flows are discussed.

Thereafter, the analysis focuses on a special type of ABL, the so-called conventionally neutral boundary layer (CNBL), which is used in the assessment of chapter 4. Secondly, the main flow mechanisms observed in wind turbine wakes are analysed, identifying different regions therein and establishing the effects of atmospheric stability. Chapter 3 presents the methodology employed for the numerical analysis, including the governing equations, the approach for representing the rotor forcing in the computational domain, and the controlled variables associated with the numerical grid. The first research question (RQ1) is dealt with through a comparative assessment performed in chapter 4. It entails the comparison of 1D atmospheric inflow profiles, single wake and wind farm wakes obtained using the ABL-N model against higher-fidelity LES simulated data for a CNBL case. Subsequently, the analysis and main findings related to answering the second research question (RQ2) are presented in chapter 5. The setup chosen is first demonstrated, followed by the characterisation of key flow phenomena occurring in VS configurations. Eventually, a comparison of the energy yield, focused on the small turbines, is performed. Ultimately, chapter 6 concludes the current report, summarising the main outcomes of the study and giving suggestions for further research on the topic.

CHAPTER 2
Theoretical background

2.1 The atmospheric boundary layer

Boundary layer is the flow regime in the close vicinity of a solid boundary that directly influences the flow through drag forces. The atmospheric boundary layer (ABL), in particular, is modulated in atmospheric flows due to the presence of the ground or the sea surface and its responsiveness to surface forcing corresponds to a timescale of up to approximately one hour [47]. Changing weather conditions and solar activity results in temporal and spatial ABL height variability as depicted in Figure 2.1. Contemporary wind turbines operate predominantly within the ABL, therefore understanding the underlying mechanisms in such flows and their impact on turbine operation and performance is of major importance.

ABL flows are known to be highly complex owing to their intrinsic three-dimensional, turbulent nature. Wind shear, which generates mechanical turbulence, and thermal effects, which either suppress or enhance vertical motions of air particles, are the two prevailing mechanisms of atmospheric turbulence.

Typically, the ABL takes up the bottom 10-20% of the earth's troposphere. The vertical structure of the ABL comprises two main regions, as seen in Figure 2.2. The atmospheric surface layer (ASL) occupies the lower part of the ABL, namely about the first 10% of its total height. It is primarily governed by the presence of the earth's surface, whereas Coriolis forces associated with the earth's rotation are negligible. Strong velocity and temperature gradients are therefore present, although turbulent fluxes and stresses are uniform with height, i.e. the variations are less than 10% [47].

It is worth-mentioning that modern wind turbines have significantly grown in size (i.e. both in hub height and rotor size), therefore they often operate in the region above the ASL. In that flow regime, surface friction is still important, yet the effect of Coriolis forces is significant, causing variations in wind direction along the vertical direction. This effect is also referred to as Coriolis-induced wind veer.

Above the ABL lies the free atmosphere where the wind is not affected by the presence of the ground, hence the flow is unidirectional in the absence of turbulence. The ABL and the free atmosphere are separated by another non-turbulent, very stably-stratified layer, called capping inversion or entrainment zone depending on the part of the day.

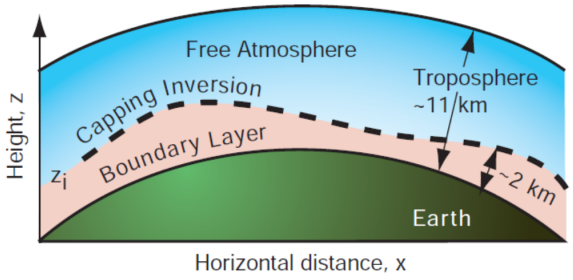

Figure 2.1: Schematic illustrating the vertical structure of the earth's troposphere; The ABL, whose height is characterised by temporal and spatial variability, occupies the first 10-20% of the total troposphere height and is separated from the free atmosphere by a capping inversion. Reproduced from Stull [48].

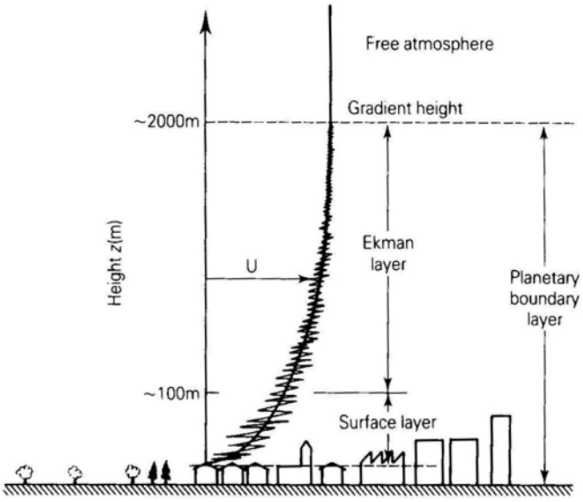

Figure 2.2: 2D schematic illustrating the vertical structure of a typical ABL. Reproduced from Tavner et al. [49].

2.1.1 Effect of atmospheric stability

Atmospheric thermal stability has a significant influence on the formation of the ABL, through the associated buoyancy forces. In the remainder of the present chapter, only static stability is reviewed, i.e. neglecting the contribution of wind shear in the turbulence budget. Thermal effects can suppress or enhance vertical motions of air particles and as such, they regulate the atmospheric turbulence levels in the ABL.

The traditional atmospheric stability classification relies purely on surface heating or cooling. Hence, three different ABL types can be distinguished, based on that criterion, namely neutral (NBL), stable (SBL) and unstable or convective (CBL) boundary layers.

Initially, NBLs are the simplest types of ABLs, characterised by nearly zero heat fluxes at the surface and a constant potential temperature with height. Buoyancy forces are

absent in those cases, therefore vertical motions of air parcels are neither enhanced nor suppressed. NBLs are observed shortly during the transition after sunset or in cloudy weather conditions [2]. Similarly, ABLs developed over the sea surface can also be assumed neutral, given that the heat fluxes are substantially smaller than those onshore.

Likewise, CBLs are developed during the daytime, when the sun heats the surface, producing positive heat fluxes. The potential temperature decreases with height, implying that in such cases, forces due to buoyancy enhance vertical motions, thereby giving rise to turbulent mixing. CBLs are mostly found over land, yet they are not commonly observed offshore.

By comparison, the formation of SBL is more frequent during nighttime, where the surface is cooler, triggering negative heat fluxes. Colder air underlies warmer air and as such, buoyancy acts as a restoring force when air particles are vertically displaced from their initial position. Consequently, in SBL turbulent motions are suppressed or non-existent. SBLs are typically shallower than CBL or NBL, where wind shear and veer are more pronounced.

A comparative illustration of the ASL profile in statically neutral, stable and convective boundary layers is shown in Figure 2.3. In the CBL (pink line), the presence of strong momentum mixing due to turbulence creates a more rapid wind speed change with height above the ground. On the contrary, the field in SBL (blue line) cannot be homogenised due to the absence of turbulence and thus diminished downward momentum transport is exhibited. NBL lies in between the two previously mentioned ABL types.

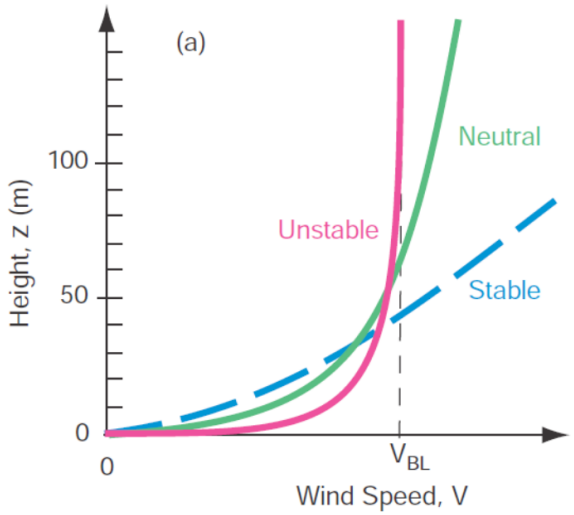

Figure 2.3: Vertical wind speed profile of the ASL (i.e. first 10%) in statically stable (SBL), unstable or convective (CBL) and neutral (NBL) atmospheric conditions. Reproduced from Stull [48].

2.1.2 Conventionally neutral boundary layer

In the preceding discussion, the traditional categorisation of ABLs according to the surface heat flux at the surface was presented. Now, the discussion is extended to additional subdivisions of the ABL, specifically for statically neutral conditions.

The NBL has been further classified based on the thermal stratification of the free atmosphere below which it develops. Zilitinkevich & Essau [72] distinguished two types of NBLs; the truly neutral ABL and the conventionally neutral ABL (CNBL), formed against a neutrally and stably stratified free atmosphere respectively.

In fact, the truly neutral boundary layer type is not encountered in real-life conditions and is therefore considered an idealised case [21]. Most NBL cases are capped by an inversion layer (capping inversion) that separates the turbulent ABL from the non-turbulent, stably stratified free atmosphere. Hence, they are of the CNBL type.

A representation of the vertical structure of the CNBL and the associated force balances are demonstrated in Figure 2.4. Firstly, the neutral ABL is located close to the ground, where the velocity increases with height. The diminishing effect of Coriolis towards the solid surface causes increasing rotation of the wind towards the direction of the pressure gradient.

Above the neutral ABL lies the stably stratified free atmosphere reflected by a constant constant lapse rate i.e., a constant potential temperature gradient, and the absence of turbulence. This flow regime is governed by a balance between the horizontal pressure

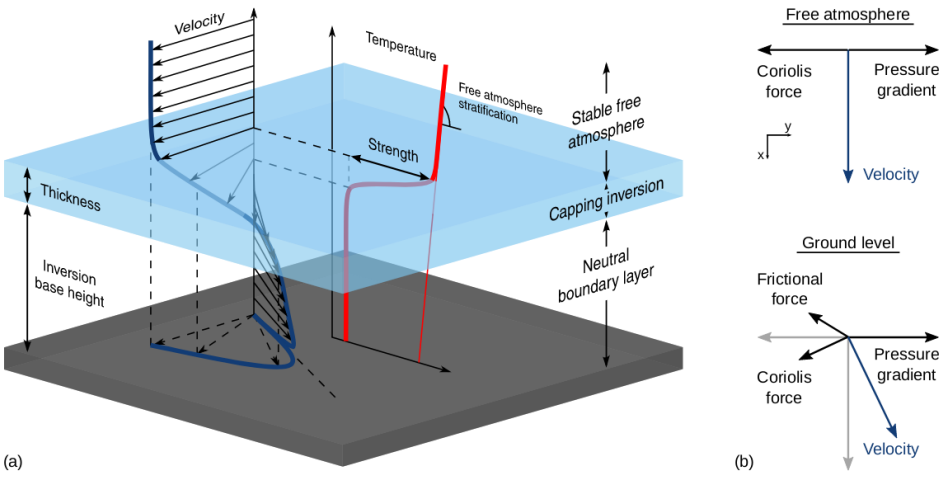

Figure 2.4: Schematic of the vertical structure in CNBL (left) and the associated force balances within the ABL and at the free atmosphere above (right). Reproduced from Allaerts [2].

gradient and Coriolis forces resulting in a unidirectional flow field driven by the geostrophic wind speed (G).

In between the free atmosphere and the turbulent ABL lies the capping inversion or inversion layer; a stably-stratified layer of thickness Δh, where a rapid potential temperature increase, referred to as inversion strength ($\Delta\theta$), is observed. A clear representation of the potential temperature profile in the capping inversion and its features is also shown in Figure 2.5, in correspondence with the formulation of Rampanelli & Zardi [38].

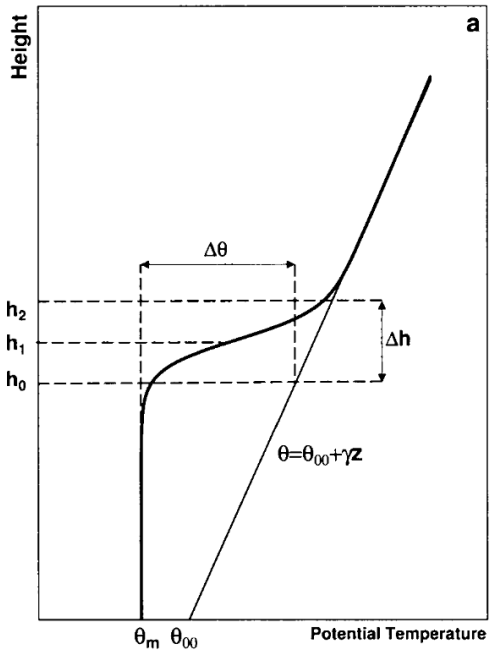

Figure 2.5: Schematic of the potential temperature along the vertical direction in CNBL. The capping inversion strength and thickness are denoted with $\Delta\theta$ and Δh respectively. Reproduced from Rampanelli & Zardi [38].

2.2 Wind turbine wakes in atmospheric turbulence

The energy extraction from the wind by a wind turbine is followed by the formation of the so-called wake in close downstream distance. Wakes are characterised by decelerated mean flow and augmented turbulence levels with respect to the free stream, inducing power losses and increasing fatigue loads to downstream turbines respectively. Their turbulent nature and interactions with the turbulent ABL, further complicate the occuring flow phenomena. Understanding the aerodynamical aspects of such flows is essential to optimise the performance of contemporary wind systems. Therefore, the present section provides a brief overview of the wake flow properties observed in wind turbine and wind farm scales.

The existence of a wind tubine influences the flow field both upstream and downstream of the turbine. The former is also called induction region, where a decrease in wind speed of the incoming flow is observed before it reaches the turbine. In contrast, wind turbine wakes are developed in the latter regime, extending between 10 to 20 rotor diameters downstream of the turbine depending on several factors such as atmospheric stability, ambient turbulence intensity and surface roughness[4], [69]. Beyond that, the flow has recovered to its initial undisturbed state.

Two main regions can be identified in wind turbine wakes, namely the near-wake and the far-wake [65], visualised in Figure 2.6. The near-wake takes up about 2-4 rotor diameters downstream of the wind turbine depending on the ambient turbulence intensity, the mechanical shear created at the turbine tips and the tip speed ratio [35]. This flow regime, being in immediate proximity to the turbine, is dominated by the characteristics of the rotor geometry - mainly the blades but also the hub and the nacelle. Perhaps the most significant feature of the near wake is the helical vortex system (see Figure 2.7) shed by the tip and the root of the blade, due to the radial variation of the force field.

However, the turbine interspacing in the streamwise direction is typically higher than 3 rotor diameters in standard wind farms, therefore the turbines are almost always located at the far wake of upstream ones. In the far wake, the flow breaks down to turbulence

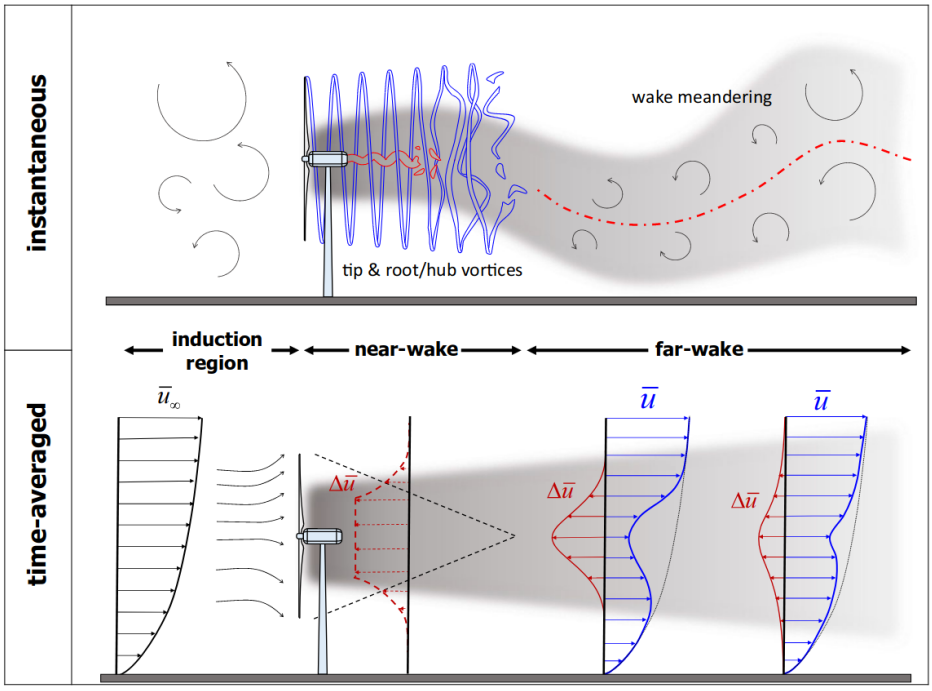

Figure 2.6: Schematic of the instantaneous (upper) and time-averaged flow characteristics around a wind turbine. Three distinct regions can be identified, namely the induction region, the near-wake and the far-wake. Reproduced from Porté-Agel et al. [35].

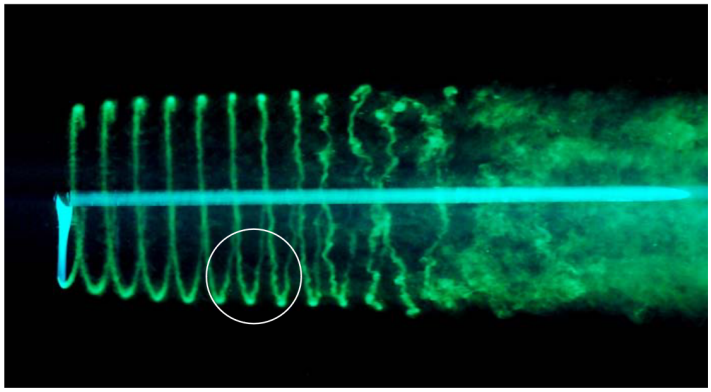

Figure 2.7: Visualisation of the helical vortex system downstream of a one-bladed wind turbine. Reproduced from Leweke et al. [30].

and, contrary to the near-wake, it is less affected by the rotor geometry. In idealised cases (i.e. in absence of surface roughness and wind shear) the velocity deficit is believed to be a Gaussian, yet that is not always representative when wind shear and surface roughness are accounted for. Turbulence intensity is higher than in the incoming flow and turbulent momentum fluxes, reflecting the absorption of the outer flow towards the wake region, are more pronounced close to the upper tip. The latter is attributed to the mechanical turbulence generated at that region as a result of shear.

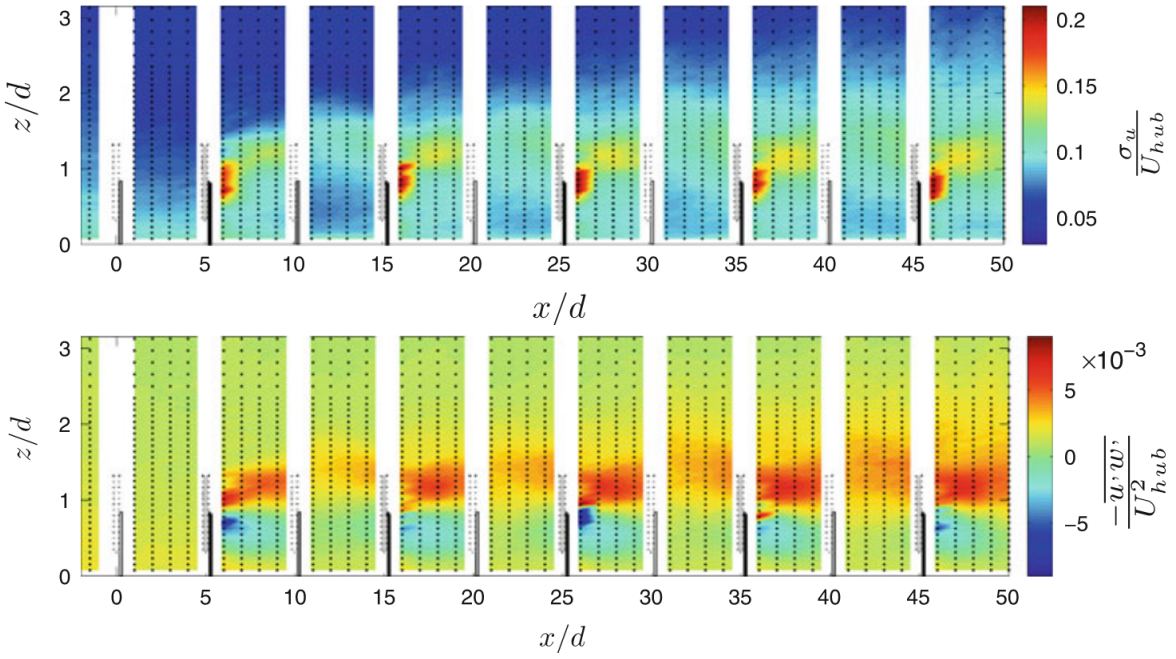

Figure 2.8: Distribution of streamwise turbulence intensity (upper) and normalised turbulent momentum transport in the vertical direction (lower) in a row of wind turbines. Reproduced from Chamorro et al. [11].

2.2.1 Wake effects in wind farms

The discussion regarding the anatomy of the wakes is now extended to a wind farm level, where more complex flow phenomena may be encountered. In particular, the flow field around a wind farm can be separated into five distinct regions; **(a)** the induction region, **(b)** the entrance and development region, **(c)** the fully-developed region, **(d)** the exit region and ultimately **(e)** the wind farm wake in correspondence with Figure 2.9. The key flow features for each of the abovementioned regions are summarised below.

Firstly, contrary to the case of a stand-alone wind turbine, the presence of a wind farm is sensed by the incoming flow several kilometres upwind of the first row of turbines. As a result, the flow decelerates and is forced to flow above and around the wind farm. This is called the induction region and its distinct slow down of the wind is also referred to as blockage. It is therefore straightforward that blockage effects have implications on the power production of the first few turbine rows.

The energy extraction by the wind turbines starts at the so-called entrance region of the wind farm. The formation of the first turbine wakes is represented by further decreases in flow momentum. As these turbine wakes propagate further downstream, they expand laterally and vertically and they overlap with other wakes. For that reason, the flow transitions from a single turbine wake scale to a more universal wind farm level. This transition is characterised by the formation of an internal boundary layer, which is highly heterogeneous at a wind turbine level, but it shows greater coherence on the top, as shown in Figure 2.9.

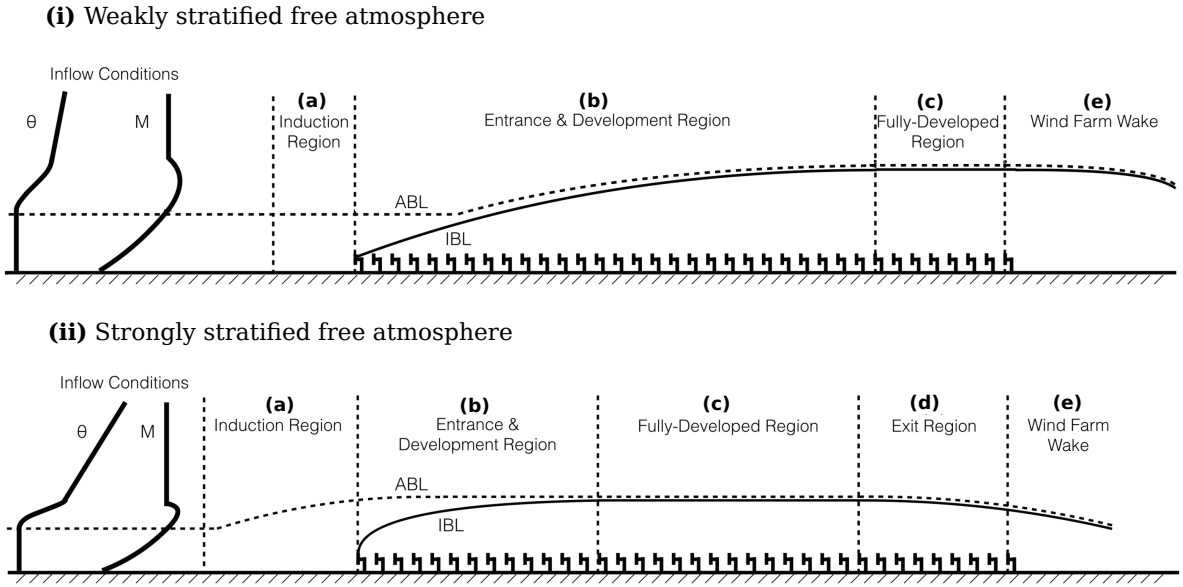

Figure 2.9: Schematic of the different flow regions in a large-scale wind farm subjected to deep ABL with weakly-stratified free atmosphere **(i)** and shallow ABL with strongly-stratified free atmosphere **(ii)**. Adjusted from [68].

Adjacent to the entrance and development region lies the fully-developed region. This regime is modulated at large downstream distances from the entrance region, and for that reason is not often encountered in reality. Nevertheless, insights have been obtained in some numerical studies, where infinitely large wind farms are investigated (e.g., [1]). The most important feature within that region is that the flow has - on average - reached an equilibrium state i.e., it has adapted to the presence of the wind turbines, whilst the energy extraction it undergoes is balanced by the downward momentum transport from the undisturbed flow lying above.

Furthermore, in the wind farm wake region the flow recovers from that energy extraction stemming from the presence of multiple turbines. Wind farm wakes can typically extend several tens of kilometres downstream of the wind farm until the flow has adequately recovered to its initial state. Their importance lies in scenarios where multiple wind farms are placed tightly, as interactions with neighbouring wind farms may potentially be triggered.

Eventually, it has to be mentioned that the extent of each region in wind farm flows depends on various factors e.g., the wind farm configuration (i.e. layout, size, interspacing), the performance of the installed turbines (thrust forces) and the stratification of the ABL and the free-atmosphere. The latter effect is discussed below.

2.2.2 Wind farms subjected to non-neutral atmospheric conditions

Thermal stratification of the ABL is a key parameter affecting the flow features within the ABL. As an extent, thermally stratified ABLs may have detrimental influence on power production, since the performance of individual turbines is highly related to the incoming flow characteristics.

For instance, as seen in Figure 2.3, the wind shear and mean wind speed at hub height in the ASL region are predominantly dependent on the atmospheric stability, and thus the wind power potential varies in different atmospheric conditions. Likewise, atmospheric turbulence, regulated by thermal effects, is related to wake recovery; it has been found that wind turbine wakes subjected to CBL recover faster than in SBL or NBL scenarios, due to higher ambient turbulence intensities[19]. Consequently, power losses of downstream turbines are less pronounced in such cases. Conversely in SBL, where relatively lower ambient turbulence intensity is witnessed, turbulent mixing is suppressed and thus wake-induced losses are amplified.

Thermal stratification of the free atmosphere is another important factor in wind farm aerodynamics and power production. The example of a CNBL depicted in Figure 2.9 can be again considered. In the previous subsection, it was mentioned that the presence of the wind farm induces an upward flow deflection. On the other hand, the free atmosphere lying above tends to confine this upward motion limiting the energy entrainment from

above. Particularly in shallow CNBLs with strongly stratified free atmosphere, these two competing effects can trigger substantial alternation of the flow.

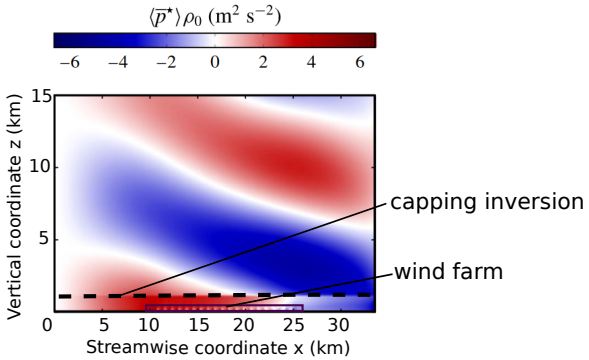

Figure 2.10: Pressure field (temporally and spatially averaged) indicative of gravity waves. Dashed line: capping inversion height; Rectangle: wind farm location. Adjusted from Allaerts & Meyers [3].

Perhaps the most striking phenomenon created due to the interaction of the highly turbulent turbine wakes and the non-turbulent free atmosphere is called gravity waves. Gravity waves exhibit pressure fluctuations (see Figure 2.10) stemming from buoyancy oscillations. Two main implications on wind turbine performance are recorded; firstly, more pronounced blockage effects (i.e. flow deceleration) are witnessed at the induction region, thereby reducing power production of the first few rows of turbines. Secondly, the propagation of gravity waves downstream leads to a speed-up region at the exit of the wind farm, featuring improved wind turbine performance. The exit region can be seen in Figure 2.9 (lower graph).

2.3 Summary

In the present chapter, a brief theoretical background is established. The complex physics governing ABL flows was first presented. The different regions in atmospheric flows were identified and the effect of temperature on the vertical structure and the convection mechanisms of the ABL were highlighted. Then, the review focused on a particular type of ABL and its intricacies; the so-called conventionally neutral boundary layer (CNBL).

As a second objective, the current chapter provided a fundamental overview of wake aerodynamics. The flow properties encountered in regions upstream and downstream of stand-alone wind turbines were initially outlined. The discussion was then extended to wind farm scales where the cumulative effect of wake interactions compounds more complex flow phenomena. Subsequently, projections were made to the complex interaction between wind turbine wakes and the turbulent ABL, in particular for non-neutral atmospheric conditions. The importance of thermal stratification of not only the ABL

itself but also the free atmosphere was unpacked. The chapter closed by introducing the so-called gravity waves and their implications on power production.

CHAPTER 3
Methodology

3.1 Flow solver

For the purposes of the present work, PyWakeEllipSys [16], the in-house CFD code of DTU, suited for modelling wind farm flows is employed. It is based on the Ellipsys finite-volume solver developed by Michelsen [32] and Sørensen [44]. The Navier-Stokes equations are solved with the SIMPLE algorithm [33], and the variables are computed at the cell centres. In order to avoid velocity-pressure decoupling, a Rhie–Chow algorithm [39] is employed. The discretisation of convective terms is performed with the QUICK scheme [29] implemented in EllipSys. That solver is coupled with a Python framework for convenient configuration and automation. It also enables multi-core parallel computations, therefore the cluster of DTU Wind and Energy systems *Sophia* is utilised in order to accelerate the numerical analysis.

3.2 Governing equations

3.2.1 RANS modelling

Wind farm flows can be described by the Navier-Stokes equations, which mathematically represent the conservation of mass and momentum. Assuming incompressible flow, (i.e. constant air density ρ), due to low Mach numbers characterising wind farm flows, the aforementioned equations in tensor notation read,

$$\frac{\partial u_i}{\partial x_i} = 0 \tag{3.1}$$

$$\frac{\partial u_i}{\partial t} + u_j \frac{\partial u_i}{\partial x_j} = -\frac{1}{\rho}\frac{\partial p_i}{\partial x_i} + \nu \frac{\partial^2 u_i}{\partial x_j \partial x_j} + f_i \tag{3.2}$$

Wherein, i is the index corresponding to cartesian coordinates (x, y, z), u, p, f represent the velocity, pressure and body forces of the flow field respectively, while $\nu = \mu/\rho$ is the kinematic viscosity and ρ, μ reflect the density and dynamic viscosity of the fluid. The left hand side (LHS) comprises two terms; the first term represents the temporal acceleration of the fluid along the i-direction, while the second term reflects the spatial or

convective acceleration. On the right hand side (RHS), pressure forces, viscous dissipation and body forces are accounted for by the first, second and third term respectively.

Solving the Navier-Stokes equations analytically has only been feasible for a very limited range of fluid flows where major assumptions have been considered (i.e. laminar flows), due to the non-linear nature of the convective term. Thus, reverting to numerical techniques, namely CFD, to find solutions to the Navier-Stokes in more complex flow cases, where turbulence should be accounted for, has been a common approach.

DNS is the most accurate but also computationally expensive approach, fully resolving all turbulence scales, yet the available resources for the purposes of the current work are not sufficient to adopt the calculations. LES requires less computational power, as it replaces the resolution of the smallest turbulent structures with sub-grid scale modelling, contrary to DNS. RANS is the cheapest numerical approach that models the full turbulence spectrum and it is employed in the present investigation. While LES may provide results with higher accuracy, the computational time is still prohibitively large, particularly for multiple turbine simulations. To put into perspective, LES has been found roughly three orders of magnitude more computationally intensive than RANS in van der Laan et al. [58] for a single turbine simulation. Thus, wind farm simulations may be unfeasible given the timeline of the project.

The basis of Reynolds-Averaged Navier-Stokes (RANS) equations is the Reynolds decomposition, according to which the velocity and pressure fields can be decomposed into a mean and a fluctuating component, i.e. $u_i = \overline{u_i} + u_i'$, $p_i = \overline{p_i} + p_i'$. Applying Reynolds decomposition to (3.1), (3.2) yields

$$\frac{\partial \overline{u_i}}{\partial x_i} = 0 \tag{3.3}$$

$$\frac{\partial \overline{u_i}}{\partial t} + \overline{u_j}\frac{\partial \overline{u_i}}{\partial x_j} = -\frac{1}{\rho}\frac{\partial \overline{p_i}}{\partial x_i} + \nu\frac{\partial^2 \overline{u_i}}{\partial x_j \partial x_j} - \frac{\partial}{\partial x_i}(\overline{u_i' u_j'}) + \overline{f_i} \tag{3.4}$$

For the remainder of the report the following two assumptions will be made. Firstly, the flow will be assumed steady i.e. $\partial/\partial t = 0$, in order to reduce the number of independent variables in the problem, thereby saving computational time. Secondly, due to the high diameter-based Reynolds number representative of wind energy applications, the flow may be considered turbulence-dominated, hence the viscous term can be neglected. The final form of the RANS equations then reads,

$$\frac{\partial \overline{u_i}}{\partial x_i} = 0 \tag{3.5}$$

$$\overline{u_j}\frac{\partial \overline{u_i}}{\partial x_j} = -\frac{1}{\rho}\frac{\partial \overline{p_i}}{\partial x_i} - \frac{\partial}{\partial x_i}(\overline{u_i' u_j'}) + \overline{f_i} \tag{3.6}$$

3.2.2 Turbulence closure

The additional term $\frac{\partial}{\partial x_i}(\overline{u_i' u_j'})$, also known as Reynolds stresses, arising by averaging the convective acceleration introduces six new unknowns which in combination with pressure and velocity result to a total of 10 quantities to be determined. However, the number of variables that have to be specified exceed the number of equations available, namely 10 unknowns with only four equations (3.5), (3.6). Therefore, the new quantities stemming from the convective term have to be modelled. This is also referred to as the turbulence closure problem.

The ultimate objective is to obtain additional expressions for the Reynolds stresses and close the system of equations. In RANS a straightforward approach in order to fulfill this objective is to employ the Boussinesq hypothesis [10], where a linear relation is assumed between the Reynolds stresses and the mean strain-rate tensor,

$$\overline{u_i' u_j'} = \frac{2}{3}k\delta_{ij} - 2\nu_T S_{ij}, \qquad S_{ij} = \frac{1}{2}\left(\frac{\partial \overline{u_i}}{\partial x_j} + \frac{\partial \overline{u_j}}{\partial x_i}\right) \tag{3.7}$$

wherein $k = \frac{1}{2}(\overline{u_i' u_i'})$ is the turbulence kinetic energy (TKE) defined as half the trace of the Reynolds stress tensor, representing the mean kinetic energy of the fluctuating velocity field. Note that in the remainder of the report TKE and k may be used interchangeably. Furthermore, δ_{ij} is the Kronecker delta, S_{ij} is the mean strain-rate tensor and finally ν_T is the eddy viscosity.

The latter is a proportionality factor, which describes the energy transfer due to turbulence. In the present work, a two-equation $k-\varepsilon$ [28] turbulence model is employed (where ε reflects the dissipation of k) to model ν_T,

$$\nu_T = C_\mu f_P \frac{k^2}{\varepsilon} \tag{3.8}$$

wherein $C_\mu = 0.03$ is a model constant, and f_P is a scalar function used as an eddy viscosity limiter in flow regions where high velocity gradients are witnessed, such as in a wind turbine wake [58]. Furthermore, k and ε may be determined by the corresponding transport equations, which respectively read,

$$\frac{Dk}{Dt} = \frac{\partial}{\partial x_j}\left(\frac{\nu_T}{\sigma_k}\frac{\partial k}{\partial x_j}\right) + \mathcal{P} - \varepsilon + \mathcal{B} + S_k, \tag{3.9}$$

$$\frac{D\varepsilon}{Dt} = \frac{\partial}{\partial x_j}\left(\frac{\nu_T}{\sigma_\varepsilon}\frac{\partial \varepsilon}{\partial x_j}\right) + \left(C_{\varepsilon,1}\mathcal{P} - C_{\varepsilon,2}\varepsilon + C_{\varepsilon,3}\mathcal{B}\right)\frac{\varepsilon}{k} + S_\varepsilon \tag{3.10}$$

with $\mathcal{P}$, $\mathcal{B}$ reflecting turbulence production due to shear and buoyancy respectively, while S_k, S_ε being additional source terms. Also, σ_k, σ_ε , $C_{\varepsilon,2}$, $C_{\varepsilon,3}$ are model constants. Eventually, it has to be noted that the temporal derivatives in (3.9) and (3.10) are neglected, consistently to the assumption of steady-state flow mentioned previously.

3.3 ABL-N inflow model

The ABL-N models discussed previously can be obtained by numerically solving (3.6) in the streamwise (x) and spanwise (y) direction. Assuming horizontal homogeneity, terms involving velocity gradients in the x and y directions can be neglected ($\partial\overline{u_i}/\partial x = \partial\overline{u_i}/\partial y = 0$). Likewise, the assumption that viscosity has negligible impact on the flow still holds for ABL flows, due to high Reynolds numbers computed based on a characteristic length scale e.g. the ASL height. Hence, the associated term can be once again disregarded, as in (3.6). Eventually the pressure gradient term is expressed through the geostrophic balance,

$$u_G f_C = -\frac{1}{\rho}\frac{\partial p}{\partial y} \qquad v_G f_C = \frac{1}{\rho}\frac{\partial p}{\partial x}$$

Therefore, (3.6) may simplify to,

$$x\text{-dir:}\quad f_c(\overline{v} - \overline{v_G}) + \frac{d}{dz}\left(\nu_T\frac{d\overline{u}}{dz}\right) = 0, \qquad y\text{-dir:}\quad -f_c(\overline{u} - \overline{u_G}) + \frac{d}{dz}\left(\nu_T\frac{d\overline{v}}{dz}\right) = 0 \tag{3.11}$$

wherein $\overline{u_G}$ and $\overline{v_G}$ are the geostrophic wind velocity components in the streamwise and spanwise directions respectively ($G = \sqrt{\overline{u_G}^2 + \overline{v_G}^2}$). The first term in (3.11) represents the effect of Coriolis-induced wind veer, while the second term indicates the contribution of turbulence to the momentum balance. Note that f_c is the Coriolis parameter and $u_{i,G}$ is the geostrophic wind velocity component in the i direction (i corresponding to the x and y directions).

Similarly to ABL-θ [56], the novel ABL-N model accounts for thermal effects through a non-zero buoyancy term $\mathcal{B}$ inserted to (3.9) and (3.10) in order to set the ABL height. The differentiation the two models lies in the formulation of that term; in particular, the latter includes the Brunt-Väisälä frequency defined as,

$$N = \sqrt{\frac{g}{\theta_0}\frac{d\theta}{dz}} \tag{3.12}$$

Hence, the buoyancy term is expressed as,

$$\mathcal{B} = \frac{g}{\theta_0}\overline{w'\theta'} = -\frac{g}{\theta_0}\frac{\nu_T}{\sigma_\theta}\frac{d\theta}{dz} = -\frac{\nu_T}{\sigma_\theta}N^2 \tag{3.13}$$

wherein θ_0, g reflect the potential temperature at ground level and the gravitational acceleration, while the vertical heat flux is expressed in terms of potential temperature gradient in the vertical direction i.e. $\overline{w'\theta'} = \frac{\nu_T}{\sigma_\theta}\frac{d\theta}{dz}$.

In the current model formulation, a constant Brunt-Väisälä frequency is assumed over the ABL height, stemming from a constant potential temperature profile in the vertical direction, which also implies that the heat flux should be constant in that direction. Clearly, this is a major assumption which is not realistic, yet the results obtained featured good agreement to LES simulated data. Eventually, a linear vertical profile of potential temperature is implied, and may be determined by integrating (3.12) as,

$$\theta = \theta_0 + \frac{\theta_0}{g}N^2 z \tag{3.14}$$

3.3.1 Similarity

From dimensional analysis, the non-dimensional solution obtained by this atmospheric inflow model has been found to solely rely on two non-dimensional numbers, namely the Zilitinkevich number and the surface Rossby number, which respectively read,

$$N_f = \frac{N}{f_C} \qquad Ro_0 = \frac{G}{f_C z_0} \tag{3.15}$$

The calculation of an ABL profile with a desired wind speed (U_∞) and TI (I_∞) at hub height comprises a two-step procedure; firstly a precursor library with various N_f and Ro_0 combinations is computed and followed by an interpolation in the non-dimensional space of N_f and Ro_0 in the pre-calculated library as per van der Laan et al. [61]. Eventually an optimisation procedure is carried out, in order to refine the interpolated profile and determine the optimal ABL for the required U_∞ and I_∞.

Besides, the ABL-N model satisfies the Reynolds number similarity as indicated in van der Laan et al. [59]. This is beneficial, particularly in AEP calculations were multiple wind speeds and directions need to be computed, as it may reduce the total number of required simulations.

3.3.2 Effect of surface roughness

The roughness length z_0 plays an important role in determining the ABL height in the ABL-N inflow model through the procedure discussed in the previous paragraph. The effect of that parameter on the ABL height is demonstrated in Figure 3.1, for the same U_∞, I_∞, f_C. Increasing shear through z_0 yields relatively shallower ABLs with relatively stronger super-geostrophic jet at the top, whereas lower z_0 values attenuate vertical temperature gradients enhancing the Ekman layer region.

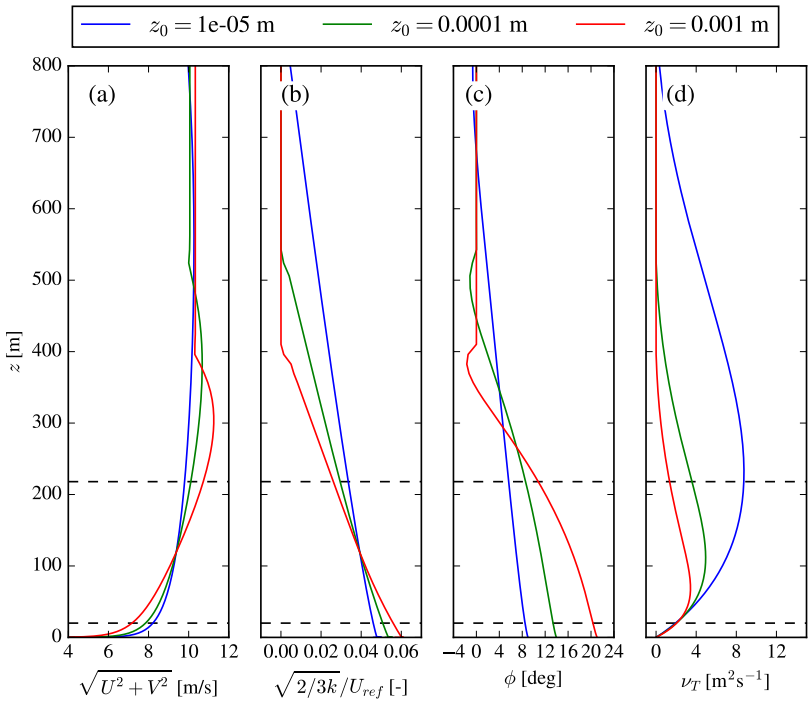

Figure 3.1: Comparison of ABL inflow profiles generated with the RANS-based ABL-N model for roughness length (z_0) variations. Results produced with $f_C = 1.14 \times 10^{-4}$ s^{-1}, $U_\infty = 9.2$ m/s, $I_\infty = 4\%$.

3.3.3 Effect of damping layer

The study by van der Laan et al. [57] that introduced the present model highlighted the presence of numerical instabilities in the solution at the far wake, due to the interaction of the highly turbulent wakes with the free atmosphere were turbulence is suppressed. In wind farm simulations, amplification of these instabilities is expected, owing to wake interactions. To mitigate potential convergence issues a damping layer of high eddy viscosity is implemented, extending above and in the far wake of the wind farm region. The artificial mixing resulting from the high eddy viscosity may therefore extinguish the numerical wiggles.

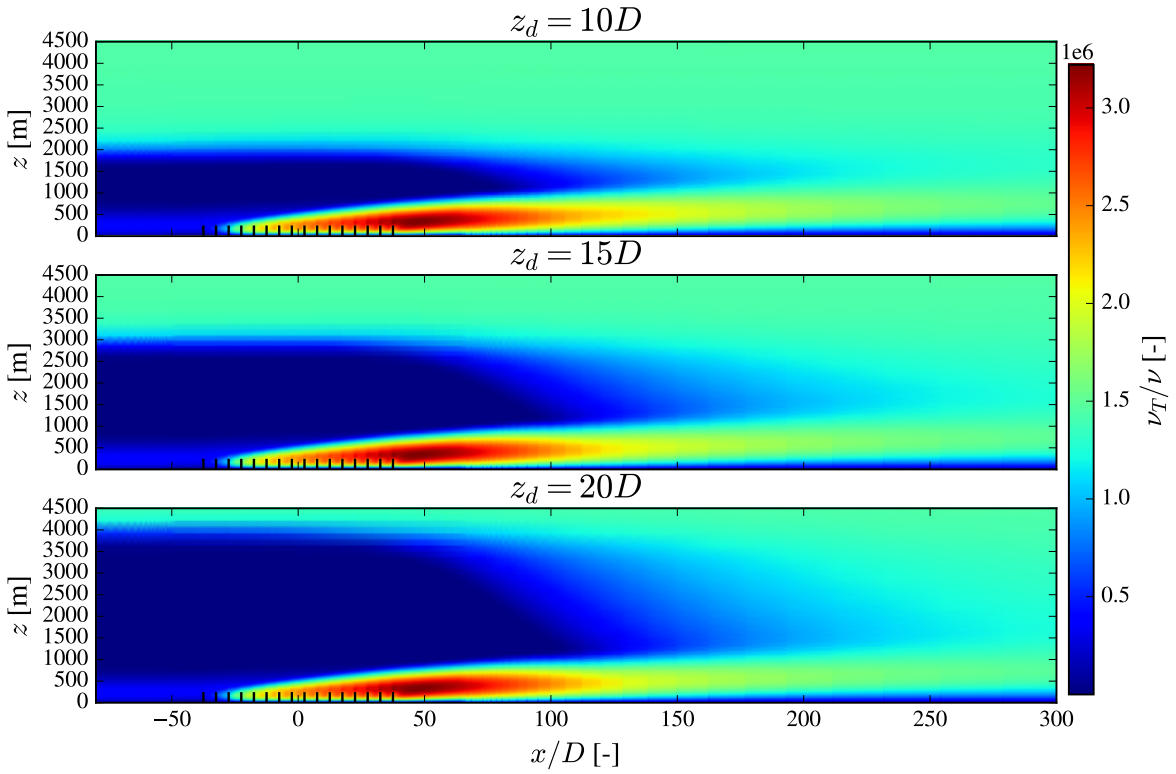

Figure 3.2: Lateral view of a qualitative comparison of the normalised eddy viscosity field ν_T for various damping layer heights z_d in a row of wind turbines. The streamwise distance of the damping layer start is kept constant in all cases as $x_d = 50D$ from the last turbine.

An demonstrative comparison of different damping layer heights z_d parametrised according to the rotor diameter and with constant streamwise damping layer distance x_d is depicted in Figure 3.2 employed in a wind farm simulation. The high eddy viscosity region in different altitudes and downstream of the wind farm may be clearly distinguished. Since this is a novel feature, there are not existing studies assessing the effect of the damping layer on the flow field. Hence, in later steps of the project the main driver for the choice of the damping layer height and streamwise distance will be based on two objectives; on the one hand numerical stability i.e. convergence of the numerical simulation should be ensured and on the other hand the damping layer region should be minimised in order to eliminate its impact on the flow.

3.4 Actuator Disk Method

Rotor forcing can be represented by various approaches in a CFD domain; the most common, given in descending computational requirements and accuracy are: the full resolution of the blade geometry, the actuator line (AL) and actuator disk (AD) method.

The latter is employed for the purposes of the present study for two reasons; firstly, despite optimal accuracy in wake predictions, blade resolving methods require unfeasible computational resources. Secondly, it has been found that the AL and AD methods are roughly equally accurate in wake modelling, with the former being more computationally demanding [51]. Hence, the AD approach is preferred over the other existing ones.

The aerodynamic forces acting against the flow, due to the presence of wind turbine rotors are represented by a momentum source (f_i) in (3.6). In the AD model implemented in PWE, a separate 2D polar AD grid with uniform radial and azimuthal cell distribution is generated, so as to construct the force vectors as suggested by [40]. Then, the forces are mapped on to the main computational grid with appropriate force redistribution described in [50].

In PWE a wide variety of methods to prescribe rotor forcing is available, including different force distributions, azimuthal forcing and inflow effects, namely shear and veer. A demonstration of the effect of various force methods (FM) provided in Table 3.1 on the evolution of the IEA10MW RWT wake is shown in Figure 3.3.

Firstly, a comparison between a uniform thrust distribution (FM1) and the one provided analytically by the Joukowsky rotor formulation [43] (FM2), neglecting azimuthal forcing and inflow effects, exhibits significant discrepancies on the overall structure of the wake as well as its convection downstream. The former (FM1) is not considered a realistic representation of the axial loading, thereby predicting a relatively lower deficit in the near wake. Also the larger deficit of FM1 in the inboard section of the blade (close to the root) results to slower wake recovery compared to the rest force methods. Overall, the force distribution consistent to the Joukowsky rotor may be employed for a more pragmatic characterisation of the AD forces.

Secondly, the effect of azimuthal forcing, i.e. wake rotation, may be considered (FM2, FM3), assuming no shear or veer in the estimation of the wake. The activation of azimuthal forcing clearly leads to a less pronounced wake deficit, particularly in the near wake, since the aerodynamic forces should be shifted more towards the rotor plane; i.e. the axial loading reduces with the inclusion of the azimuthal induction. Yet, that effect becomes less visible in successive downstream locations, where FM2 and FM3 tend to coincide.

Finally, further addition of inflow effects on the wake deficit may be regarded, accounting also for azimuthal forces (FM3, FM4). The compound effect of wake rotation and the inflow, predominantly shear, and less importantly veer, yield a non-axisymmetric wake deficit as per FM4; blade rotation causes momentum diffusion in the azimuthal direction, hence the high-momentum unperturbed flow above the turbine is entrained more towards one side (right end) of the wake leading to a faster recovery in that region. Conversely, the low-momentum flow under the rotor is pushed towards the other end (left), yet it does not compensate the momentum increase, leading to a non-uniform wake deficit

profile. At the near wake, where the deficit is highly impacted by the blade geometry, this effect may be seen in terms of the uneven peaks, while at the far wake the peak is displaced towards the left.

Table 3.1: AD methods and associated features available in PWE.

AD method	Force distribution	Azimuthal Forcing	Inflow effects
FM1	Uniform	Off	Off
FM2	Joukowsky rotor	Off	Off
FM3	Joukowsky rotor	On	Off
FM4	Joukowsky rotor	On	On

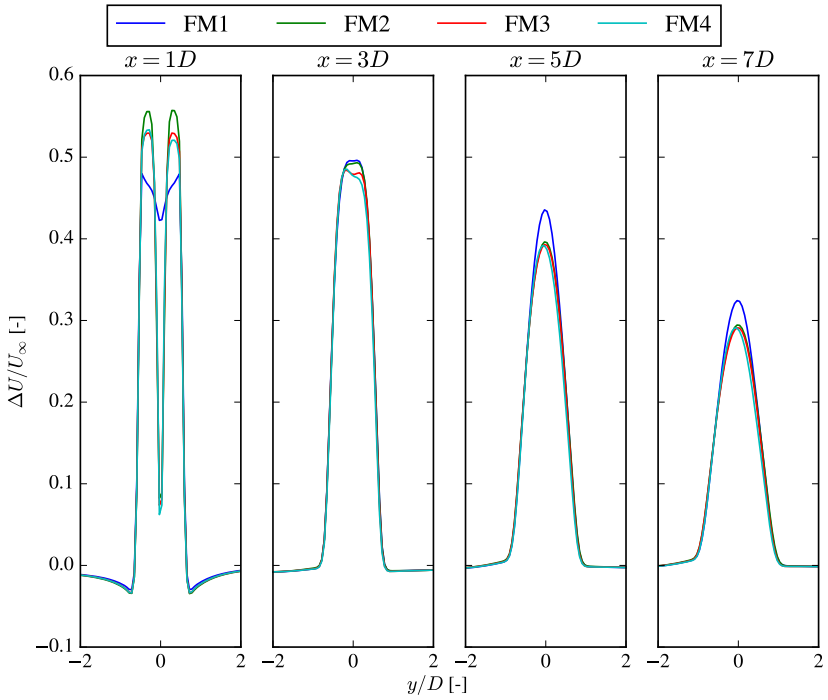

Figure 3.3: Downstream evolution of the normalised velocity deficit at a single IEA10MW RWT wake using various AD forcing methods. Isolating inflow (wind shear and veer) and azimuthal forcing effects. Results produced with $U_\infty = 9.2\text{m/s}$, $I_\infty = 4\%$, $f_c = 10^{-4}\text{s}^{-1}$.

3.5 Multiple AD force treatment

In numerical simulations involving wind turbine wake interactions, the incoming flow speed should be known apriori, in order to set the rotor forcing. In stand-alone wind turbine scenarios, the wind speed at hub height can be used to represent the thrust forces at the rotor disk. Yet, when multiple wind turbines are to be analysed, determining the inflow speed for each one of them is not straightforward, owing to the presence of considerable blockage effects upstream and the waked flow downstream.

A comparison of three different techniques to account for that effect has been presented in van der Laan et al. [62]; the first technique makes use of tabulated airfoil data, the second involves 1D momentum theory, whereas the third performs force calibration. Due to the restricted access to polar data, the first method was disregarded from the present analysis.

The assessment carried out in the following chapters focuses on the latter two methods. Their common characteristic is that instead of computing the aerodynamic forces based on the free stream speed, they express turbine performance in terms of AD-averaged quantities. In particular, the following conditions should be imposed

$$C_T^* = C_T \left(\frac{U_{AD}}{U_\infty}\right)^2 \qquad C_P^* = C_P \left(\frac{U_{AD}}{U_\infty}\right)^3 \tag{3.16}$$

wherein, C_T^*, C_P^* represent the AD-averaged aerodynamic performance coefficients, U_{AD} is the axial velocity averaged over the AD area and U_∞ is the wind speed of the undisturbed flow at hub height. In the preceding formulation the velocity ratio U_{AD}/U_∞ should be determined, in order to obtain the thrust and power at the AD.

3.5.1 Method 1: 1D Momentum theory

A relation between the U_{AD} and U_∞ should be derived, in order to close (3.16). That relation may be obtained from 1D momentum theory, according to which the following expression holds,

$$U_\infty = \frac{U_{AD}}{1 - a_x} \qquad a_x = 0.5\left(1 - \sqrt{1 - C_T}\right) \tag{3.17}$$

wherein a_x represents the axial induction.

Two important remarks related to this strategy have to be mentioned. Firstly, in order to address heavily loaded rotor cases i.e. $a_x > 0.3 - 0.4$ empirical relations have been proposed e.g. by Prospathopoulos et al. [37], yet in the present study the axial induction does not surpass that threshold, thus the corrections were not utilised. Secondly, that simple approach overpredicts the thrust forces and power for wind speeds below rated, owing to overestimation of the inflow velocity at hub height, indicating underprediction of the associated wake deficits. This method suffices when power ratios between streamlined turbines are computed, since both turbines' power is overpredicted by similar factors. Nevertheless, it is not favourable when absolute power is of interest.

3.5.2 Method 2: Force Calibration

In the procedure introduced in van der Laan et al.[58], the scaling of (3.16) is addressed by means of force calibration. This entails numerical simulations of a stand-alone

wind turbine performed prior to the actual calculation at hand, since rotor forcing can be conveniently prescribed i.e., without the need for such scaling. The single-turbine simulations are carried out over the entire wind speed range (from cut-in to cut-out) in 1m/s intervals and the U_{AD} can be extracted, to eventually create C_T-U_{AD}, C_P-U_{AD} relations for each U_∞. Subsequently, these relations are accessed to simplify the definition of AD forces in multiple turbine simulations.

The comparative assessment of van der Laan et al.[58] suggests that force calibration method is most accurate in power and thrust force predictions in double wake scenarios compared to method 1. Therefore, when absolute power numbers are of interest, this approach should be preferred.

3.6 Grid generation & boundary conditions

In the present section, an argumentation for the numerical setup used in the present study, including the domain size, boundary conditions and numerical grid parameters is hereby presented.

A schematic of the domain employed in the present work is demonstrated in Figure 3.5. Firstly, an ABL profile is calculated through a precursor simulation in EllipSys1D [55] implementing a 1D grid, consistently to the method mentioned in section 3.3. To that end, a tall domain of 100 km is selected for the precursor simulations, accounting for the effect of large ABL heights. Subsequently, the 3D domain suited for wind farm simulations is initialised with the 3D equivalent of the resulting ABL profile.

A Cartesian grid with uniform roughness and elevation, corresponding to flat terrain was employed for all simulated cases, comprising a general flow domain as well as a wake refinement region for convenient resolution of the occurring steep gradients. The grid structure is demonstrated in Figure 3.6, while a description of the controlled sizing parameters in PWE is given in Table 3.3.

The grid size may be chosen based on the trade-off between low computational cost and high accuracy (i.e. low grid errors). An important feature that influences the aforementioned aspects is the wake refinement region spacing (grid_cells1_D). It has been found that for an adequate resolution of the wake it should be at minimum $D/8$ [58]. The sensitivity of the numerical solution with respect to that parameter was assessed in the present work through a grid study on a stand-alone turbine, consistently to Roy [42], in order to quantify the associated errors and eventually obtain a grid independent solution. Figure 3.4 depicts a comparison of the disk-averaged streamwise velocity for increasing wake region spacing. Further analysis with $D/32$ and $D/4$ is not feasible due to prohibitively high computational requirements and high grid errors respectively. A preliminary investigation showed that for single wake simulations the computational cost allows the use of 16 cells per diameter, whereas in wind farm simulations a compromise

of either 8 or 10 cells per diameter was found optimal (see relevant chapters 4, 5). The discretisation of the AD polar domain for the computation of the AD forces (discussed in section 3.4) was also considered. Initial analyses proved that employing a grid of 64x64 cells (in radial and azimuthal direction) can yield optimal results.

The boundary conditions used in PWE are outlined in Table 3.2. The ground effect is accounted for by a Neumann boundary condition (BC) described in [45] representing a rough wall of roughness length z_0. The same consideration was also made for the 3D domain; periodicity to the lateral boundaries was imposed, in order to account for the effect of wind veer included in the ABL-N model, while the outlet of the domain is described by a zero gradient BC, assuming fully developed flow.

Table 3.2: Summary of boundary conditions used in the numerical simulations. The subscript *in* (inflow) refers to the corresponding quantity from the precursor solution. Table adjusted from the PWE documentation [16].

Boundary	BC type	u	v	w	k	ε
bottom	rough wall	0.0	0.0	0.0	Neumann [45]	ε_{in}
inflow	inlet	u_{in}	v_{in}	0.0	k_{in}	ε_{in}
top	inlet	u_{in}	v_{in}	0.0	k_{in}	ε_{in}
outflow	zero gradient					
lateral	periodic					

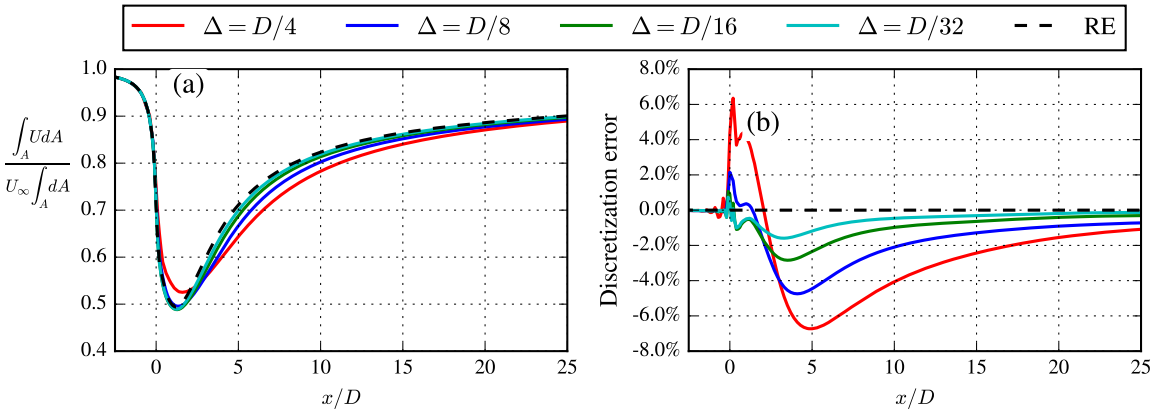

Figure 3.4: Grid convergence study, consistently to Roy [42]. (a) Normalised disk-averaged streamwise velocity in the streamwise direction for various wake sizes. (b) associated discretisation errors. Note that RE corresponds to Richardson extrapolation.

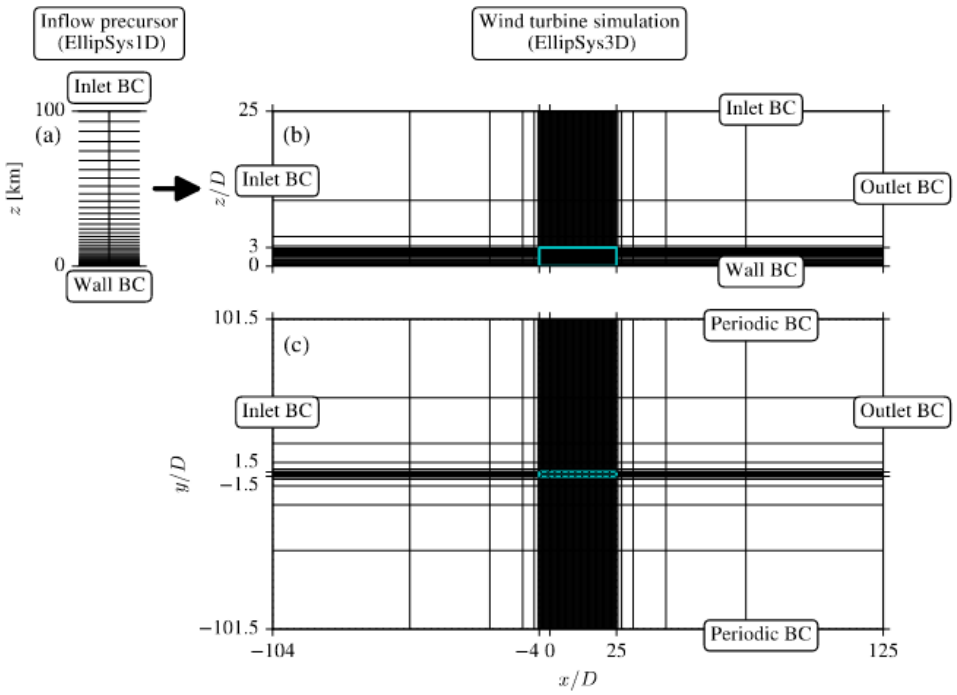

Figure 3.5: Schematic of (a) 1D ABL inflow precursor simulation domain, (b) lateral view and (c) top view of the 3D wind farm flow simulation domain. The wind farm domain is initialised with the atmospheric profile calculated as per (a); Courtesy of van der Laan et al. [57]

Table 3.3: Description of grid sizing parameters in correspondence with Figure 3.6.

Parameter	Description
Outer domain	
grid_Dref	reference rotor diameter for grid scaling
grid_radius_D	horizontal flow domain extent
grid_zlen_D	flow domain height
grid_zFirstCell_D	first cell height
Wake refinement region	
grid_cells1_D	cells per diameter in refinement region
grid_m1_w_D	horizontal western wake domain margin
grid_m1_e_D	horizontal eastern wake domain margin
grid_m1_n_D	horizontal northern wake domain margin
grid_m1_s_D	horizontal southern wake domain margin
grid_zWakeEnd_D	vertical wake domain dimension
AD polar grid	
adgrid_nr	number of radial points
adgrid_ntheta	number of azimuthal points

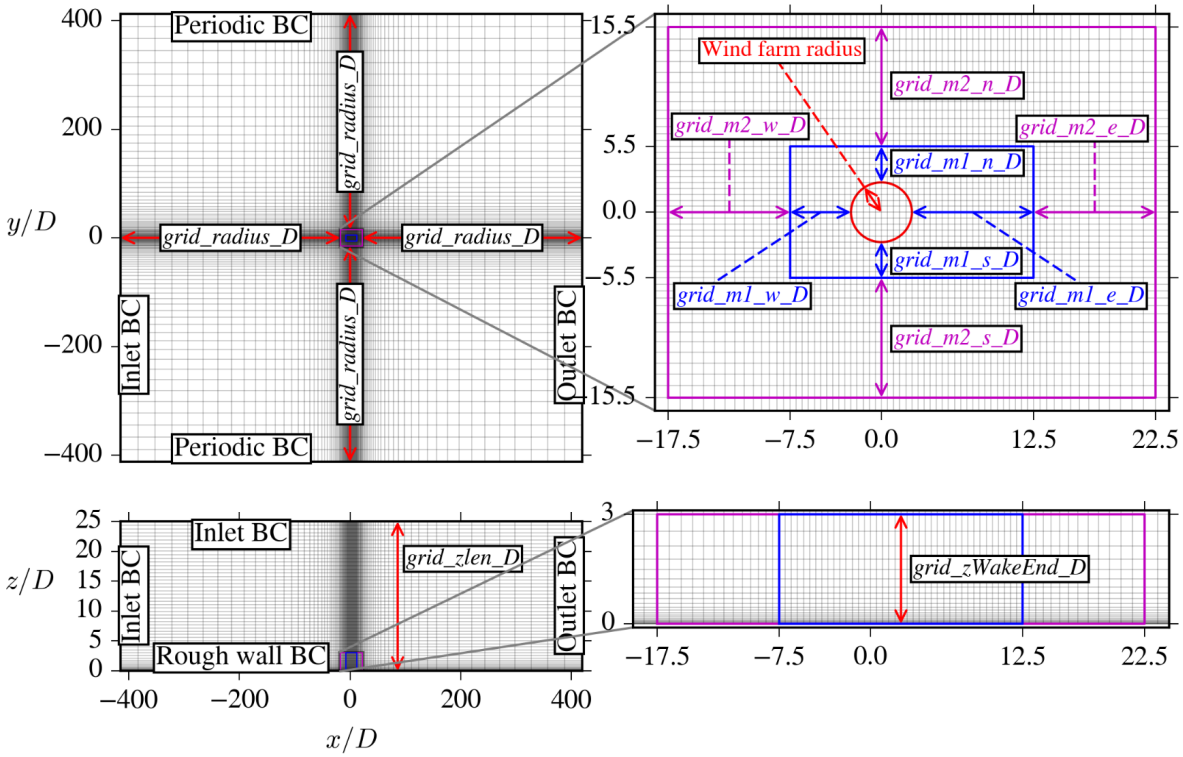

Figure 3.6: Schematic of the cartesian grid generated in PWE with all controlled parameters. The depicted parameters are for reference. The actual values chosen for all parameters are given in chapter 4 and 5.

CHAPTER 4
Inflow Model Validation

In the present chapter **RQ1** is dealt with. As mentioned in chapter 1, the RANS-based ABL-N inflow model presented in section 3.3 has not been yet tested in wind farm scale, therefore the present chapter demonstrates the model validation process; that is, to assess its capabilities on modelling wake effects in wind farm flows. Firstly, the numerical setup and the argumentation for the choices regarding the grid, force method, layout, and flow cases are demonstrated. Secondly, the results of the assessment are illustrated and interpreted.

4.1 Setup

Validation of the model in the current study was made possible by considering the work of Lanzilao et al. [25] and the corresponding LES database [26] for Conventionally Neutral Atmospheric Boundary Layer (CNBL), publicly available in the KU Leuven repository. That study focuses on a fictious offshore wind farm demonstrated in Figure 4.1 with the corresponding coordinate system defined. It consists of a 16×10 grid of IEA 10 MW Reference Wind Turbines (RWT) [9], whose operational data is depicted in Figure 4.2. Further turbine specifications are provided in Table A.1 in Appendix A. The IEA 10 MW turbine has a rotor diameter of $D = 198$m at a hub height of $z_h = 119$m.

To ensure a meaningful comparison between the LES and RANS-based results, the simulation setup from the reference database was closely replicated wherever feasible. To that end, the wind farm layout and turbine type were kept the same. Likewise, the primary aim of the investigation is to study the effect of the inflow model on the prediction of the wake. However, the overall wake structure and downstream convection are also highly dependent on the rotor forcing. Hence, the effect of the prescribed forces should be eliminated in order to obtain an estimate solely on the efficiency of the inflow model in wake predictions. To that end, similar force method to Lanzilao & Meyers [25] was implemented, namely AD with uniform axial loading in absence of azimuthal forces i.e. non-rotating actuator disk. Nevertheless, it has to be noted that this is a rather simplified representation of a realistic force distribution along a wind turbine blade, which however, suffices for an accurate prediction of the wake, except for the near wake i.e. $x/D < 5$, where the velocity is overpredicted [69]. Similarly, the force control method, consistent to 1D momentum, reviewed in section 3.4 was employed to model wind turbine interactions in wind farms for the same reasons. Despite the well-known underprediction of the rotor forces of such a method coupled with a RANS approach as per van der Laan

et al. [62], the selection of a different force control strategy than that adopted in the abovementioned LES study, would amplify the associated effect on the flow field, thereby preventing a realisable comparison.

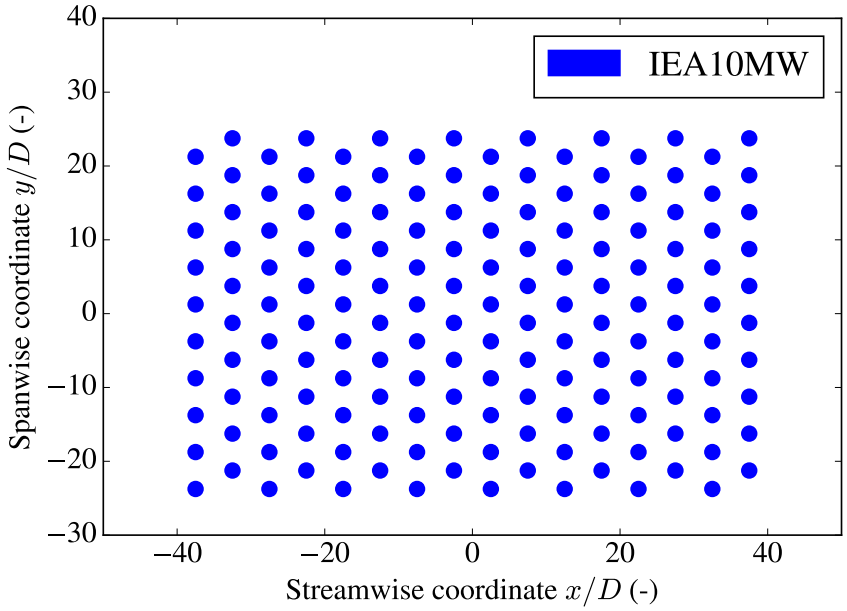

Figure 4.1: Top view of the wind farm layout and coordinate system considered for the validation of the RANS-based ABL-N inflow model. Layout taken from Lanzilao & Meyers [25].

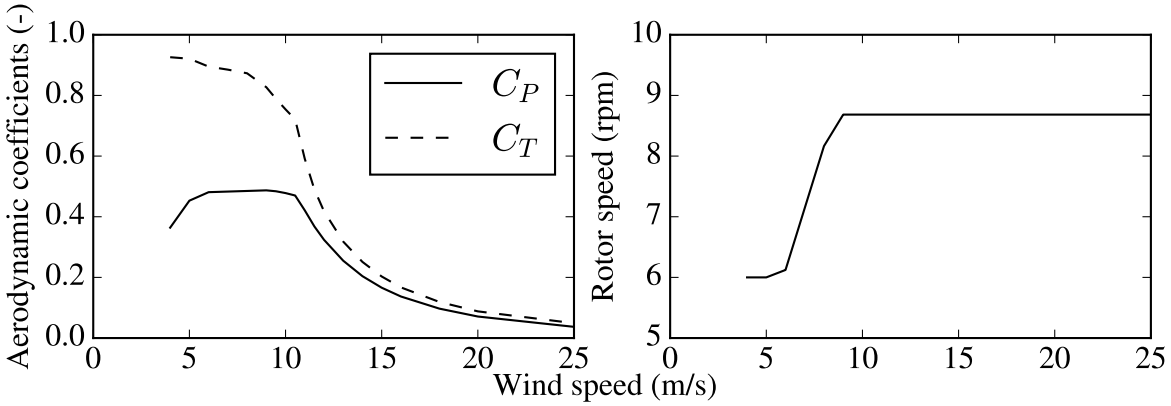

Figure 4.2: Operational data of the IEA10MW RWT [9], left: aerodynamic coefficients, right: rotor speed curve.

The grid sizing parameters chosen for the investigation are summarised in Table 4.1.

The overall domain size was chosen adequately large, namely 500 rotor diameters in the streamwise and spanwise directions, such that the presence of artificial blockage effects on the numerical solution is minimised. The height of the domain is set to 25 diameters, with the first cell height being 0.5% of the rotor diameter and exponentially growing in the vertical direction. The wake refinement region extends 3 diameters vertically, 10 diameters upstream, 40 diameters downstream and 2 diameters laterally with respect to the radius defined by the wind farm at hand (see Figure 3.6). The objective that led to the aforementioned choices was to capture upstream effects, the wind farm wake downstream as well as potential lateral convection or deflection of the wake. The wake domain was discredited with 16 cells/D and 10 cells/D for stand-alone turbine and wind farm flow simulations respectively, consistently to the trade-offs mentioned in chapter 3. In addition, the residual threshold was fixed to 10^{-5} for all simulations.

Table 4.1: Grid sizing parameter values for RQ1 in correspondence with Figure 3.6. The values are normalised by the rotor diameter of the IEA10MW RWT [9].

Parameter	Normalised Value
Outer domain	
grid_Dref	$D = 198$ m
grid_radius_D	500
grid_zlen_D	25
grid_zFirstCell_D	0.005
Wake refinement region	
grid_cells1_D	single turbine:16, wind farm:10
grid_m1_w_D	10
grid_m1_e_D	40
grid_m1_n_D	2
grid_m1_s_D	2
grid_zWakeEnd_D	3
AD polar grid	
adgrid_nr	64
adgrid_ntheta	64

Table 4.2: Examined flow cases and associated features from Lanzilao & Meyers [26] under CNBL conditions. H is the ABL height, $\Delta\theta$ represents the capping-inversion strength and Γ is the free atmosphere lapse rate. U_∞ and I_∞ reflect the unperturbed flow wind speed and TI respectively, while the parameters z_0, f_C, G indicate the roughness length, Coriolis parameter and geostrophic wind respectively.

Case	H, $\Delta\theta$, Γ	U_∞, I_∞	z_0, f_C, G
$H1000$	1001 m, 5.33 K, 4 K km^{-1}	9.24 m/s, 3.93 %	10^{-4} m, $1.14 \cdot 10^{-4}$, 10 m/s
$H500$	509 m, 5.28 K, 4 K km^{-1}	9.13 m/s, 4.18 %	10^{-4} m, $1.14 \cdot 10^{-4}$, 10 m/s

Furthermore, for the purposes of the present thesis, two flow cases were adopted from the previously mentioned LES dataset, whose features are outlined in Table 4.2. These flow scenarios were chosen such that the evaluation of the ABL-N model efficiency in different ABL heights is permitted. In particular, the only variable in the LES data against which the RANS results were compared, is the ABL height H, whereas the lapse rate Γ, capping-inversion strength $\Delta\theta$, Coriolis parameter f_C, roughness length z_0, geostrophic wind G and atmospheric conditions (CNBL) remain unchanged.

4.2 Results and Discussion

The validation procedure comprises qualitative and quantitative comparisons carried out in three intermediate steps; the first step focuses on generating atmospheric inflow profiles with the ABL-N model in accordance with Table 4.2 and comparing them to the LES and ASL, whereas in the second step, the ABL inflows are contrasted in a single wind turbine wake setup, similar to van der Laan et al.[57]. Ultimately, once the above two tests have been completed, the implementation of the ABL inflows generated in the first step is extended to wind farm wake simulations utilising the configuration shown in Figure 4.1.

4.2.1 Atmospheric inflow comparison

The present section provides a comparison between ABL inflow profiles in the vertical direction computed by the RANS-based ABL-N and ASL models against the equivalent profiles contained in the reference LES dataset. The latter correspond to time-averaged fields over a time span of 4 hr and spatially averaged over the domain width, to suppress possible local variations.

Likewise, ABL-N-produced profiles were tuned through appropriate adjustments of the roughness length z_0 as discussed in the previous chapter, such that they match the LES ones to the greatest feasible extent. In particular, the main objective was to mimic the LES profiles in wind speed and TI at hub height. Besides, an additional objective concerns achieving similar wind shear and capping-inversion height by the roughness length tuning; that is, the trade-off between shear and ABL height was considered as described previously and clearly depicted in Figure 3.1. Roughness lengths of $z_{0,H500} = 10^{-5}$ m and $z_{0,H1000} = 5 \times 10^{-5}$ m were used for the cases H500 and H1000 respectively. On the contrary, the roughness length for the ASL profile was set consistently to the method described in van der Laan et al. [63]. Alternatively, the RANS-based profiles could be generated by calibration of the model constant C_μ using the available LES data, yet this would require recalibration of the f_P parameter (see (3.8)), as it is a function of C_μ.

Figure 4.3 illustrates the atmospheric inflow profile comparison in the vertical direction in terms of five measures, namely velocity magnitude, TI, veer angle, potential temperature, and eddy viscosity. The latter is to showcase the differentiation of the ABL-N inflow

model from the ASL one and its ability to produce a physically reasonable eddy viscosity despite its simplicity.

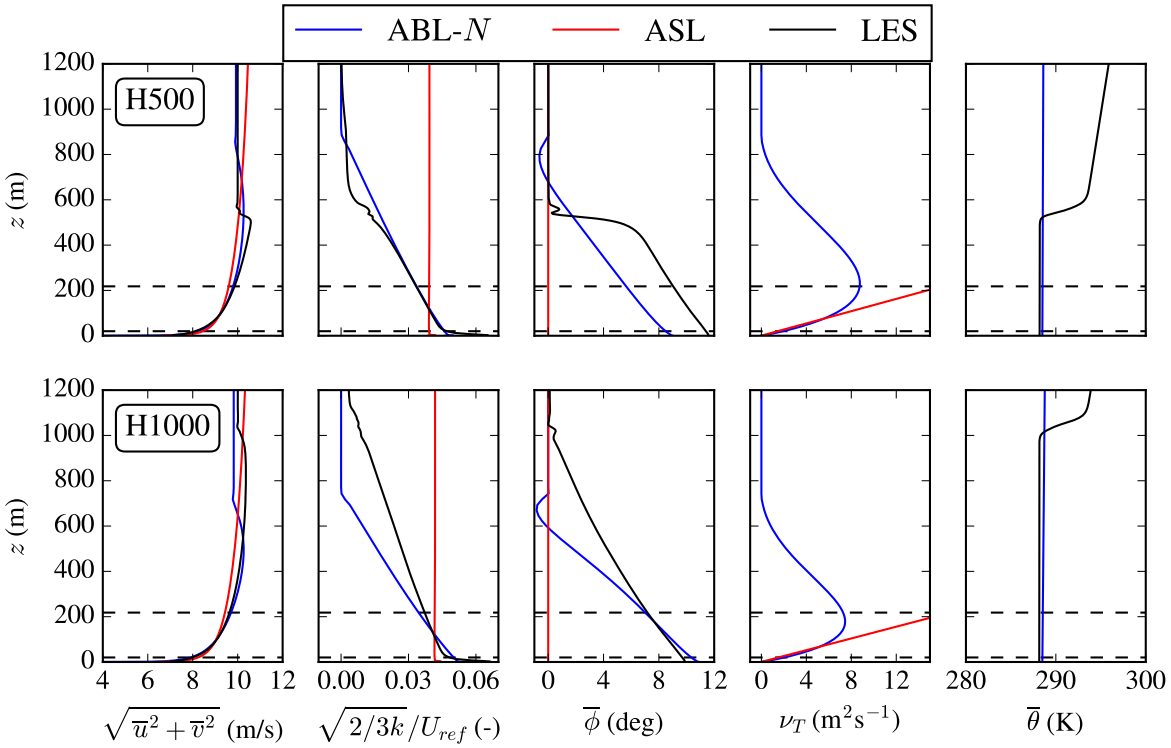

Figure 4.3: ABL profile comparison between RANS-based ABL-N and ASL models against mean LES profiles for CNBL [25]. The LES profiles are time-averaged over a time span of 4 hrs and spatially averaged over the domain width to suppress transient effects. The rotor area of the IEA10MW RWT is denoted in horizontal dashed black lines. The ABL-N profiles were generated with roughness lengths of $z_{0,H500} = 10^{-5}$ m and $z_{0,H1000} = 5 \times 10^{-5}$ m for the cases H500 and H1000 respectively.

The ABL is limited by the capping-inversion for the ABL-N and LES results, whereas the figure for the ASL model shows an ever-growing wind speed profile implying infinite ABL height. It can be seen that the wind shear of the LES profiles is resembled with high accuracy by ABL-N through proper tuning of z_0, yet the ABL heights of the latter show considerable deviations to the former in both cases. In particular, deeper and shallower ABL is predicted by ABL-N in the H500 and H1000 cases respectively. Conversely, a significantly less accurate wind shear is obtained by the ASL model, as expected. It has been found that, in general, analytical models can yield optimal agreement in weakly stratified free atmosphere [34] conditions.

Another common feature between ABL-N and LES profiles is the presence of super-geostrophic jets at the top of the boundary layer, characteristic of CNBL conditions.

This phenomenon is more pronounced in the shallow ABL case (H500) where the velocity gradients are stronger. This was not resolved by ABL-N model as it predicts a relatively deeper ABL in that case, thereby attenuating the velocity gradients. On the contrary, the analytical ASL model does not account for such jet. Overall, ABL-N exhibits high level of agreement with LES, particularly around the hub height, within the rotor area and slightly further above with the capability of accounting for more physical mechanisms.

The figure for TI, shows non-zero values only below the capping-inversion, except for the ASL profile which has a non-physical constant value along the vertical direction. ABL-N was found to predict identical TI profile for the majority of the vertical positions in the H500 case, yet there are some deviations from the LES close to the capping-inversion due to the different ABL heights between the two models. The aforementioned deviations are more pronounced in the deep ABL case (H1000).

Considerable discrepancies were also recorded for the wind direction between ABL-N and LES. Note that a reference veer angle of 0 deg was regarded above the capping-inversion. The veer angle is predicted quite accurately in H1000, particularly within the rotor area, whereas remarkable deviations were witnessed in H500. Once again, a substantial source of discrepancies is the difference in the ABL height attained.

Ultimately, the thermal stratification of the LES results is reflected by the potential temperature. As discussed in section 3.3, the linear temperature profile in the vertical direction of the ABL-N model stems from the constant temperature gradient assumption and is unable to represent a temperature profile that characterises CNBL conditions. A more realistic potential temperature profile may be obtained by the method proposed in Rampanelli & Zardi [38] as in the ABL-Θ model formulation [56]. However, it is worth mentioning that, contrary to LES, in RANS-based models a temperature transport equation is not employed, since that would mean that the wind conditions perceived by the most upstream wind turbines would be different than the ones prescribed at the inlet of the domain, unless the potential temperature is linear [54]. Otherwise, the distance between the inlet and the first row of turbines would become a parameter, as the solution would develop downstream.

A quantitative comparison of the atmospheric inflows, focused on wind speed magnitude and TI, is illustrated in Figure 4.4, featuring the normalised difference defined as,

$$\Delta\psi = \frac{\psi_{RANS} - \psi_{LES}}{\psi_{\infty}} \times 100 \tag{4.1}$$

wherein $\psi = [U, I]$ and ψ_{∞} being the free-stream quantity of interest probed at hub height. A more accurate prediction of the wind speed and TI was witnessed in the shallow ABL case (H500) by the ABL-N model, with the normalised differences quantifying to less than 5% for both quantities within the ABL regime. Some significant deviation in the order of 20% were, nevertheless, recorded at the capping-inversion region for the

latter quantity. Similar but slightly higher differences in wind speed were also found for the deep ABL flow case (H1000); the maximum discrepancy was once again seen close to the capping-inversion due to the different ABL heights predicted by ABL-N. The figure for TI shows remarkably worse predictions compared to the shallow ABL case. In summary, there are clear improvements of the ABL-N results compared to the ASL ones, which is an anticipated deduction.

Ultimately, it is evident that there are minor discrepancies in geostrophic wind speed; however, these are found in the order of a few percent. Better prediction of the geostrophic wind was once again recorded in the shallow ABL flow case.

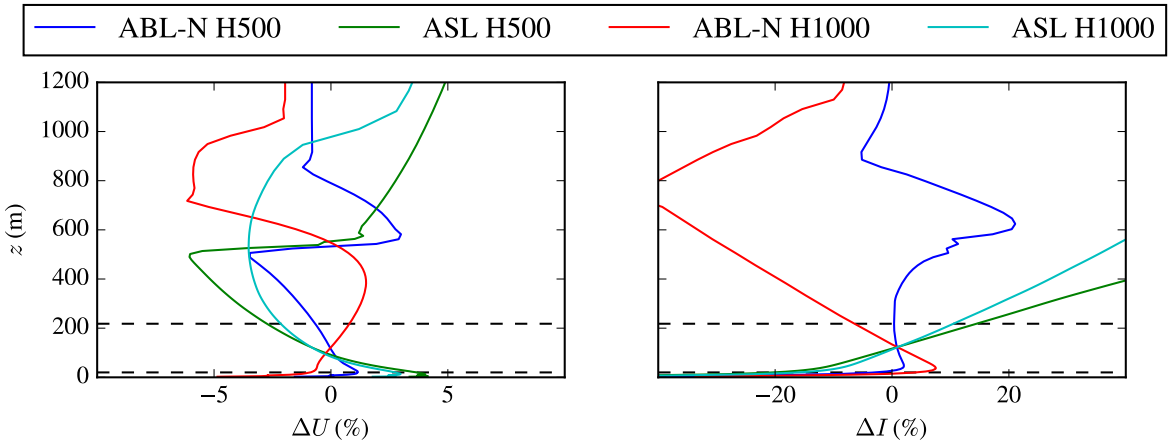

Figure 4.4: Comparison of the normalised difference between inflow profiles produced by RANS ABL-N, ASL models and LES simulated results (CNBL) [25]. The rotor area of the IEA10MW RWT is denoted in horizontal dashed black lines.

4.2.2 Single wake comparison

The second stage of the inflow model evaluation involves a comparison of the flow phenomena at the wake of a single IEA 10 MW wind turbine subjected to the atmospheric inflows discussed previously, as in van der Laan et al. [57] for benchmarking.

The objective of the current study is to isolate the effect of the turbulence (inflow) model and contrast it against higher fidelity results. Therefore, the AD force method FM1 (see Table 3.1) is preferred for further investigations over FM4 as discussed in section 3.4, in order to mimic the approach adopted in the LES simulations [25] and thereby eliminate the influence of the force method on the results. Hence, a more meaningful comparison may be realised. Yet, for the sake of completeness, both FM1 and FM4 approaches are hereby presented.

A qualitative comparison of the RANS models against the LES dataset is shown in Figure 4.5 and Figure 4.6, where the quantities of interest are the wake-induced velocity

deficit and added TI respectively along the vertical direction. The depicted illustration features the referred profiles at the rotor midplane in various downstream locations, defined as

$$u^- = \frac{\sqrt{\overline{u}^2 + \overline{v}^2}_{\text{inflow}} - \sqrt{\overline{u}^2 + \overline{v}^2}}{U_\infty} \qquad I^+ = \frac{\sqrt{2/3k} - \sqrt{2/3k}_{\text{inflow}}}{I_\infty} \tag{4.2}$$

wherein the subscript inflow denotes the associated quantities probed at a streamwise distance of $x = -3D$ upstream of the wind turbine. Note that the LES data correspond to time averaged quantities as described in the atmospheric inflow comparison.

Firstly, no significant variations in the occurring flow phenomena were recorded between the two flow cases, due to high similarity in inflow conditions (i.e. U_∞, I_∞ from Table 4.2). The velocity deficit is considerably underpredicted, with the deviations being maximum in the near wake. Yet, uniform axial force distribution (FM1) in LES has been proved adequate to reproduce the wake structure except for the near wake [69]. Therefore, the comparison in that region cannot be fully relied on. It is also evident that FM1 is indeed able to produce slower wake recovery than FM4, thereby resembling more accurately the LES wake convection. This is attributed to the existence of a significantly higher velocity region (i.e. lower deficit) close to the hub in the latter method, which triggers more pronounced momentum mixing and thus faster recovery.

Contrasting the RANS-based models, despite the marginal differences in the near wake, ABL-N demonstrates better capabilities than ASL in predicting the wake-induced velocity deficit for downstream distances $x \geq 5D$. Eventually, in the far wake, i.e. $x = 15D$ the deviations are again fractional.

Comparing these findings with those highlighted in the equivalent assessment of van der Laan et al. [57], it can be concluded that the present work finds larger deviations to LES for single wake simulation. In particular, the comparison provided by the aforementioned study employed FM4 and contrasted the results against the LES field of Hodgson et al. [22] which was generated with the same force method and software. Yet, this was not possible for the current study. Therefore, the deviations obtained may be associated with the differences in force method implementation, as the LES simulations of Lanzilao & Meyers [25] were carried out in different software.

Similar conclusions can be drawn for TI (Figure 4.6). In that case, a significant overprediction is observed as anticipated; FM1 shows minimal deviations, although the order of magnitude remains significant. Another interesting observation is that the ABL-N model predicts slightly better the added TI than the ASL model.

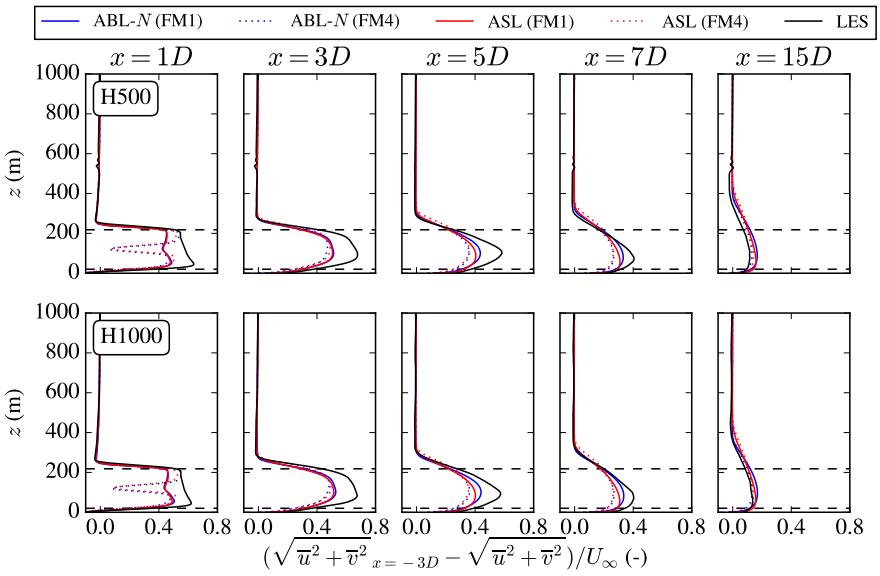

Figure 4.5: Normalised wake-induced velocity deficit comparison in the vertical direction between LES and RANS-based ABL-N and ASL models using different AD force methods (see Table 3.1). The depicted quantities correspond to a spanwise location at the rotor midplane. The rotor area of the IEA10MW RWT is denoted in horizontal dashed black lines.

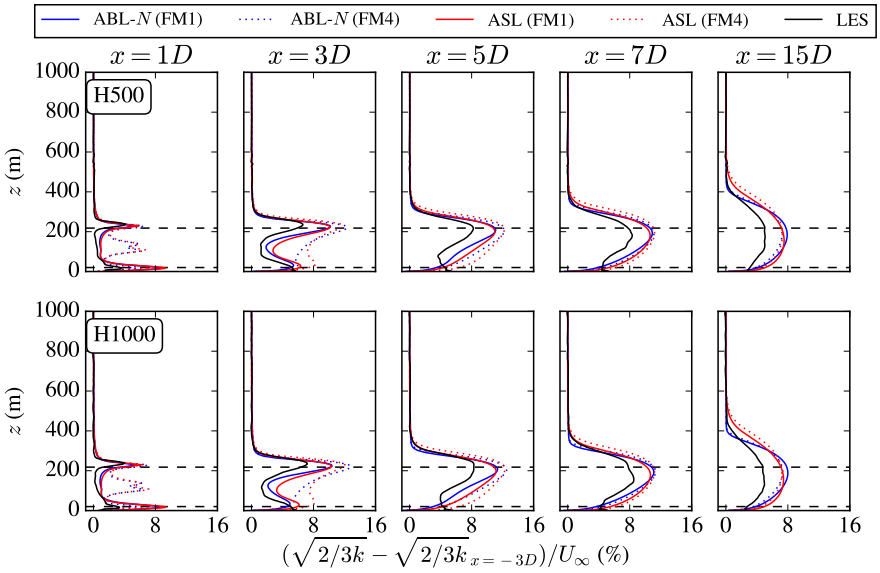

Figure 4.6: Normalised wake-added TI comparison in the vertical direction between LES and RANS-based ABL-N and ASL models using different AD force methods (see Table 3.1). The depicted quantities correspond to a spanwise location at the rotor midplane. The rotor area of the IEA10MW RWT is denoted in horizontal dashed black lines.

The corresponding quantitative comparison in terms of velocity and TI, dictated by (4.1) reflects the order of magnitude of the discrepancies, illustrated in Figure 4.7 and Figure 4.8. Regarding the former, FM1 deviates roughly 20% at maximum from the LES whereas FM4 exceeds 40% close to the turbine (i.e. $x = 1D$). Furthermore, ABL-N demonstrates improvements in wake deficit predictions compared to ASL, as expected, especially for $x \geq 5D$, where the comparison can be considered more meaningful for the reasons mentioned previously. On the contrary, the deviations of the latter quantity (TI) can exceed 50%, thereby highlighting the limitation of the linear eddy viscosity model (3.8) to accurately represent the TKE field and as an extent the TI.

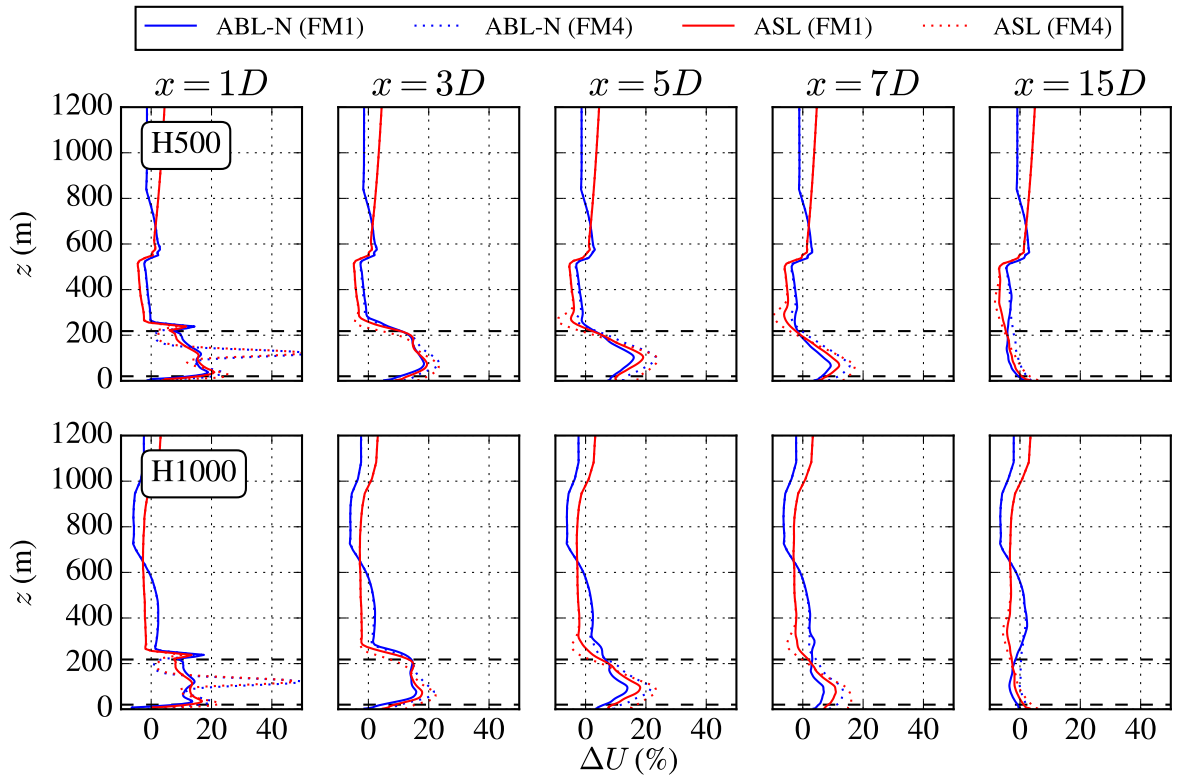

Figure 4.7: Normalised velocity difference comparison in the vertical direction between LES and RANS-based ABL-N and ASL models using different AD force methods (see Table 3.1). The depicted quantities correspond to a spanwise location at the rotor midplane. The rotor area of the IEA10MW RWT is denoted in horizontal dashed black lines.

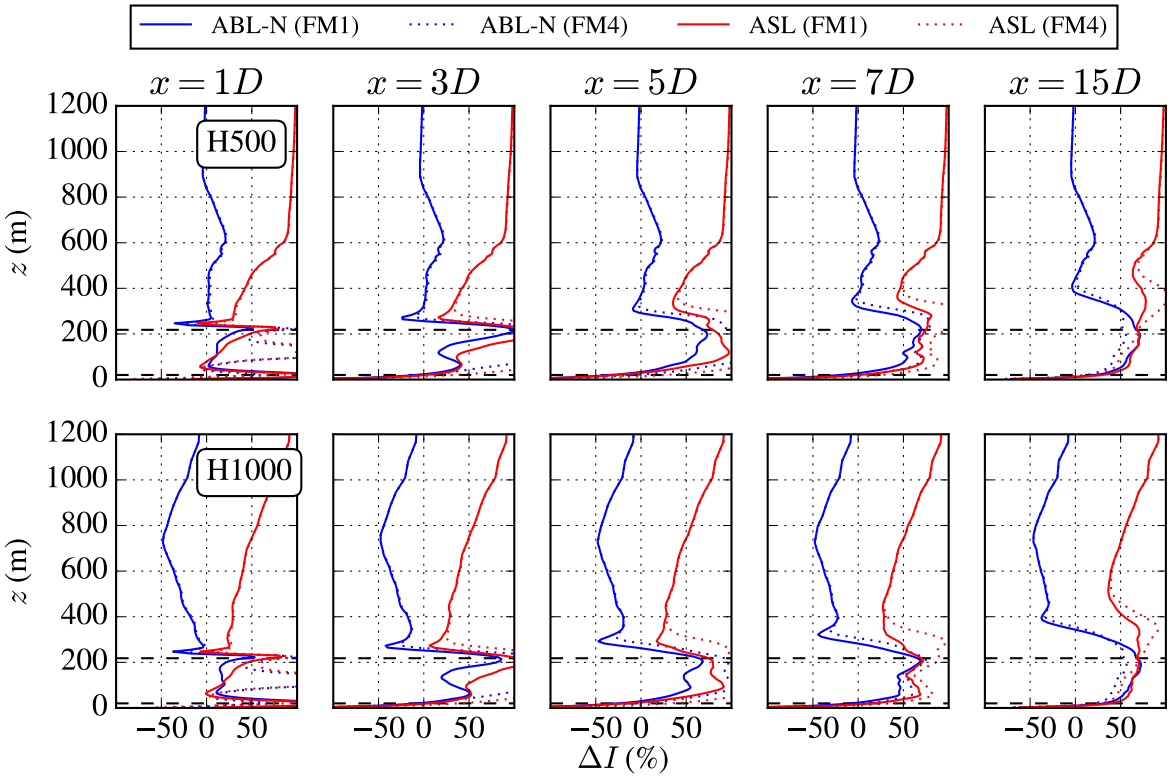

Figure 4.8: Normalised TI difference comparison in the vertical direction between LES and RANS-based ABL-N and ASL models using different AD force methods (see Table 3.1). The depicted quantities correspond to a spanwise location at the rotor midplane. The rotor area of the IEA10MW RWT is denoted in horizontal dashed black lines.

4.2.3 Comparison of wake effects in wind farms

The final stage of the model evaluation focuses on the application of ABL-N to the wind farm layout shown in Figure 4.1. This evaluation was made possible through two major components; that is, a comparison of the velocity and TI field, as well as a comparison of disk-averaged velocity and TI along the streamwise direction in the middle turbine row. In the former component, the quantities were computed and averaged over the wind farm width, in order to minimise transient phenomena from the LES dataset and capture global effects occurring in the wind farm.

It is also important to note that numerical instabilities and eventually divergence of the simulations were initially witnessed when the ABL-N model was employed. The presence of those instabilities has been previously reported in a single wake case by van der Laan et al. [57], yet there were no references regarding divergence. In the present case, the wake interactions between the wind farm and the free atmosphere are significantly more pronounced, subsequently amplifying numerical waves and preventing convergence. To that end, artificial mixing was introduced through a damping layer with $z_d/D = 20$,

as discussed in section 3.3, as a mitigation strategy. It was eventually proven that the numerical instabilities are alleviated by the high eddy viscosity of the damping layer and convergence of the simulations was achieved.

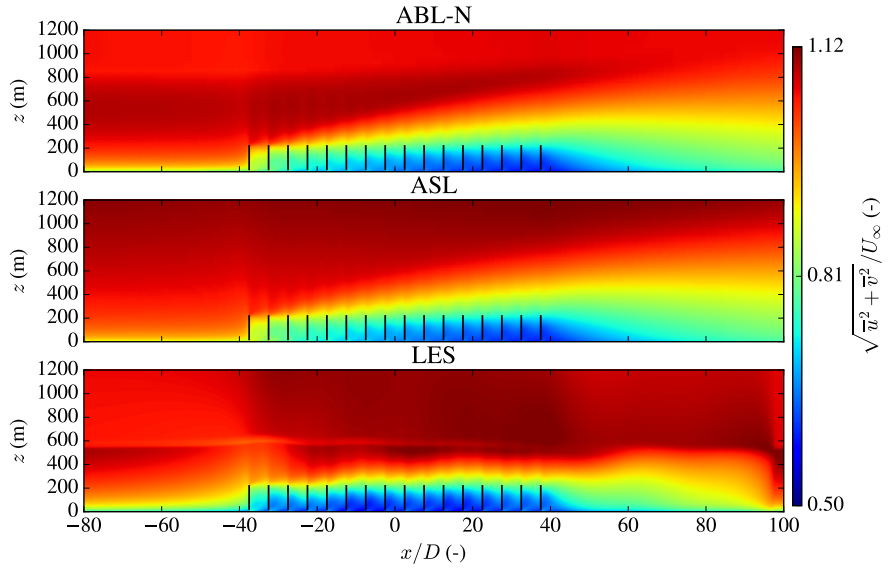

Figure 4.9: Comparison of the velocity field in the streamwise direction, averaged over the wind farm width between LES and RANS-based ABL-N and ASL models. Case H500 in correspondence with Table 4.2.

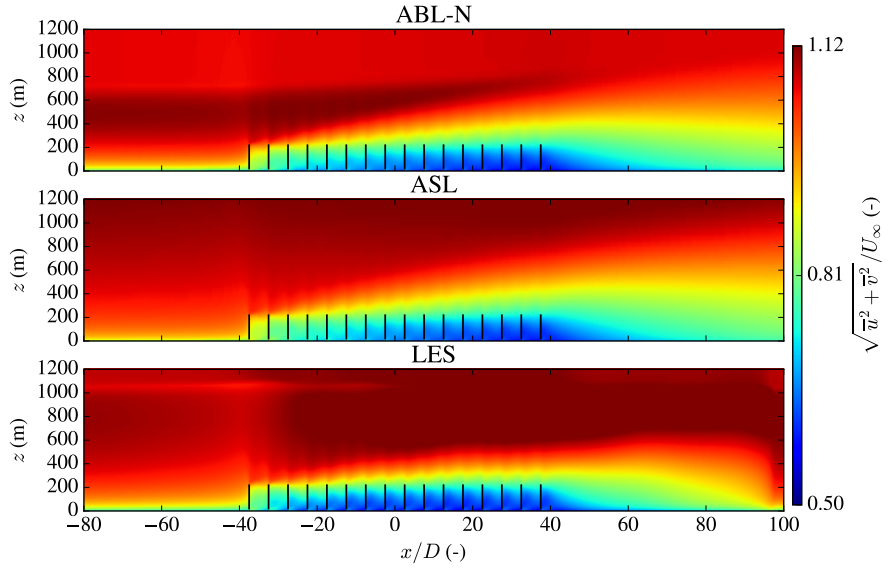

Figure 4.10: Comparison of the velocity field in the streamwise direction, averaged over the wind farm width between LES and RANS-based ABL-N and ASL models. Case H1000 in correspondence with Table 4.2.

Figure 4.9 and Figure 4.10 illustrate the velocity field for the cases H500 and H1000, while the deviations from LES are depicted in Figure 4.11 and Figure 4.12 respectively. The LES results reflect the presence of gravity waves, i.e. interactions between the highly turbulent wind turbine wakes and the stably stratified free atmosphere. As expected, in the shallow ABL case those interactions are magnified, due to the closer proximity between the capping-inversion and the wake region, which gives rise to downward energy entrainment from above the ABL. This is reflected by significant blockage effects (i.e. decelerated flow) in the induction and entrance region of the wind farm and speed-ups further downstream. From a wake perspective, this can be interpreted as enhanced wake effects in the entrance region, contrasted by a more rapid recovery and diminished wake effects further downstream, as discussed in chapter 2.

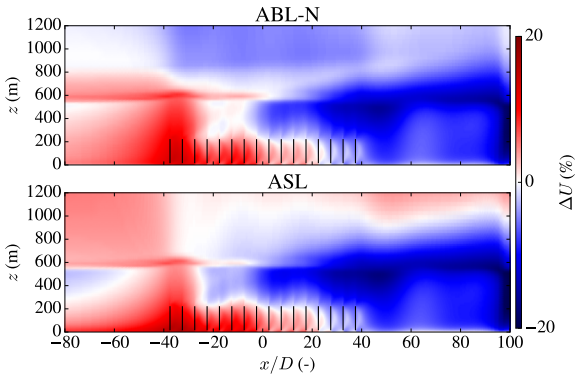

Figure 4.11: Comparison of the percentagewise difference in velocity field along the streamwise direction, averaged over the wind farm width between LES and RANS-based ABL-N and ASL models. Case H500 in correspondence with Table 4.2.

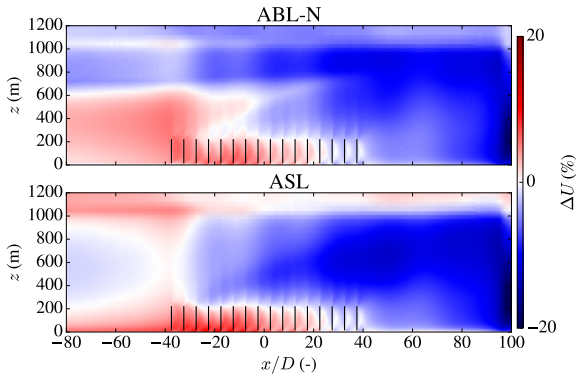

Figure 4.12: Comparison of the percentagewise difference in velocity field along the streamwise direction, averaged over the wind farm width between LES and RANS-based ABL-N and ASL models. Case H1000 in correspondence with Table 4.2.

Initially, at about $x/D = 100$ a fringe has been employed in the LES dataset, in order to force the flow field back to the one computed in the precursor domain. Therefore, a comparison in the region $x/D \geq 80$ is not realisable, since the LES velocity field is highly affected by the fringe forcing.

Highly transient phenomena such as the effect of gravity waves cannot be captured by steady RANS-based models such as ABL-N or ASL. It is evident that particularly in the shallow ABL case, where such mechanisms are more pronounced close to the wind farm, the deviations between RANS and LES are increased. In particular, overprediction of the velocity in the first few rows of turbines is observed, since the blockage effects are not modelled accurately. Similarly, the flow acceleration towards the exit region of the wind farm is underestimated by RANS. However, ABL-N was found to better represent the velocity field compared to ASL, as anticipated, especially for the deep ABL case.

Another source of deviations, was the difference in capping-inversion height between LES and ABL-N as discussed in the atmospheric inflow comparison. In summary, the order of magnitude of the discrepancies in velocity was quantified to approximately 15% at maximum.

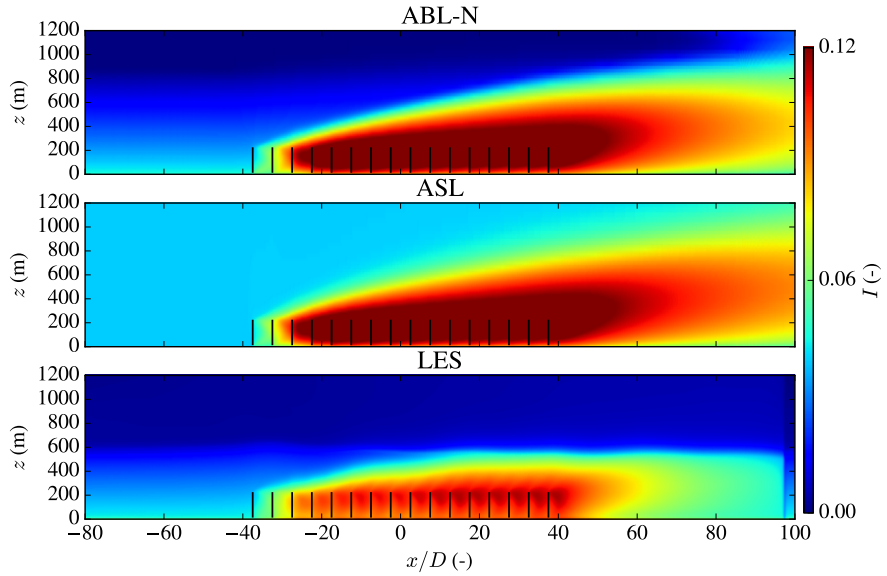

Figure 4.13: Comparison of the TI field in the streamwise direction, averaged over the wind farm width between LES and RANS-based ABL-N and ASL models. Case H500 in correspondence with Table 4.2.

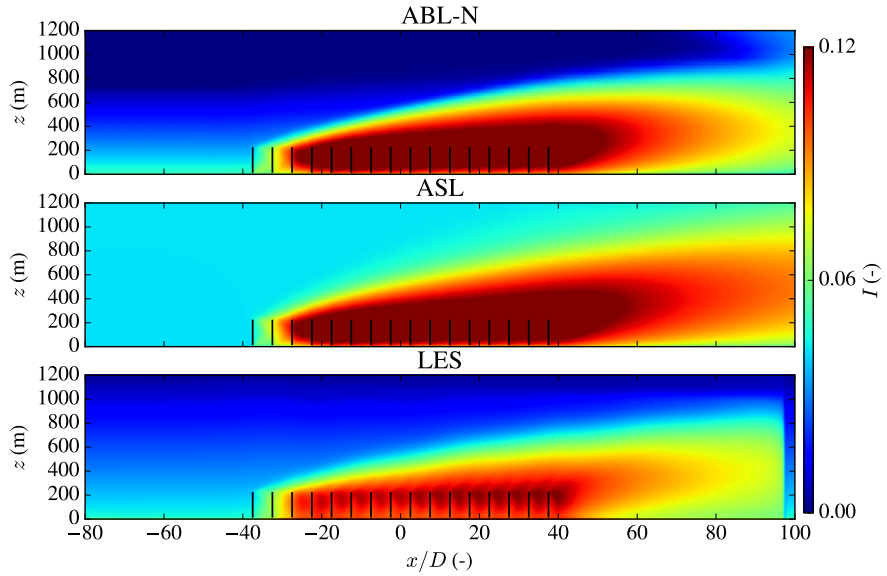

Figure 4.14: Comparison of the TI field in the streamwise direction, averaged over the wind farm width between LES and RANS-based ABL-N and ASL models. Case H1000 in correspondence with Table 4.2.

The TI fields for H500 and H1000 are demonstrated in Figure 4.13 and Figure 4.14 respectively, with Figure 4.15, Figure 4.16 showing the associated deviations. Contrary to the velocity field, as highlighted also in the single wake comparison, the TI one is significantly overpredicted by the RANS-based models, with the percentage-wise discrepancies being prohibitively large to support quantitative analyses. ABL-N shows, to some extent, improvements compared to ASL, which is expected, yet the overall picture indicates the shortcomings of linear eddy viscosity models (see (3.8)). Analogously to the velocity field, the stronger interaction between the turbulent wakes and the free atmosphere in the shallow ABL case is translated into larger discrepancies between LES and RANS.

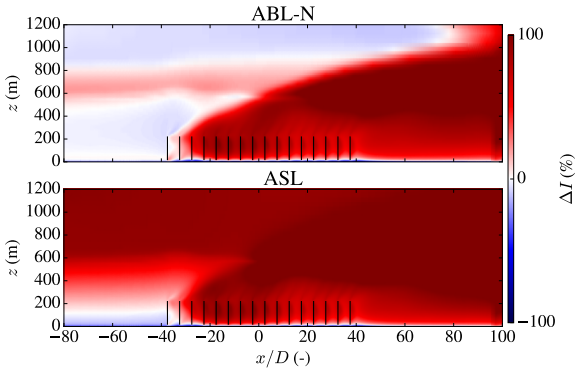

Figure 4.15: Comparison of the percentage-wise difference in TI field along the streamwise direction, averaged over the wind farm width between LES and RANS-based ABL-N and ASL models. Case H500 in correspondence with Table 4.2.

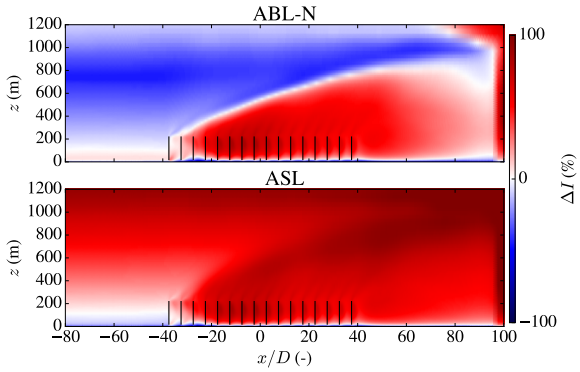

Figure 4.16: Comparison of the percentage-wise difference in TI field along the streamwise direction, averaged over the wind farm width between LES and RANS-based ABL-N and ASL models. Case H1000 in correspondence with Table 4.2.

Eventually, the downstream evolution of the streamwise velocity (U_{AD}) and TI (I_{AD}), averaged over the rotor disk area are provided in Figure 4.17 for the middle turbine row of the wind farm. Indeed, the velocity is more accurately predicted by RANS-based models in the tall ABL case, where the effects of gravity waves are weaker. The inability of ABL-N and ASL to resolve blockage effects in the entrance region of the wind farm causes overprediction of the velocity in the order of 10% and 5% for H500 and H1000 respectively. Similarly, the exit region, characterised by speed-ups, which RANS does not capture, shows approximately equivalent underestimations. The figure for TI exhibits a remarkable overall overprediction of more than 50% by RANS models in both flow cases. Unexpectedly, ABL-N and ASL have almost coinciding TI in the H500 case, whereas the difference between the two is marginal for H1000.

In summary, the velocity field is overpredicted in the induction and the entrance region and underestimated at the exit of the wind farm in both cases. The RANS results are found in better agreement with the LES for the deep ABL case (H1000). This is attributed predominantly to the diminished influence of gravity waves to the flow

close to the wind farm compared to H500. The differences in force method (discussed in subsection 4.2.2) and the differences in ABL height (discussed in subsection 4.2.1) have additional contributions to the deviations obtained. On the other hand, the TI is significantly overpredicted by RANS, due to the linear eddy viscosity assumption. Hence, the model cannot support quantitative analyses. Using a non-linear eddy viscosity to model the Reynolds stresses, such as the one proposed by Baungaard [7] has been shown to improve the prediction of TI, thus is recommended as an alternative.

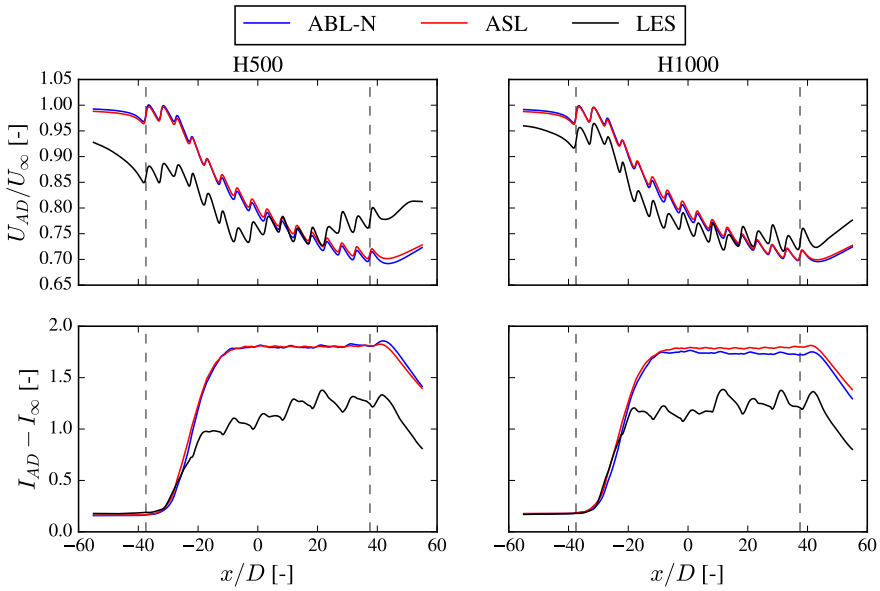

Figure 4.17: Comparison of disk-averaged velocity and TI along the streamwise direction, between LES and RANS-based ABL-N and ASL models. Case H1000 in correspondence with Table 4.2. The first and last turbines are denoted by grey dashed vertical lines.

4.3 Summary

This chapter aimed to compare the newly developed steady-state ABL-N model in RANS against LES results from the database of Lanzilao&Meyers [26]. The study attempted to resemble the rotor forcing strategy described in the corresponding publication [25] to isolate the effect of turbulence modelling by the model. The results showed overprediction of the velocity field in the induction and entrance region of the wind farm and underestimation towards the end of the wind farm. This is attributed to the presence of gravity waves in the LES dataset, which the RANS model cannot resolve, the deviations in force method between the different software and the slightly different ABL heights predicted by the models. The gravity wave effects are less pronounced in the deep ABL case, hence the results are in better agreement. Conversely, the TI field is significantly overpredicted, presumably owing to linear eddy viscosity models' shortcomings in computing the Reynolds stresses and thus the TKE. It was concluded that the model is not suited for quantitative analysis of TI.

CHAPTER 5
Effect of Vertical Staggering

In the present chapter RQ2 is dealt with. As discussed chapter 1, the concept of installing large-scale turbines (both in terms of hub height and rotor size) into an already existing wind farm, has not been yet explored. Therefore, the current chapter aims to demonstrate the effect of vertical staggering, by means of numerical simulations, through a simplified case study tailored to the German onshore wind standards.

The proposed study entails two core objectives; firstly, to assess the deviations in flow phenomena between vertically-staggered layouts with various hub heights and a baseline arrangement without multi-scale turbines. As such, the impact of implanting new large-scale turbines on their smaller counterparts in terms of power production and wake-added TI (and therefore fatigue loads) may be revealed, providing further understanding and expertise for siting applications. Besides, relatively larger hub heights of the tall turbines may minimise the rotor overlap and thus demonstrate less power losses (refer to chapter 1), yet this could increase the production cost of the turbine towers and potentially cause complications related to visual impact. To that end, obtaining insights on the relative differences between vertically-staggered setups with varying hub heights of the tall turbine is of major importance to balance this trade-off.

Initially, the numerical setup and the argumentation for the choices regarding the grid, force method, layout, and flow cases are presented. Thereafter, the results of the assessment are illustrated and analysed.

5.1 Wind farm setup and coordinate system

The study summarised previously endeavours to resemble German onshore wind farms. As per the assessment by Vestas Wind Systems A/S, these are characterised by tight turbine interspacing i.e. less than 5 rotor diameters in both the streamwise and spanwise direction, emphasising the importance of understanding the wake interactions occurring within wind turbine clusters.

Numerical simulations of wind farms, even with steady-state RANS, require significant computational resources with the computational time increasing dramatically when relatively larger configurations are of interest. Therefore, several simplifications were necessary in the present analysis, in order to balance the trade-off between adopting a realistic layout and preventing excessively high computational times. To that end, a

4x4 grid, shown in Figure 5.1, was initially realised as the control wind farm case for simplicity. It comprises only baseline wind turbines in a horizontally-aligned arrangement with tight inter-spacing, especially 5 and 2.5 rotor diameters in the streamwise and spanwise direction respectively, consistently to that of typical German plants. Similarly, the vertically-staggered layout is realised by erecting larger-scale machines (both in rotor size and hub height) in the control wind farm. The coordinate systems for the current study is defined as per Figure 5.1 and Figure 5.2 in Cartesian and polar coordinates respectively (the latter is necessary for the definition of wind direction).

Two main considerations were made for the collocation of multi-scale wind turbines. Firstly, the wind farm area defined by the baseline turbines was kept the same, to imitate realistic cases where additional land leasing for the installation of the large turbines may be challenging. Secondly, the new turbines were also placed in horizontal alignment with the ones already installed. Horizontally-staggered configurations are in principle more favourable, with multiple studies (refer to chapter 1) highlighting reduction of wake effects compared to aligned cases. Yet, the present study aims to quantify the flow phenomena in the most adverse wake conditions, hence an in-series layout is more suitable for that purpose. Eventually, the resulting vertically-staggered wind farm is defined by a 2.5 rotor diameter distance between wind turbines in both spanwise and streamwise directions as shown also in Figure 5.1. Note that the turbine interspacing is parametrised with respect to the rotor diameter of the relatively smaller-scale turbines.

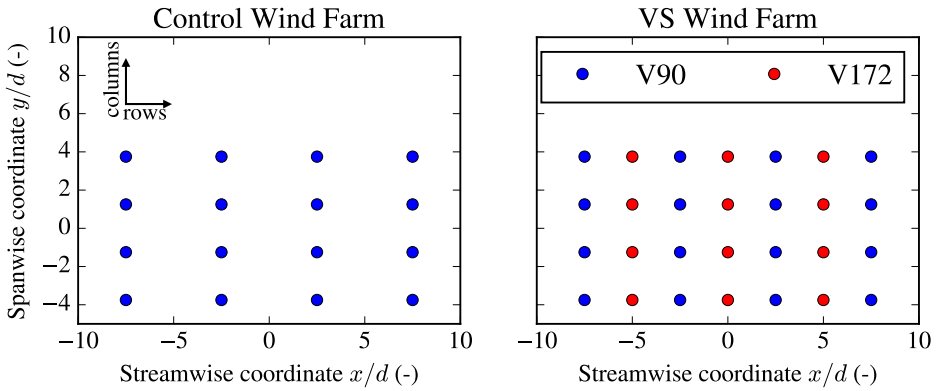

Figure 5.1: Schematic of the wind turbine locations in the control (left) and vertically-staggered (right) wind farms, representative of the German onshore market. The streamwise and spanwise coordinates are normalised with respect to the rotor diameter of the smaller-scale turbines Vestas V90, i.e. $d = 90$m. Turbine rows and columns are defined in the streamwise and spanwise direction respectively.

Consistently to Figure 5.1, in order to model realistic turbine performance to the highest extent possible, proprietary data of the Vestas V90 are utilised to represent the lower hub height (baseline) turbines. The rotor diameter, hub height and rated power are fixed to $d = 90$ m, $z_h = 80$ m and 1.8 MW respectively. Similarly, Vestas V172 was used as the

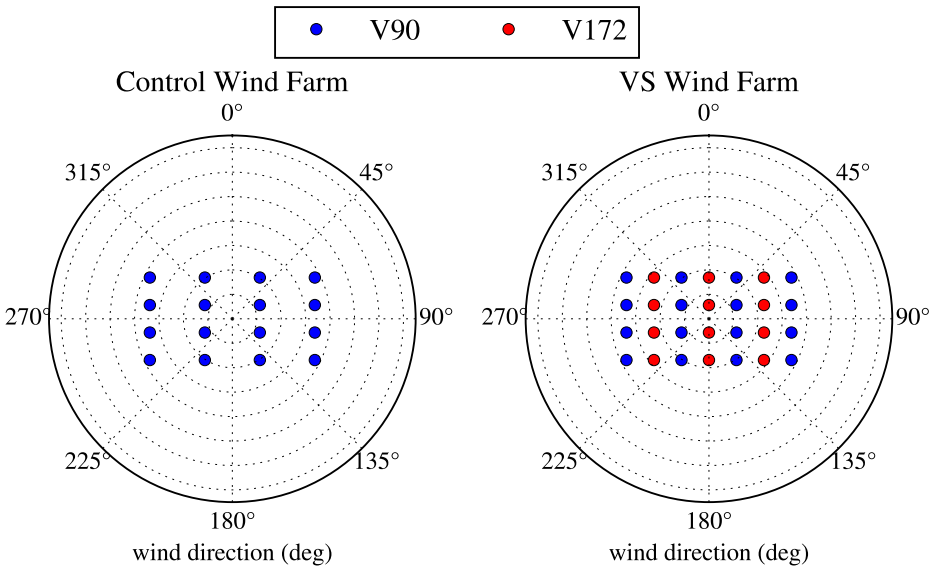

Figure 5.2: Schematic of the wind farm layouts in a polar coordinate system for the definition of wind direction: control (left) and vertically-staggered (right) wind farms.

larger turbine, with a rotor diameter of $D = 172$ m, and 7.2 MW of nominal power and variable hub height (z_H). Note that performance details for these two turbines cannot be published.

Relative differences between different vertically-staggered setups are to be identified for the reasons explained previously. To that end, three vertically-staggered configurations were examined beyond the control case, where the hub height of the small turbines is constant, whereas the one for the larger turbines (z_H) is varied. The configurations under consideration are summarised in Table 5.1. The parametrisation of all three cases was made possible through the blade overlap ratio (BOR) of the baseline turbines, defined in the present work as,

$$\mathrm{BOR} = \frac{H_{\mathrm{overlap}}}{d} \times 100 \tag{5.1}$$

wherein, H_{overlap} is the vertical distance of the geometrically overlapping section of the V90 turbine blades with the newly installed ones, while d is the rotor diameter of the V90. This measure will simplify the investigation of multiple partially overlapped cases and allow comparison to a non-overlapping rotor scenario. In particular, as summarised in Table 5.1 and visualised in Figure 5.3, through appropriate hub height adjustments of the large-scale turbines (Vestas V172) the three cases of interest feature partial overlap with BOR of 50%, 25% and 0% (i.e., no geometrical overlap) respectively.

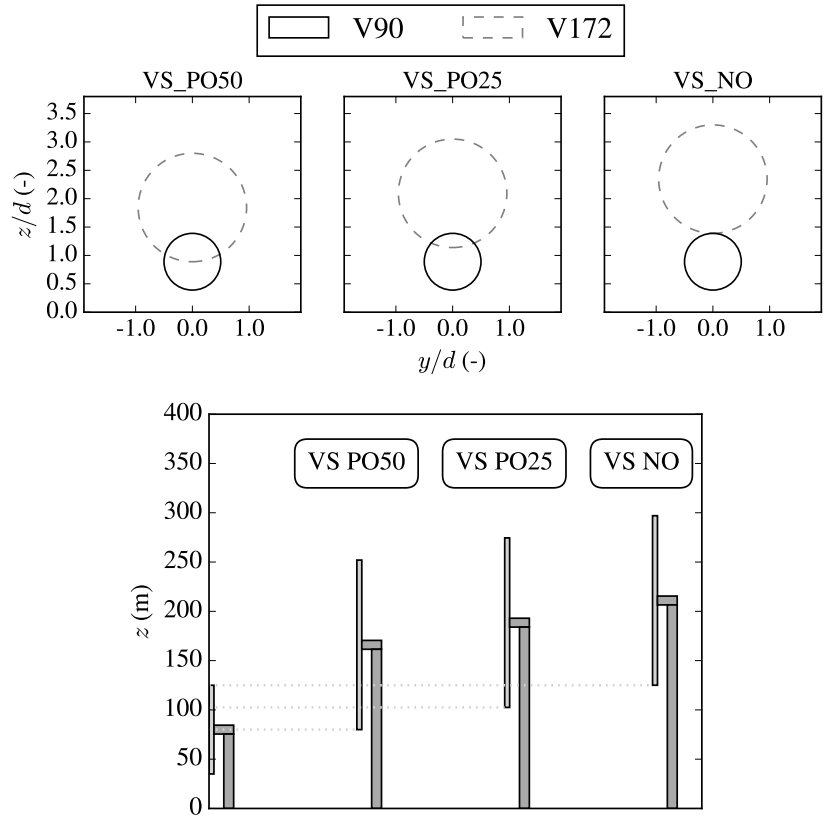

Figure 5.3: Schematic of the rotor vertical overlap in the vertically-staggered configurations under consideration, parametrised with respect to the blade overlap ratio (BOR), in accordance with Table 5.1. Rotor overlap per configuration on a spanwise plane (upper) and hub height for each turbine type per configuration on a vertical plane (lower).

Table 5.1: Examined flow cases parametrised with respect to the blade overlap ratio (BOR). z_h and z_H represent the hub heights of the short (baseline) and the newly installed tall turbines respectively.

Configuration	BOR (%)	Hub height ratio z_H/z_h (-)	Total nominal power (MW)
control	-	-	28.8
VS PO50	50%	2.075	115.2
VS PO25	25%	2.356	115.2
VS NO	0%	2.638	115.2

5.2 Site and inflow conditions

AEP calculations are conducted in the current chapter. The wind resource input parameters are based on meteorological mast measurements. In particular, ten years of 10-min average wind speed measurements are used. These have been performed at the onshore test centre Høvsøre on the west coast of Denmark owned by DTU using a sonic anemometer at a height of 100m, which is fairly representative of the reference height of the small turbines i.e., $z_h = 90$ m. According to Vestas Wind Systems, these wind conditions are thought analogous to a site located in northern Germany. The fitted Weibull distribution, shown in Figure 5.4, is used to define the wind speed probability in AEP calculations, assuming a uniform probability distribution for the wind direction.

In RQ1 (refer to chapter 4) the analysis was focused on offshore wind conditions with the ambient mean TI being around 4%. On the contrary, onshore sites are known to experience higher ambient turbulence levels [8] than those offshore, therefore the ambient TI was increased in the assessment presented in the current section. In particular, TI is kept constant at $I_\infty = 10\%$ at z_h for all wind speeds and wind directions for the sake of simplicity. As demonstrated in Figure 5.4, turbulence measurements in Høvsøre verify that this assumption is fairly representative of mean wind speeds above 6m/s, yet it is not valid for lower values, where a significant increase in mean TI is witnessed. Nevertheless, the impact of these wind speeds on the AEP is assumed negligible. The reason is that the abovementioned wind speed range is fairly small, whilst it lies very close to cut-in, hence some turbines may still be parked. It is also important to mention that the mean turbulence intensity is slightly less in Høvsøre (around 8%). Yet, this corresponds to a coastal area where turbulence is relatively lower than an area further inland, which is the objective of the study.

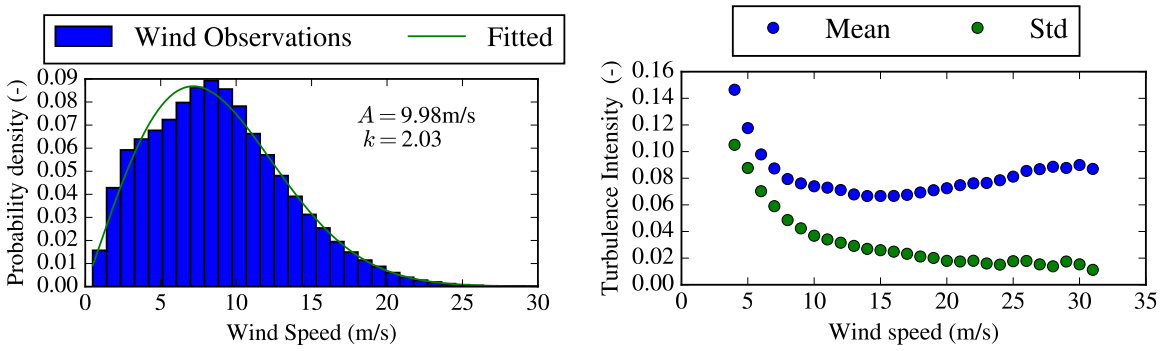

Figure 5.4: 10 years of simultaneous wind speed and turbulence measurements at the onshore test centre Høvsøre on the west coast of Denmark owned by DTU. Measurements performed using sonic anemometer at a height of 100m.

Surface roughness is an important parameter in wake recovery and added turbulence as per Chamorro et al. [12], with onshore terrains being rougher than offshore [8]. Hence,

the roughness length was fixed to a representative value of $z_0 = 0.1$m [41].

The precursor implemented for the analysis was generated in EllipSys1D using the ABL-N inflow model following the method described in section 3.3. Assessing the interference between the free atmosphere above the ABL and the turbine rotors of the Vestas V172 was not in the scope of the present work. Therefore, the ABL height was determined accordingly such that all turbines operate within the ABL and sufficiently far from the ABL top. As mentioned previously (see Figure 3.1), the ABL height is controlled purely by the roughness length (z_0) assuming constant TI and wind speed at hub height. The terrain roughness value mentioned previously (z_0 =0.1m), produces an ABL of about 1 km as seen in Figure 5.5, hence it is sufficient for that purpose.

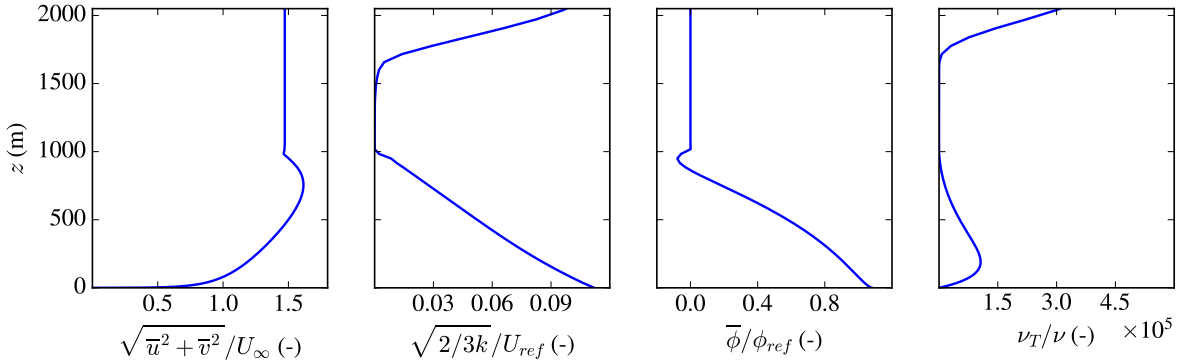

Figure 5.5: ABL profile generated with $I_\infty = 10\%$, $z_0 = 0.1$m, through 1D precursor simulations in PWE. The effect of the damping layer is reflected by the rapid increase of viscosity ν_T and TI at high altitudes ($z \geq 1700$ m). The veer angle is normalised by the same angle probed at hub height $z_h = 80$ m.The resulting ABL height is around 1 km.

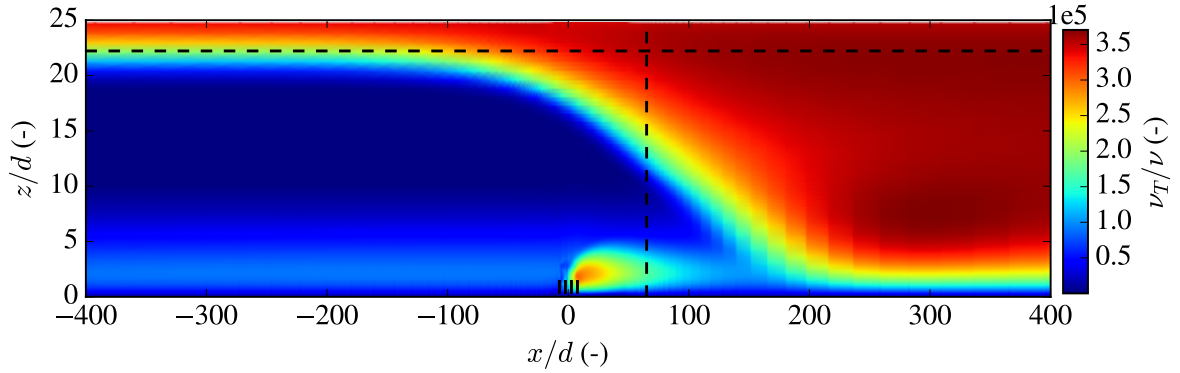

Figure 5.6: Spanwise-averaged normalised eddy viscosity field in the vertical plane of the wind farm domain. The starting streamwise location and height of the damping layer are denoted with black dashed lines.

A damping layer was also employed in both the precursor and the 3D wind farm domain to alleviate numerical instabilities (see chapter 3) and is visualised for the former in Figure 5.5 and for the latter in Figure 5.6. The starting height and streamwise distance were set to $22d$ above the ground and $50d$ behind the last turbine row respectively, such that it does not interfere with the flow close to the wind farm.

5.3 Numerical setup

Table 5.2: Grid sizing parameter values for RQ2, normalised by the rotor diameter of the small turbines

Parameter	Normalised Value
Outer domain	
grid_Dref	$d = 90$m
grid_radius_D	500
grid_zlen_D	25
grid_zFirstCell_D	0.005
Wake refinement region	
grid_cells1_D	8
grid_m1_w_D	5
grid_m1_e_D	20
grid_m1_n_D	2
grid_m1_s_D	2
grid_zWakeEnd_D	$(max(z_H) + D/2)/d + 2.0$
AD polar grid	
adgrid_nr	64
adgrid_ntheta	64

All configurations outlined in Table 5.1 were simulated with the same numerical grid, in order to obtain comparable results. The grid sizing employed in this investigation is described in Table 5.2. The scaling of the grid was done with the small turbine rotor diameter d. The current discretization differentiates in three aspects from the one utilised in RQ1 with respect to the wake refinement region: firstly, the wake domain height was chosen such that it covers the tallest turbine rotor (see VS_NO) plus two diameters above its upper tip. This was needed in order to capture the upward wake expansions. Secondly, the horizontal dimensions of the wake domain were decreased owing to the smaller number of turbines compared to chapter 4. Thirdly, the wake domain spacing was set to 8 cells per diameter which is the minimum requirement [58] to minimise the computational expenses for AEP calculations. This grid size was found of sufficient accuracy within 2.5 rotor diameters downstream (see Figure 3.4), which is the streamwise turbine interspacing

defined in the simulated wind farms. Eventually, the resulting blockage ratio in the worst case scenario (VS_NO) was quantified to $\pi(D^2 + d^2)/(1000d \times 25d) = 0.06\%$.

The boundary conditions employed are outlined in chapter 3. In addition, the convergence criterion in the current analysis was set to a residual of 10^{-4}. A threshold of 10^{-5} could be argued for, yet the relative error in terms of AEP has been found in the order of 0.01% [52], while the computational cost is significantly higher. Hence, it was not preferred for this analysis.

Similarly to chapter 4 the same AD method is employed to represent rotor forcing in the numerical domain i.e., non-rotating actuator disks with uniform force distribution. The absence of rotation and thus azimuthal forcing was chosen, in order to isolate the flow deflection due to Coriolis and its effect on power production. In addition, in the current analysis, absolute power figures are of interest, therefore force calibration is implemented for multiple AD force treatment (refer to Equation 3.16).

5.4 Results and Discussion

This section provides a presentation and discussion of the main findings from the analysis. The flow properties of the flow cases outlined in Table 5.1, are first examined in terms of the velocity field, turbulence intensity and wake recovery in different regions. Subsequently, the analysis focuses on power production; the effect of vertical staggering on individual turbine performance as well as wind farm power and AEP is assessed.

5.4.1 Velocity field

The resulting velocity field for the analysed cases is shown in Figure 5.7 for a free-stream wind speed of U_∞ =10 m/s in the main wind direction (270 degrees in Figure 5.2), where rotor interactions are maximised. The graphs **(a-d)** depicts the spanwise-averaged velocity over the wind farm width, whereas the ones **(e-h)** show the same quantity plotted in a horizontal plane at the level of the small turbines' hub (z_h =80m). Turbine size heterogeneity induces flow phenomena that are not observed in the homogeneous case (i.e., control wind farm), as expected from existing research [12] and are analysed below.

Initially, the upstream region of the wind farms is dominated by blockage effects in all flow cases as discussed in chapter 2. These effects are remarkably amplified with the addition of new larger-scale turbines (V172) and their distribution varies when z_H changes; higher geometrical overlap between the two different types of turbines introduces stronger flow deceleration upstream and around the level of V90, whereas when the geometrical overlap reduces, the additional deceleration stemming from the tall turbines is shifted upwards as seen in Figure 5.7(d). Even in the non-overlapping VS scenario (VS_NO), where minimum blockage is witnessed among the other VS cases (see graph (h)), the flow velocity was still reduced more than in the control wind farm. The associated power losses in the first row of small turbines are quantified and discussed in subsequent section.

Further downstream in the wind farm, where the energy extraction from the wind turbines happens, lies the entrance and development region. Vertical staggering leads to significant differentiation of the flow features within the wind farm from the control case. The velocity deficits for both types of turbines were more pronounced, particularly for higher geometrical overlap, owing to stronger wake interactions. This result is in agreement with findings from the literature ([14], [20], [13]). The general morphology of the velocity distribution is similar among the VS arrangements, although the magnitude experiences substantial variations.

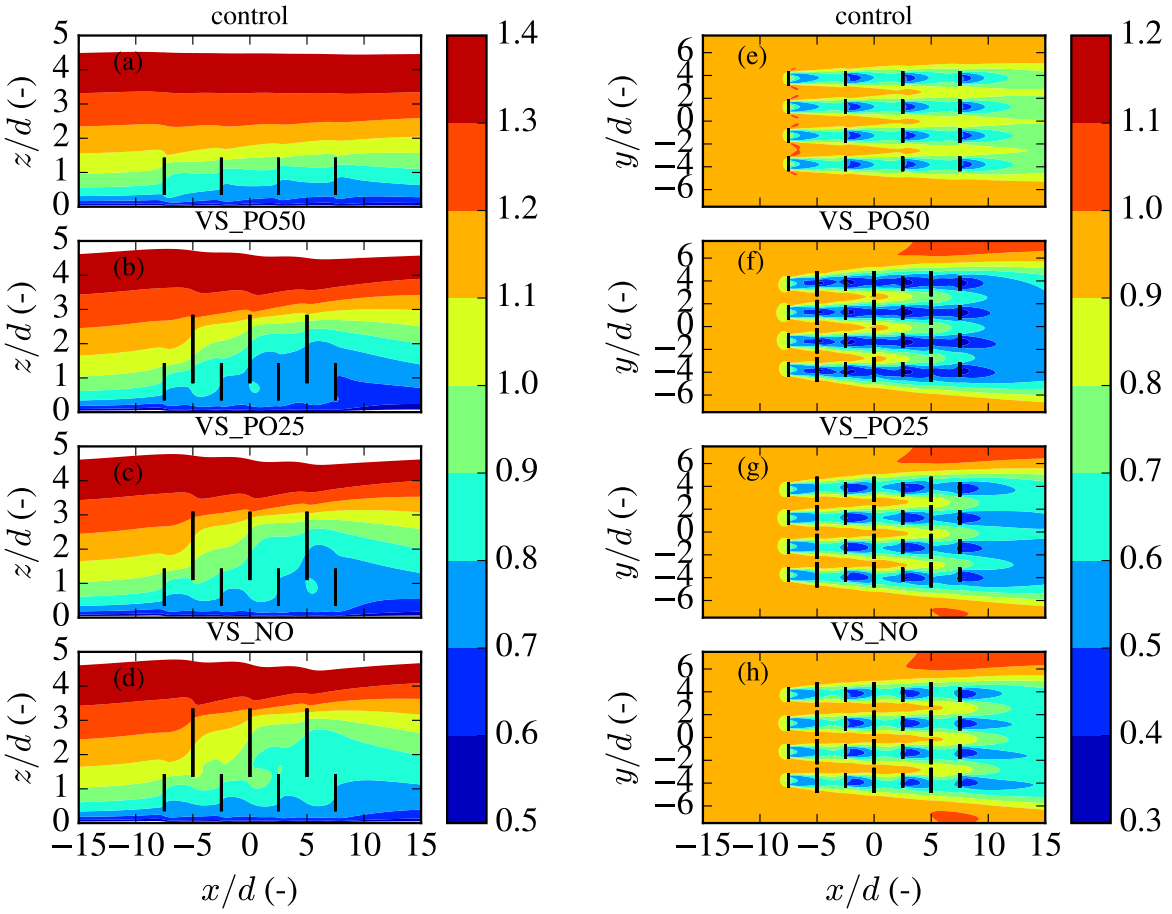

Figure 5.7: Velocity field for U_∞ =10m/s and 270° (main wind direction case) corresponding to the flow cases summarised in Table 5.1. Spanwise-averaged velocity field in the vertical plane (**a-d**) and velocity field at hub height of V90 (z_h =80m) (**e-h**). The rotor disks are denoted with black lines.

Two competing effects can be identified; the first is the additional energy extraction from the large turbines (inducing stronger wake deficits) and the second is the additional flow acceleration between them, due to close interspacing in the spanwise direction. This feature of the layouts confines the local flow, which speeds up in the region among

consecutive turbine columns (better seen in Figure 5.7 (e-h)); this effect is augmented for the VS cases, as the spanwise clearance between the tall turbine rotors is smaller. Interestingly, the VS_NO configuration showed that the abovementioned accelerated flow extends further into the wind farm than in the control case at the horizontal plane taken at z_h.

Coriolis forces also impact the air within the wind farm boundaries. As a result, the flow is non-symmetric around the longitudinal axis of the wind farm (i.e., x-direction) with the wakes at $y/d > 0$ recovering faster. This is expected to cause column-wise turbine power variability (discussed in later section). It is important to highlight that, in general, flow asymmetry could be also caused by wake rotation stemming from the azimuthal rotor forcing. Yet, this is not the case in the present analysis, as non-rotating actuator disks were implemented. Again, the effect of Coriolis is more visible in the VS cases, where the overlapping wakes induce detrimental flow decelerations compared to the control wind farm.

The cumulative effect of Coriolis forces and the hub height of the large turbines is demonstrated through the flow acceleration recorded at $x/d \geq 5$ and $y/d \approx 6$ in the VS cases. The former effect compels more flow towards one side of the wind farm, and therefore that speedup region is developed. The latter effect controls the velocity magnitude within that region; increasing the hub height of the larger turbines forces more air laterally and around the wind farm than above it (specifically focusing on the horizontal plane at the hub height of the small turbines). For that reason, the speedup region was more pronounced when the larger turbines were placed at maximum height. This is expected to improve the power production of the last row of small turbines. On the other hand, the lack of larger turbines in the control wind farm leads to insignificant flow accelerations in the abovementioned region.

Eventually, it has to be mentioned that due to the limited size of the wind farm and the tight spacing, the flow cannot fully adapt to the presence of the wind turbines, hence there is no formation of either the fully developed or the exit region, as described in chapter 2.

5.4.2 Turbulence intensity

A similar illustration to the preceding discussion is demonstrated in Figure 5.8 but now for the turbulence intensity field. Higher turbulence intensities mean more turbulent mixing, enhancing the energy entrainment from the undisturbed flow towards the waked flow regions. On the other hand, turbines subjected to high turbulence intensity e.g., due to the presence of upstream turbines, encounter amplified fatigue loads.

Similarly to the velocity field, vertical staggering causes considerable changes in the TI field compared to the control case. Qualitatively, graphs (e-h) show that the overall distribution of the TI is similar for all three VS configurations, whereas the magnitude is

hub height dependent. As expected, decreasing the hub height difference (i.e., increasing the geometrical overlap) between the two types of turbines introduces more added turbulence downstream. The spanwise-averaged TI field in the $x-z$ plane (Figure 5.8 (a-d)) also showed that turbulence generation is dominated by the larger turbine rotors, since they produce more significant coherent structures. To put into perspective, the last turbine row experiences turbulence intensities that are double the ambient value, which is likely to cause fatigue problems and would need further structural investigation.

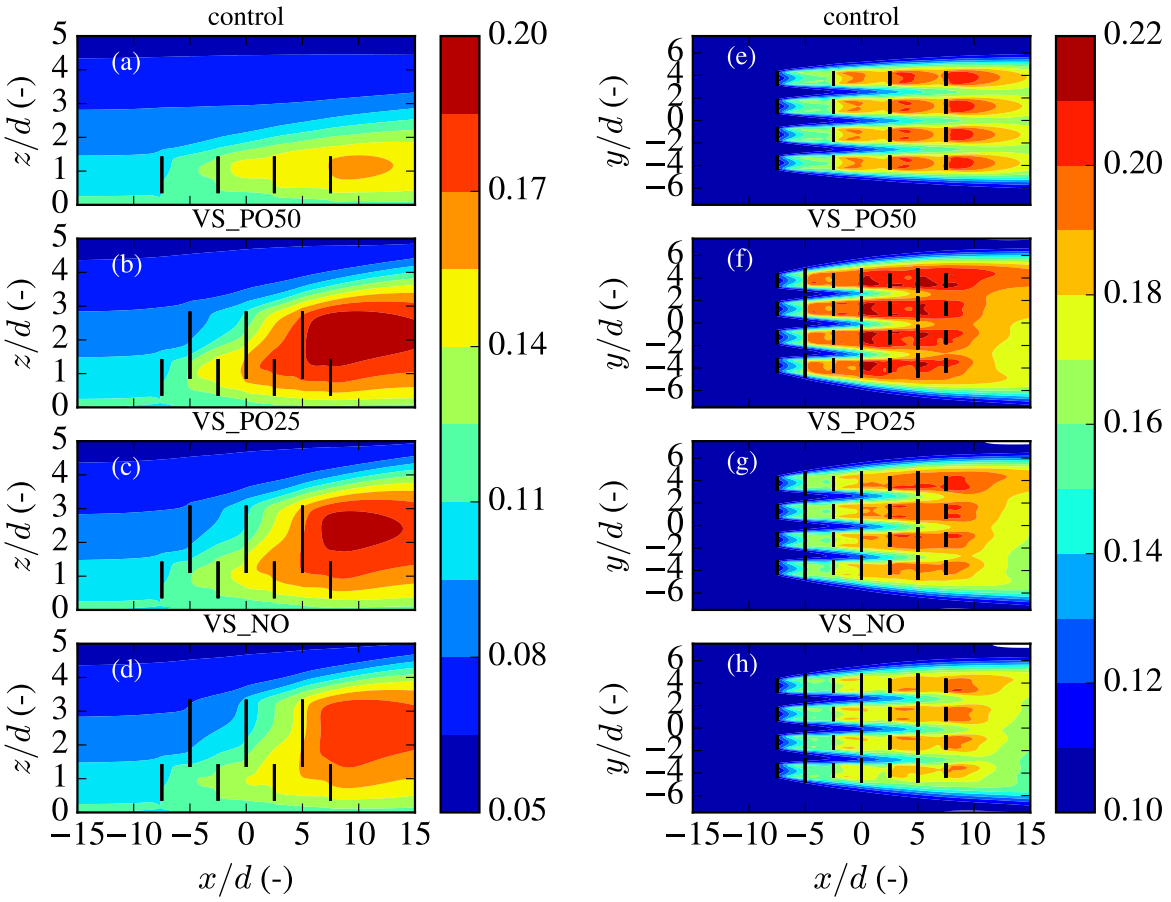

Figure 5.8: Turbulence intensity field for U_∞ =10m/s and 270° (main wind direction case) corresponding to the flow cases summarised in Table 5.1. Spanwise-averaged TI field in the vertical plane (**a-d**) and TI field at hub height of V90 (z_h =80m) (**e-h**). The rotor disks are denoted with black lines.

In addition, the flow perceived by the small turbines was clearly more turbulent in the VS cases than in the control wind farm. This is an expected outcome of the study due to the wake superposition between the two turbine scales and given their tight interspacing. Counterintuitively, when the turbine rotors do not overlap geometrically (Figure 5.8(h)), the turbulence intensity at the hub of the small turbines was slightly less than in the

control case, even though an average over height shows the opposite. As extensively discussed previously RANS models are not accurate in predictions of TKE and thus TI. Hence, this result should be further investigated with higher fidelity modelling e.g., LES.

Coriolis forces once again contribute to flow heterogeneity, which is most evident in the VS cases in the horizontal plane. The TI is significantly higher for $y/d > 0$ than its symmetric counterpart, particularly in the wake of the wind farm. This increased turbulence gives rise to momentum transport from the undisturbed flow around the wind farm. This finding is consistent with the observations discussed in the preceding comparison of the velocity fields, where wakes were found to recover faster in that region.

Eventually, in chapter 4 several remarks were provided regarding the reliability of eddy-viscosity models, such as the one currently employed. It was mentioned that the limitations of such models are most noticeable in TI predictions. Consequently, the present TI analysis is intended solely to capture global features; it is, however, not suited for accurate quantification of the TI distribution. Further research is recommended, using higher fidelity simulation tools i.e., LES.

5.4.3 Wake convection & recovery

The momentum transport towards the low energy wakes from the surrounding area i.e., wake recovery, is hereby investigated. Indicative of wake recovery processes is the spatial variation of the Reynolds stresses, also referred to as stress divergence [53], therefore it is employed as the quantity of interest. In the present analysis, wake recovery is studied in the lateral and vertical directions; that is, sideways and top-down flow entrainment respectively. The contribution of the former in the momentum balance is reflected by $\frac{\partial \overline{u'v'}}{\partial y}$, whereas the corresponding quantity for the latter is $\frac{\partial \overline{u'w'}}{\partial z}$.

In Figure 5.9 the wake recovery is contrasted for all the simulated wind farm arrangements. Graphs (a-d) indicate the amount of momentum transported in the vertical direction towards the hub plane of the turbines. In contrast, graphs (e-h) illustrate the momentum recovery from the sides at the hub height of the small turbines.

Several interesting observations can be made: more complex momentum transport phenomena, and thus wake recovery are exhibited due to the large turbines' addition (VS configurations) compared to the control. When the large turbines are added, the most momentum gains in the vertical direction are obtained, contrary to the single hub height setup, along the rotor area of the larger turbines, particularly in the last two large turbine rows, where the momentum deficits are the largest. More pronounced momentum losses for the small turbines are recorded for the VS_PO50 arrangement. This effect diminishes with decreasing rotor overlap. Similar observations can be made for the lateral direction. Lateral recovery extends in larger downstream distances at the wind farm wake region when rotor overlap decreases. The flow between the turbine rotors experiences the most significant momentum losses; this lost momentum is transferred sideways to the turbine

wakes. Higher rotor overlap considerably enhances this feature. Also, more of the outer flow is affected in the VS configurations with stronger rotor overlap, as in those wind farms the energy extraction by the turbines is considerably more pronounced.

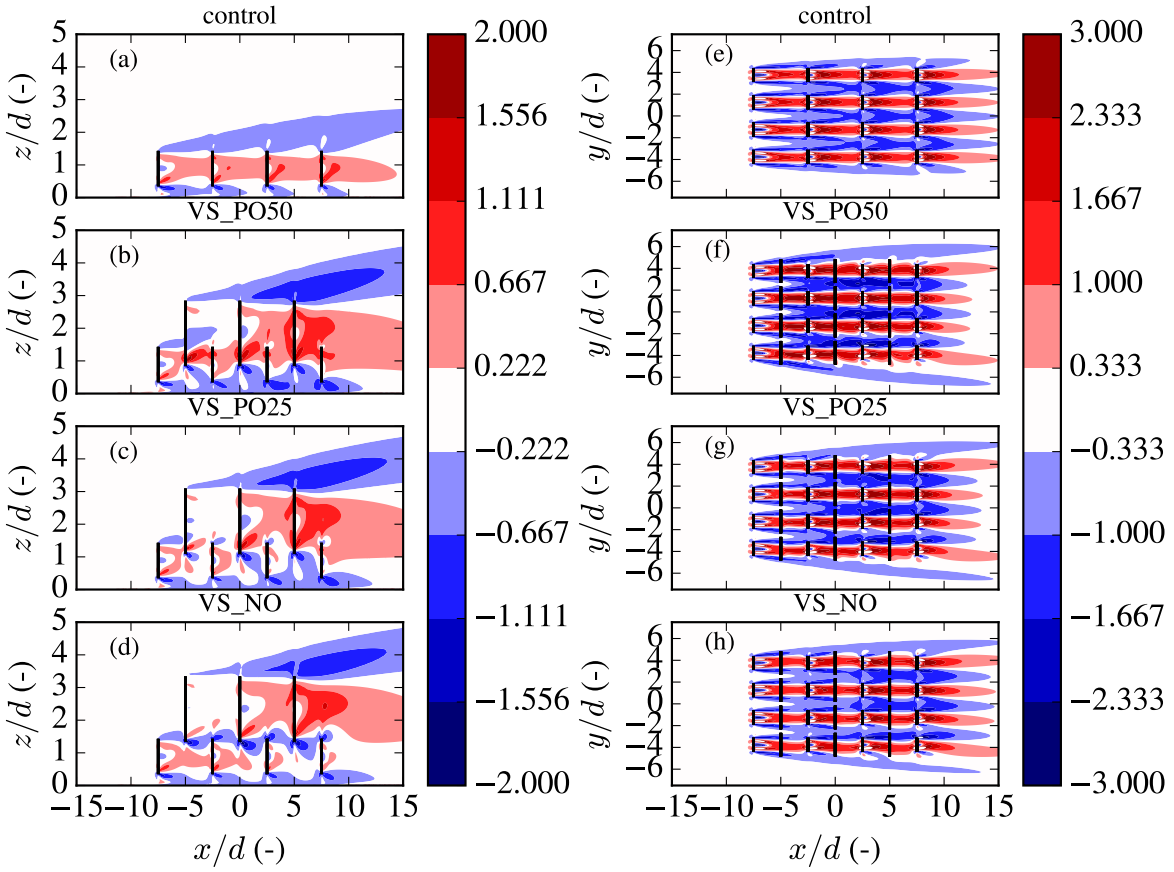

Figure 5.9: Reynolds stress divergence field for U_∞ =10m/s and 270° (main wind direction case) corresponding to the flow cases summarised in Table 5.1. Spanwise-averaged Reynolds stress divergence field in the vertical plane i.e., $-\frac{d}{k_{ref}}\frac{\partial \overline{u'w'}}{\partial z}$ (**a-d**) and Reynolds stress divergence field at hub height of V90 (z_h =80m) i.e., $-\frac{d}{k_{ref}}\frac{\partial \overline{u'v'}}{\partial y}$ (**e-h**). k_{ref} is the free stream TKE probed at z_h. The rotor disks are denoted with black lines.

Insights on wake recovery can also be obtained by comparing vertical profiles of the velocity TI and stress divergence, spanwise-averaged over the wind farm width, as visualised in Figure 5.10. As the flow evolves into the wind farm, consecutive turbine rows extract more energy from it. Hence, the associated velocity deficits are increasingly larger within the wind farm. Despite that high shear within the wind farm, the flow recovers and therefore the gradients diminish as the flow leaves the wind farm area ($x/d = 10$). Flow entrainment or in other words vertical expansion of the wakes is indicated as the mean velocity deficit, TI and stress divergence profiles extend further upwards in larger downstream distances. The wakes of small turbines in vertically staggered arrangements

are influenced by the wakes of the large turbines. This interaction results in different wake recovery behaviours compared to when the small turbines are in a single hub height arrangement (i.e., control). The velocity deficits, particularly in the overlapping area of the two rotor types, are significantly increased in the VS configurations; this effect is more pronounced in VS_PO50 with maximum overlap. Hence, diminished turbine performance is expected in comparison with the control and the other VS setups. Interestingly, at $x/d = 6.25$ i.e., past the third couple of large and small turbine rows in the wind farm, the flow at the lower part of the small rotor ($z/z_h \leq 1$) is faster in the VS_NO than the control case. Likewise, the small turbines may be thought of as roughness elements for the larger ones. In other words, they vary the effective roughness that the larger turbines are subjected to; this roughness grows with increasing geometrical overlap, thereby exposing the large turbines to relatively slower and more sheared wind speeds. It can be therefore expected that the performance of the tall turbines will also deteriorate as a result of higher overlap with their smaller counterparts.

The figure for TI demonstrates that highly overlapping rotors in VS wind farms also introduce relatively higher turbulence levels in downstream turbines. The small turbines are, in general, subjected to augmented turbulence than in single hub height cases. Consequently, as highlighted previously, it is more likely to experience structural problems related to fatigue loads. VS_NO shows almost coinciding TI along the rotor area of the small turbines, yet it is considerably higher above, owing to the presence of the large turbines. It is worth mentioning once again that these trends, despite they seem physically reasonable, they are not to be fully relied on due to the limitations of eddy viscosity models to predict the TI field.

Lastly, the significant alternations of the vertical wake recovery mechanisms in VS configurations are profound. In the control wind farm, momentum gains at the wake region of the small turbines mainly come from above. However, this is not the case in VS configurations. In particular, hub-height heterogeneity causes upward momentum transport from the rotor area of the small turbines, which is transferred towards the large turbines' waked region. This effect is more evident in VS_PO50 where rotors overlap maximally, and at $x/d = 6.25$ i.e., further into the wind farm. Presumably, this is because the large turbines extract relatively more energy than the small ones. In other words, the flow across the small rotor area is relatively more energetic than the flow around the large one, hence large turbines steal this energy from the small ones.

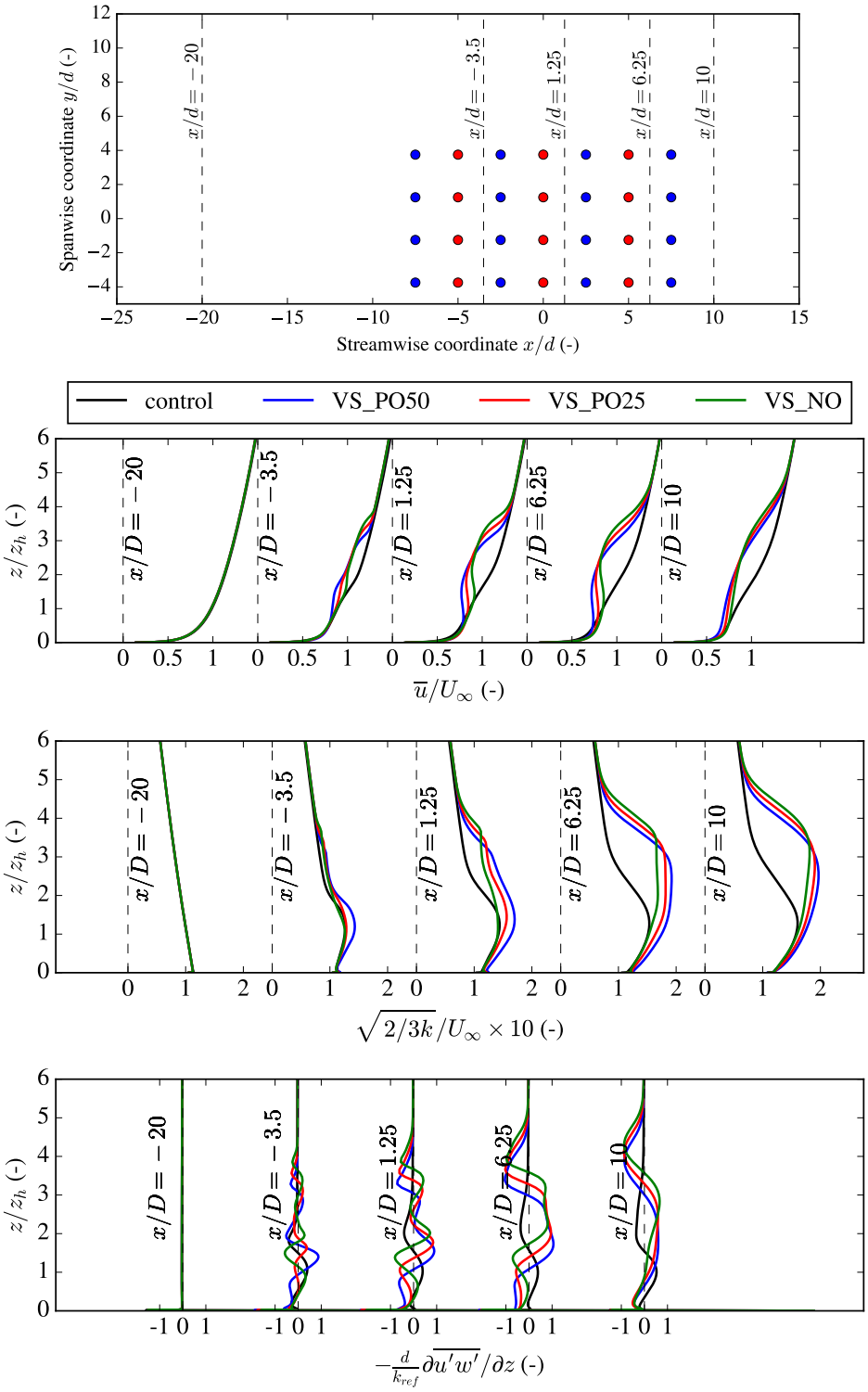

Figure 5.10: Spanwise-averaged velocity, TI and vertical stress divergence profiles computed in various streamwise locations. The normalised locations (x/d) are demonstrated in the top graph. The spatial averaging was taken over the wind farm width.

5.4.4 Energy yield comparative assessment

The preceding subsections revealed several interesting flow phenomena, resulting from installing larger-scale turbines into the control wind farm, shown in Figure 5.1. The hub height of the large turbines seems to have considerable impact on the flow, while the flow properties in VS configurations remarkably deviate from the control wind farm. This subsection aims to quantify these aspects through a comparative assessment focused on the power production of the smaller turbines. In the following paragraphs, the analysis identifies individual turbine patterns and subsequently, the discussion is extended to a wind farm level.

5.4.4.1 Column-wise power variability

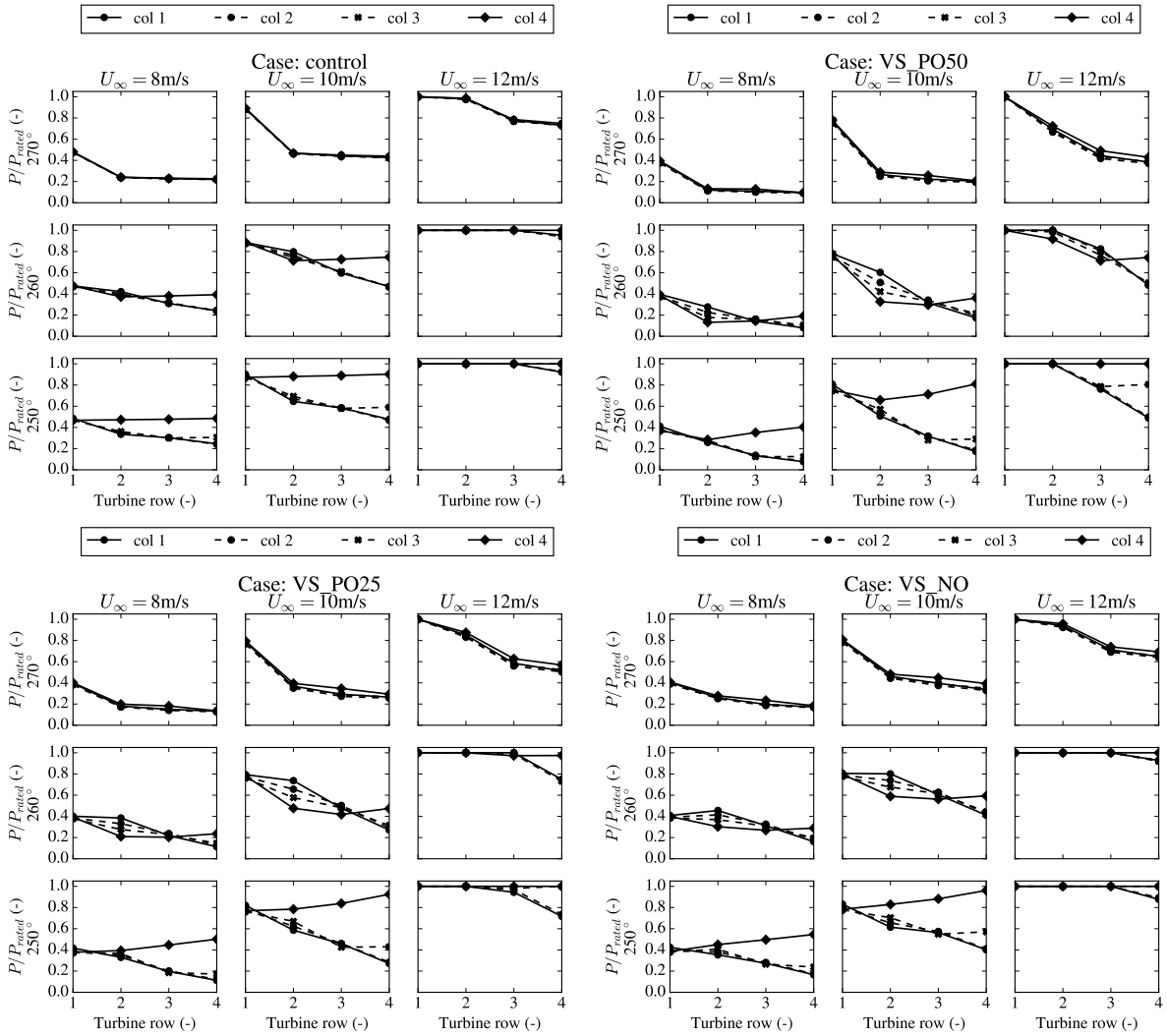

Figure 5.11: Column-wise power variation of the smaller turbines for various wind speeds (below and above rated) and wind directions (main wind direction and at an angle). Turbine power is normalised with the rated power of the small turbines (P_{rated}).

In the preceding discussion, the flow was found asymmetrical around the longitudinal axis of the wind farm, particularly in the wind farm wake, owing to the Coriolis-induced wind veer effect. This is expected to cause power variations between the turbine columns in the wind farm. Figure 5.11 illustrates the column-wise power variability of the small turbines in each wind farm configuration. Turbine power is plotted for two wind speeds below rated, namely 8, 10 m/s, one above rated, 12 m/s, and three different wind directions i.e., 250, 260, 270 degrees (see Figure 5.2).

In the main wind direction i.e., 270°, the effect of Coriolis on the power of individual turbines can be isolated; The previously mentioned cumulative effect of the larger-scale turbines' hub height and Coriolis is visible in the last turbine rows. The power production of the very top column (col 4) in the most downstream row is slightly improved, due to the flow acceleration witnessed in that region; This effect is insignificant in the control case, whereas is small yet noticeable in VS configurations.

In non-aligned cases, the power variability is rather dominated by the absolute wind direction of the incoming flow i.e., the angle between the flow direction and the $x-$axis. Coriolis forces and thus wind veer refer to rotations with respect to the absolute wind direction, which are nevertheless less influential on the power compared to the depicted absolute wind directions.

5.4.4.2 Effect of hub height on turbine power production

The previous discussion revealed a power variability in each turbine column of the wind farm, highlighting the high correlation between this variability and the wind speed of the free stream and the absolute wind direction. In order to obtain a more universal comparison between the power distribution of the small turbines in the different simulated configurations, averaged quantities were considered. In particular, the power of each row is obtained by averaging over all columns, as visualised in Figure 5.12.

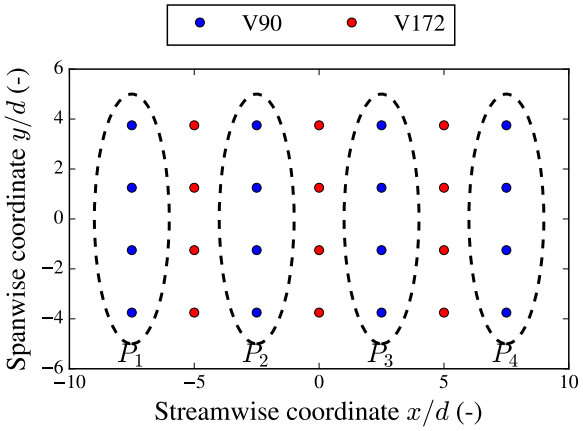

Figure 5.12: Schematic of the power averaging over turbine columns.

A comparative assessment of the column-averaged power produced by each turbine row was conducted. The aim is to quantify how the hub height of the larger turbines (and thus the geometrical overlap) impacts the power production of their smaller counterparts. Similarly to the discussion provided previously, the results of this analysis are presented for wind speeds below rated 8, 10 m/s and above rated, 12 m/s. A broader wind direction range is analysed, namely from 270 to 210 degrees in two 30-degree increments, in order to identify the effect of wind direction on individual turbine power. In Figure 5.13, the average power is normalised by the rated power of the small turbines, hence an estimate for the absolute power evolvement in the downstream direction can be obtained.

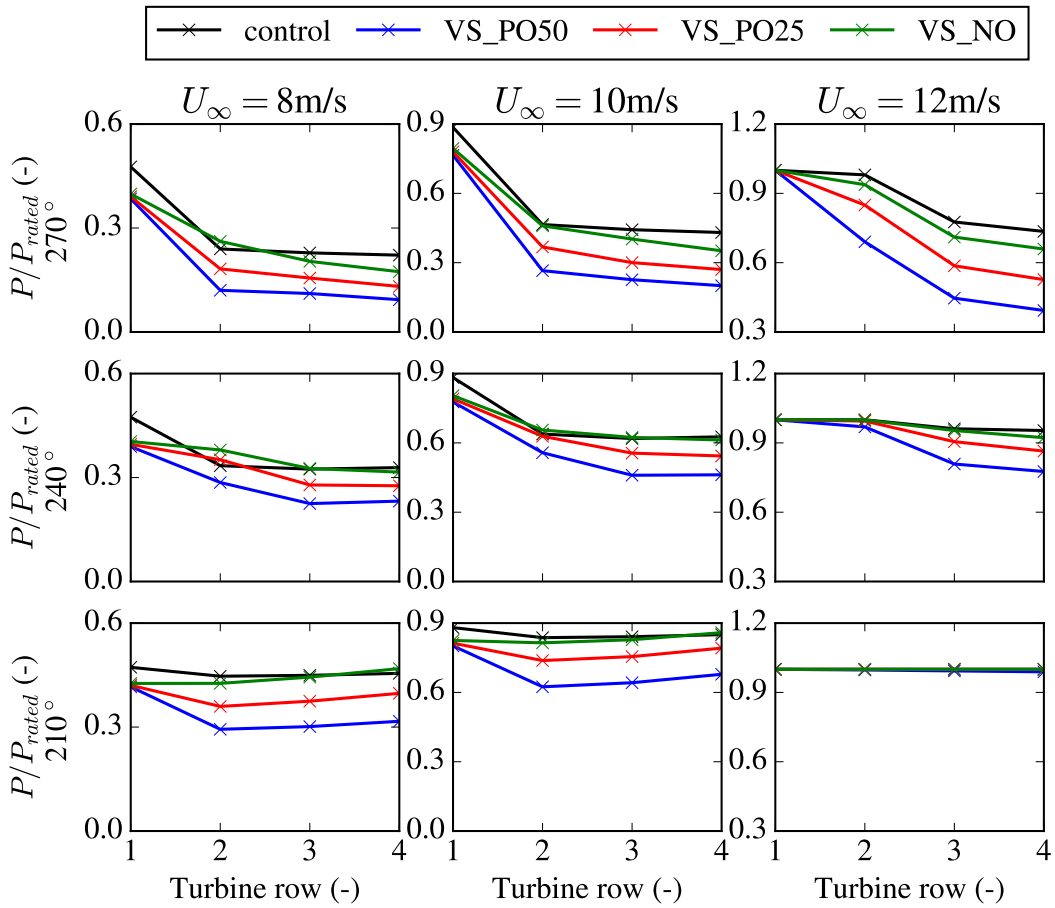

Figure 5.13: Comparison of turbine power, averaged over turbine column, for various wind speeds (below and above rated) and wind directions (main wind direction and at an angle). Turbine power is depicted only for the smaller (baseline) turbines and is normalised with the rated power (P_{rated}).

For the first row of turbines, the power losses in vertically-staggered configurations are more pronounced at wind speeds below the rated level due to enhanced blockage compared to the control wind farm. These losses are particularly significant at 8 m/s,

where the effects of vertical staggering are most evident. At 10 m/s, however, the turbines operate closer to their rated power, making the power production difference between the control and VS configurations less pronounced. When examining a fixed wind speed below rated, wind direction significantly impacts the power difference between VS and control arrangements. Specifically, as the wind direction deviates from 270°, where wake effects are maximized, the power output in the first row gradually improves for the VS cases. Interestingly, the VS cases perform similarly with one another in the first row, indicating that the studied hub heights do not have a strong influence on blockage and, consequently, on power drop in the first row. More extreme hub height variations are expected to cause larger power deviations in the first turbine row in the below-rated wind speed range.

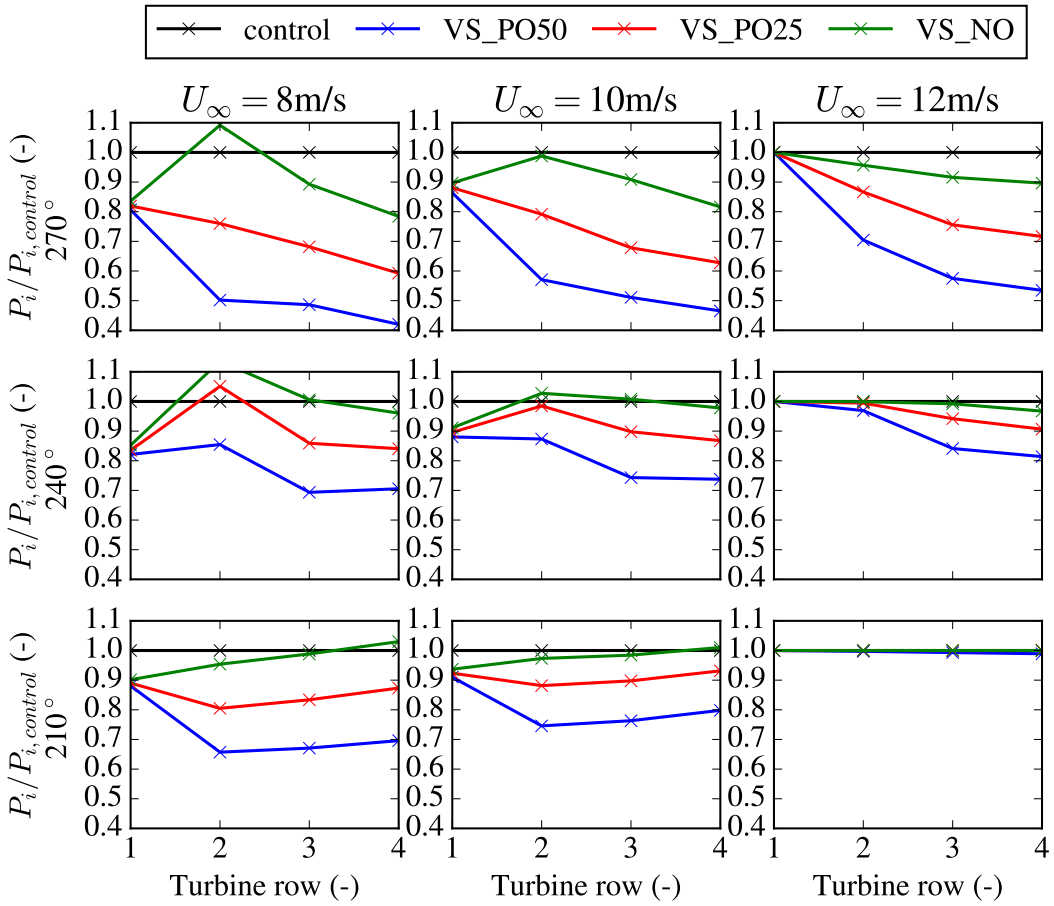

Figure 5.14: Comparison of turbine power, averaged over turbine row, for various wind speeds (below and above rated) and wind directions (main wind direction and at an angle). Turbine power is depicted only for the smaller (baseline) turbines and is normalised with the turbine power of the same turbines in the control wind farm ($P_{control}$).

Above the rated wind speed, the first row consistently produces nominal power, unaffected

by upstream effects. At 270°, where wake effects are maximized, only the first row operates at maximum power. However, as the wind direction deviates from this angle, the wake effects diminish, allowing more turbines to operate at their rated capacity. Furthermore, as the geometrical overlap decreases while assuming fixed wind direction and speed, the power output of each row tends to align closer with that of the control wind farm. Noticeably, at 240°, the power output of the smaller turbines in the VS_NO configuration is nearly identical to that of the baseline case. At 210°, all turbine rows produce maximum power, with the exception of the last row in the maximum overlapping case (VS_PO50).

For the rows located further downstream, the results are more complex due to the intricate wake interactions within the wind farm. Unlike the first row, the performance of downstream rows is strongly dependent on the hub height of the larger turbines. At a fixed wind speed and direction, increasing the hub height of the larger turbines reduces wake-induced losses. This is in agreement with studies in the literature [20], [64]. In some instances, the power output of the VS_NO configuration even surpasses that of the control wind farm. Those power gains are shifted increasingly towards the last rows of the wind farm when the wind direction is varied from 270deg, keeping the wind speed constant. The reason is that more downstream turbines are exposed to the undisturbed flow without being shaded by the large ones, therefore they can extract relatively more kinetic energy from the incoming air. Despite such occasional occurences where the VS configurations exceed the control wind farm in individual turbine power, the smaller turbines generally perform worse when collocated with larger ones in the VS configurations as demonstrated in Figure 5.14. This indicates that implanting new large turbines into an existing wind farm results in an energy redistribution, as previously reported by Chamorro et al. [11].

The current discussion focused on the power production of the small turbines individually. Several interesting observations were made, revealing the impact of the hub height of their larger counterparts. However, identifying patterns at a wind farm level is also of major importance.

5.4.4.3 Effect of hub height on wind farm power output

It is of interest to extract insights regarding the impact of the large turbines' hub height on the power production of the small turbines collectively i.e., at a wind farm level and to quantify the deviations from the control setup. To that end, wind farm power ratios were computed as,

$$\mathrm{PR} = \frac{P_{VS,i}}{P_{control}}\bigg|_{U_\infty,\mathrm{wd}} \tag{5.2}$$

$P_{VS,i}$ and $P_{control}$ represent the power output of the small turbines in the $i-$th VS configuration and the control wind farm respectively, for a certain combination of wind speed and direction. This allows quantification of the wind farm power percentage lost from the control setup due to vertical staggering, as well as to identify the relative differences caused by varying the hub height of the large turbines.

The results of this investigation are compared in Figure 5.15 for the entire wind direction range and the wind speeds considered in the preceding analyses. Maximum deviation from the control wind farm was observed around 270±20° for all cases. This trend holds for all depicted wind speeds. Hence, it can be concluded that the wake effects from the tall turbines are more influential around that wind direction range. The 270° angle is used as reference in the following discussion.

Below rated and when the tall turbines' hub height is minimum and thereby rotor overlap is maximised (VS_PO50), the power output drops to approximately 60% of that recorded in the control case at 270°. Halving the rotor overlap (VS_PO25), a roughly 15% improvement in wind farm power was observed relative to the aforementioned VS configuration. Notably, when the two rotor types are placed in a non-overlapping vertical alignment as in VS_NO, an additional 15% may be gained at 270°, producing around 10% less power than the control wind farm. This trend is consistent with the preceding findings concerning individual turbines.

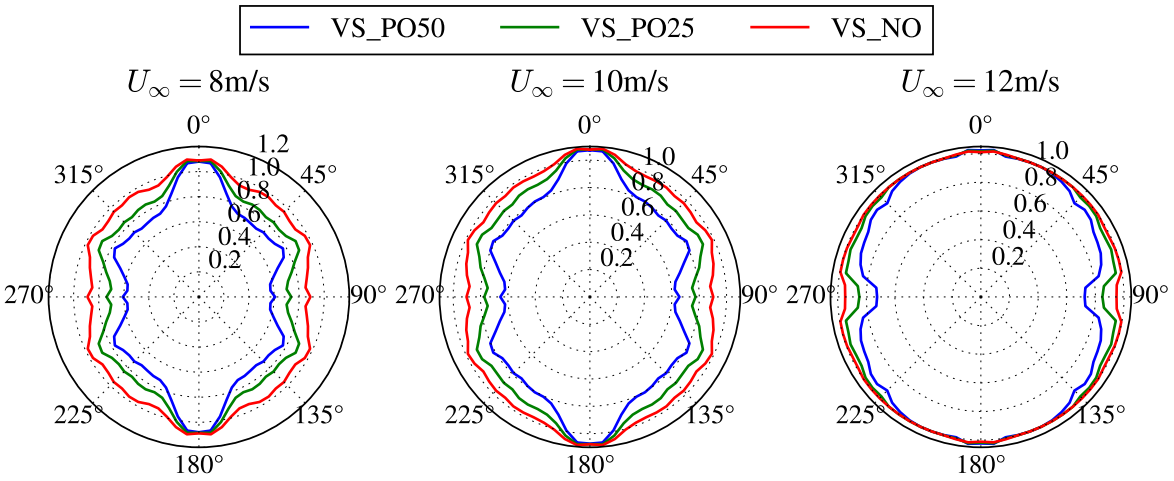

Figure 5.15: Wind farm power for VS configurations normalised by the wind farm power of the control wind farm. The results are presented for the full wind direction range and for wind speeds below (8, 10m/s) and above rated (12m/s). Power ratios are computed solely for the small turbines as dictated by (5.2).

At 270 degrees and above the rated wind speed, increasing rotor overlap leads the small turbines to operate below rated power for a wider wind speed range, while the deviations from the control setup are once again amplified. In general, VS_NO performs marginally differently from the control wind farm for most wind directions. In addition, for wind speeds significantly higher than the rated, turbine performance in all configurations is insensitive to wind direction, since all turbines have reached rated power. For absolute wind farm power figures, the reader is referred to Appendix B, Figure B.1.

Eventually, it can be concluded that in all three VS configurations, the small turbines generally produce less power than in the control wind farm in the majority of wind directions for all wind speeds, as anticipated. It is, hence, confirmed that local power gains in VS arrangements with respect to the control wind farm are not sufficient to exceed its total wind farm power. Interestingly, the power output of the small turbines is higher than in the control wind farm close to 0 and 180 degrees, where all VS configurations demonstrate almost identical performance.

5.4.4.4 Implications on Annual Energy Production (AEP)

It has been previously found that despite some local gains in the small turbines' performance, their aggregate production in VS configurations is lower than in the single hub height wind farm (i.e., control setup) for the majority of wind directions. However, this trend had some outliers specifically for 0 and 180 degrees, where the opposite effect was witnessed. Consequently, this requires further investigation of the wind farm performance universally.

To that end, a comparative assessment is conducted, with focus on the AEP. The calculations were carried out using a Weibull wind speed distribution with $A = 9.98$ m/s and $k = 2.03$ as seen in Figure 5.4, corresponding to the Høvsøre test site. In addition, a uniform probability was assumed for the wind direction. The results of the analysis are demonstrated in Figure 5.16.

It was found that erecting larger turbines into the already existing wind farm increases the total AEP of the wind farm by around 2.7 to 3.1 times with respect to the single-scale one (i.e., no large turbines). This significant AEP increase is recorded, due to the dominance of the larger turbines in power production; one reason is that they are exposed to stronger winds at high altitudes therefore there is more available power. A second reason is their remarkably higher capabilities in power production. To put into perspective the rated power of the large turbines is four times higher than the smaller ones. Nevertheless, it can be concluded that the large turbines experience diminished performance by increasing their geometrical overlap in the vertical direction with the small ones.

Despite the overall AEP increase for the current wind distribution the AEP of the smaller turbines, is negatively impacted by the presence of their larger counterparts. In particular, maximum rotor overlap in VS_PO50 causes a 11.5 percent AEP drop to the small turbines relative to the control wind farm, where no larger turbines exist. In the VS_PO25 configuration where the geometrical rotor overlap is decreased, the wake-induced AEP losses reduce by approximately 5%, yielding 5.9% less AEP than the control setup. Eventually, another 4% of the AEP can be gained when the larger turbines are install such that they don't overlap vertically. Yet, the smaller turbines in the latter configuration are still not able to outperform the single hub-height setup. For absolute AEP and wake loss figures, the reader is referred to Appendix B, Figure B.2. The study concludes that optimal power production is achieved when rotor overlap is minimized or

eliminated entirely. However, other factors such as visual impact restrictions should be also taken into consideration for the choice of the hub height in wind farm planning and development processes.

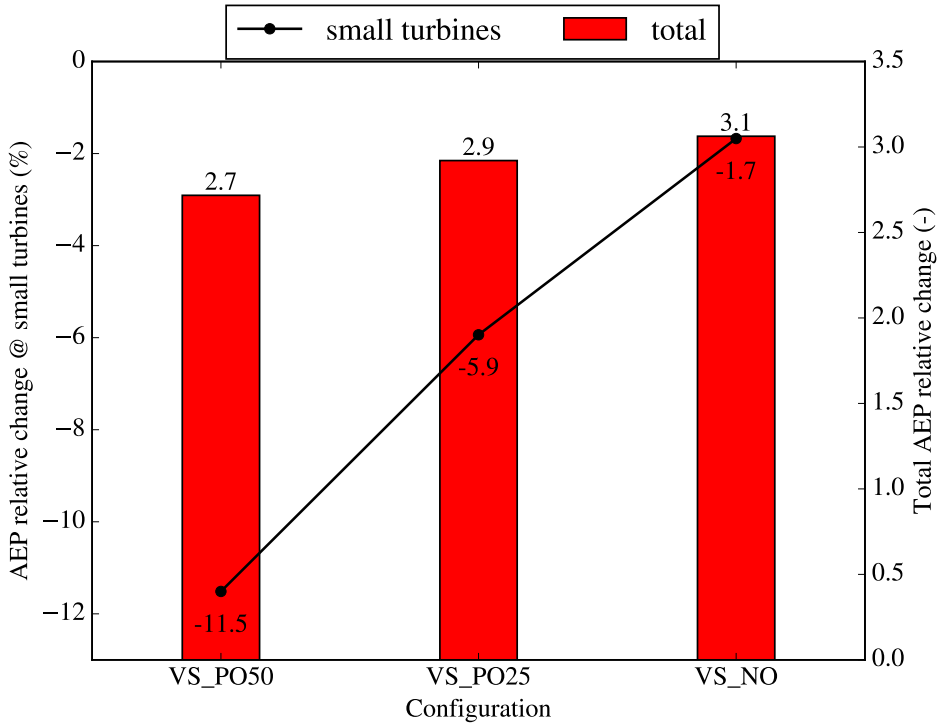

Figure 5.16: Relative change in AEP between control and VS configurations. The results are presented solely for the small turbines (black line) as well as for the entire wind farms, including the production of the large turbines (red bars).

Two final remarks should be made in relation to the hub height effect. Firstly, further hub height increases, such that vertical clearance is created between the two rotor types, are expected to induce flow acceleration above the small rotors and thus additional wake recovery, alongside the even more reduced inter-turbine wake interactions. Following the trend captured in Figure 5.16, it is hypothesised that the small turbines can exceed the control wind farm's AEP by further increasing the hub height difference. Secondly, in the extreme case that the hub height of the large turbines is increased infinitely in a fictitious VS arrangement, it is speculated that the smaller ones will perform as in the control wind farm since the rotor interactions between the two turbine scales will be eliminated. However, a detailed investigation is suggested, in order to examine the validity of these assumptions.

5.5 Summary & Remarks

The present chapter analysed and compared the flow field and power production trends between single-height wind farms and VS configurations by means of numerical simulations. The investigation focused on a simplified model indicative of German onshore wind farms. Three different VS arrangements are under consideration with BOR of 50, 25, and 0 percent respectively. The results demonstrate that erecting larger turbines (in rotor size and hub height) into an already existing wind farm consisting of smaller turbines impacts the flow properties and thus turbine performance. This impact is significant when the two rotor types overlap geometrically in the vertical direction. Some additional remarks are given below.

BOR formulation: In case a different rotor diameter ratio (d/D) between the two turbines is under investigation, assuming the same BOR then the wake interactions in the wind farm will deviate from the currently tested case and thus differences in power production should be expected. However, the BOR formulation does not take into account the tall turbine's rotor diameter.

Use of engineering wake models: Due to the lack of wind observations or higher-fidelity CFD data for the site studied in the present section, the use of engineering wake models (outlined in chapter 1) was not feasible. The RANS results could be employed for calibrating the wake models, yet, as demonstrated in chapter 4, they feature considerable limitations, mainly stemming from the eddy viscosity model assumption.

Sources of uncertainty: Some known sources of uncertainty stem from the eddy viscosity RANS model limitations. Furthermore, insights related to the uncertainty of the AEP calculations can be gained by performing sensitivity analyses on *1)* the wind direction resolution (currently it is computed in 5-degree increments), *2)* the grid error on AEP.

CHAPTER 6
Conclusion and outlook

The current research aimed to assess the reliability of a novel, RANS-based inflow model applied to wind farms and then use it to identify flow field and power production characteristics in vertically-staggered, onshore wind farms in Germany. The central questions dealt with in this research were as follows,

1. How do the velocity and TI predicted by the ABL-N model in large wind farms compare with LES-simulated results for different ABL heights?
2. How are the turbines of a control German onshore wind farm affected by the installation of additional larger-scale turbines in terms of flow phenomena and energy yield?

6.1 Main conclusions

The RANS wind farm flow field computed with the ABL-N inflow model was compared with the LES database of Lanzilao & Meyers [26] for two ABL heights in conventionally neutral boundary layer conditions. The results showed an overall overprediction of the velocity field in the induction and entrance region of the wind farm and an underestimation further downstream. The deviations from LES were in the order of 10%. A significant impact on the comparison have: 1) the differences in the AD method implementation, 2) the different ABL heights and 3) the presence of strong thermal effects in the reference dataset which was not resolved by RANS. The latter was less pronounced in the deep ABL case, consequently the velocity field was in better agreement with LES. The TI field was highly overpredicted by RANS, mainly due to the linear eddy viscosity model assumption. It was concluded that such a model cannot be fully relied on for quantitative analyses. Despite the outcomes of this study providing meaningful insights, selecting the novel model for further studies cannot be generalised and should be judged upon the objective at hand.

Subsequently, larger turbines were installed into an existing wind farm representative of a simplified model of the German onshore standards. Two partially overlapping rotor cases and one with no overlap were tested through hub height modifications. The resulting flow fields and turbine performance were compared to the single hub height arrangement. The study found that the collocation of multi-scale turbines introduces flow complexity, stemming from the inter-turbine wake superposition. Two competing effects were identified: the additional energy extraction from the large rotor and the

speedup regions between them. These highly influenced the performance of their smaller counterparts with the former being dominant when the rotors were partially overlapped. The coupling of Coriolis-induced wind veer and the hub height difference between the turbines also induced flow heterogeneity. Enhanced turbulence levels were recorded in the VS wind farms, raising concerns about fatigues problems. The exact numbers predicted are, however, questionable due to the turbulence model limitations mentioned previously. Despite the overall energy yield increase in all three VS configurations, the AEP of the smaller turbines was negatively impacted by the presence of their larger counterparts. Decreasing the rotor overlap improved their AEP; individual turbine performance in the non-overlapping setup was locally higher than the control wind farm, yet it remained below the one computed in the control. It is hypothesised that the small turbines in VS configurations can exceed the control wind farm's AEP by further increasing the hub height difference, yet detailed research is suggested to verify the validity of this argument. The study concludes that wind farm designers must balance the trade-off between minimizing turbine overlap to reduce wake-induced losses and avoiding too high hub heights to limit potential visual impact issues.

6.2 Proposals for future research

Future research should focus on conducting a more fair comparison of the RANS results obtained with the ABL-N model against field measurements or LES data, particularly in the absence of gravity waves. Turbine performance and flow properties such as turbulent fluxes should be contrasted between LES and RANS. It is also recommended to compare RANS and LES within the same software to eliminate the impact of differing force methods. If this direct comparison is not feasible, the impact of force method deviations among the software can be estimated by comparing RANS and LES using identical inflows, such as a simple logarithmic ASL profile (i.e., in the absence of complex ABL thermal phenomena). Insights into the improvements offered by the novel model used in the present thesis can be gained by including the other RANS inflow models (reviewed in chapter 1) in the comparative assessment of chapter 4. Additionally, further investigation is needed to test the hypothesis regarding higher hub heights, specifically exploring whether small turbines in VS configurations can surpass the control wind farm's AEP by increasing the hub height difference.

APPENDIX A
Wind turbine specifications

Table A.1: Specifications of the IEA 10 MW RWT [9].

Item	Value	Units
Name	IEA 10 MW RWT	N/A
Rated Power	10000	kW
Rated Wind Speed	11	m/s
Cut-in Wind Speed	4	m/s
Cut-out Wind Speed	25	m/s
Rotor Diameter	198	m
Hub Height	119	m
Drivetrain	Direct Drive	N/A
Control	Pitch Regulation	N/A
IEC Class	IA	N/A

APPENDIX B
Performance in VS wind farms

B.1 Wind farm power

The present section provides an absolute wind farm power comparison for the small turbines as a supplementary part of subsubsection 5.4.4.3, where relative differences with the control arrangement are identified. Minimum efficiency is obtained around the main wind direction (270°) for all wind farm configurations. Decreasing the rotor overlap increases the wind farm performance, yet it is found that none of the investigated cases outperforms the control arrangement for the majority of the wind direction range. The only outlier is witnessed close to 180°. This feature requires further research. The overall variation of the normalised wind farm power is almost identical with wind direction for all tested wind farm configurations. Coriolis forces have negligible effect on wind farm power i.e., it does not cause asymmetries around the spanwise axis (0-180°).

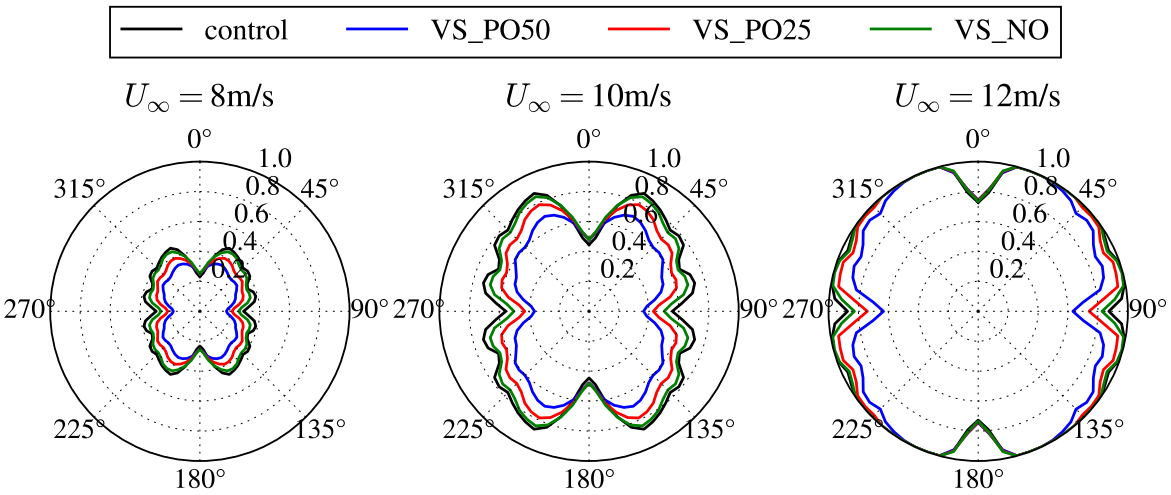

Figure B.1: Wind farm power for the simulated configurations normalised by the rated wind farm power. The results are presented for the full wind direction range and for wind speeds below (8, 10m/s) and above rated (12m/s). Power ratios are computed solely for the small turbines as P/P_{rated}.

B.2 Additional AEP results

The absolute numbers for AEP and wake losses for the small turbines and the entire wind farms examined, including the large turbines, are presented for reference. Wake losses

are defined as $1 - P/P_{\text{no loss}}$, wherein P is the computed wind farm power and $P_{\text{no loss}}$ represents the wind farm power without wake-induced losses, obtained from the power curve at the free stream wind speed at hand. The capacity factors can be computed from the AEP results; for the current wind resource input they are 0.49 for the control wind farm, and from 0.46 to 0.5 for the VS configurations for decreasing hub height. Therefore, the results show that despite the small turbines' performance drop, the resulting capacity factor in the VS_NO arrangement exceeds the control one.

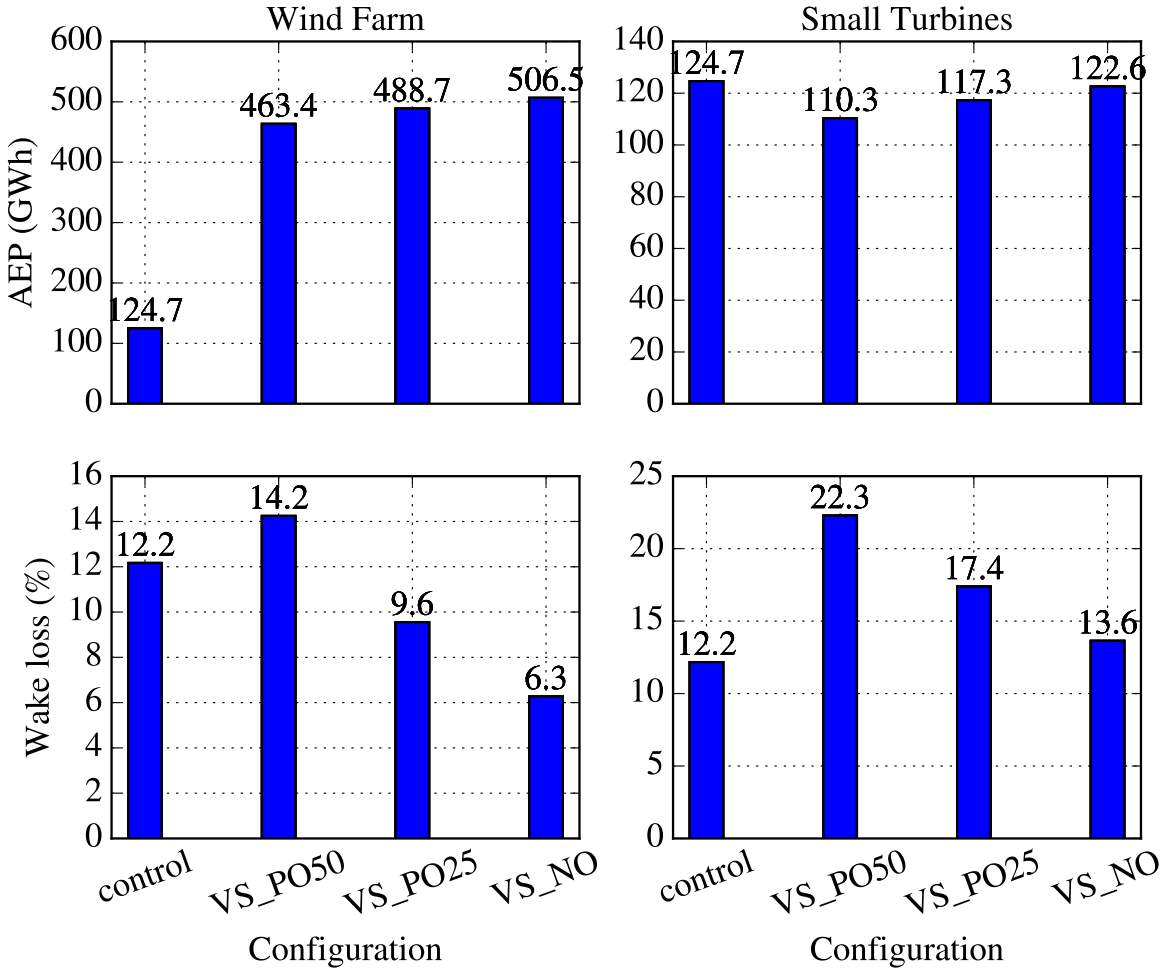

Figure B.2: AEP and wake loss comparison for all tested wind farm arrangements. Total wind farm numbers (left column) and solely for small turbines (right column).

Bibliography

[1] M Abkar and F. Porté-Agel. "The Effect of Free-Atmosphere Stratification on Boundary-Layer Flow and Power Output from Very Large Wind Farms". In: *Energies* 6.5 (May 2013), pages 2338–2361. ISSN: 1996-1073. DOI: 10.3390/en6052338. (Visited on March 11, 2024).

[2] D. Allaerts. "Large-Eddy Simulation of Wind Farms in Conventionally Neutral and Stable Atmospheric Boundary Layers". PhD thesis. November 2016.

[3] D. Allaerts and J. Meyers. "Boundary-Layer Development and Gravity Waves in Conventionally Neutral Wind Farms". In: *Journal of Fluid Mechanics* 814 (March 2017), pages 95–130. ISSN: 0022-1120, 1469-7645. DOI: 10.1017/jfm.2017.11. (Visited on February 26, 2024).

[4] I. Ammara, C. Leclerc, and C. Masson. "A Viscous Three-Dimensional Differential/Actuator-Disk Method for the Aerodynamic Analysis of Wind Farms". In: *Journal of Solar Energy Engineering* 124.4 (November 2002), pages 345–356. ISSN: 0199-6231. DOI: 10.1115/1.1510870. (Visited on August 5, 2024).

[5] D. D. Apsley and I. P. Castro. "A Limited-Length-Scale k-ε Model for the Neutral and Stably-Stratified Atmospheric Boundary Layer". In: *Boundary-Layer Meteorology* 83.1 (April 1997), pages 75–98. ISSN: 1573-1472. DOI: 10.1023/A:1000252210512. (Visited on February 15, 2024).

[6] M. Bastankhah and F. Porté-Agel. "A New Analytical Model for Wind-Turbine Wakes". In: *Renewable Energy*. Special Issue on Aerodynamics of Offshore Wind Energy Systems and Wakes 70 (October 2014), pages 116–123. ISSN: 0960-1481. DOI: 10.1016/j.renene.2014.01.002. (Visited on March 15, 2024).

[7] M. Baungaard. "Turbulence Modeling for Wind Turbine Wakes in Non-Neutral and Anisotropic Conditions". PhD thesis. Risø, Roskilde, Denmark: DTU Wind and Energy Systems, 2022. DOI: 10.11581/dtu.00000244.

[8] N. Bodini, J. K. Lundquist, and A. Kirincich. "Offshore Wind Turbines Will Encounter Very Low Atmospheric Turbulence". In: *Journal of Physics: Conference Series* 1452.1 (January 2020), page 012023. ISSN: 1742-6596. DOI: 10.1088/1742-6596/1452/1/012023. (Visited on July 29, 2024).

[9] P. Bortolotti et al. "IEA Wind TCP Task 37: Systems Engineering in Wind Energy - WP2.1 Reference Wind Turbines". In: (2019). DOI: 10.2172/1529216. (Visited on April 3, 2024).

[10] J. Boussinesq. *Théorie de l'écoulement tourbillonnant et tumultueux des liquides dans les lits rectilignes a grande section*. Paris: Gauthier-Villars et fils, 1897. (Visited on March 25, 2024).

[11] L. P. Chamorro, R. E. A. Arndt, and F. Sotiropoulos. "Turbulent Flow Properties Around a Staggered Wind Farm". In: *Boundary-Layer Meteorology* 141.3 (December 2011), pages 349–367. ISSN: 1573-1472. DOI: 10.1007/s10546-011-9649-6. (Visited on March 10, 2024).

[12] L. P. Chamorro et al. "Variable-Sized Wind Turbines Are a Possibility for Wind Farm Optimization". In: *Wind Energy* 17.10 (2014), pages 1483–1494. ISSN: 1099-1824. DOI: 10.1002/we.1646. (Visited on December 15, 2023).

[13] T. Chatterjee and Y. Peet. "Exploring the Benefits of Vertically Staggered Wind Farms: Understanding the Power Generation Mechanisms of Turbines Operating at Different Scales". In: *Wind Energy* 22.2 (2019), pages 283–301. ISSN: 1099-1824. DOI: 10.1002/we.2284. (Visited on November 30, 2023).

[14] K. Chen et al. "Wind Turbine Layout Optimization with Multiple Hub Height Wind Turbines Using Greedy Algorithm". In: *Renewable Energy* 96 (October 2016), pages 676–686. ISSN: 0960-1481. DOI: 10.1016/j.renene.2016.05.018. (Visited on March 11, 2024).

[15] Y. Chen et al. "Wind Farm Layout Optimization Using Genetic Algorithm with Different Hub Height Wind Turbines". In: *Energy Conversion and Management* 70 (June 2013), pages 56–65. ISSN: 0196-8904. DOI: 10.1016/j.enconman.2013.02.007. (Visited on March 11, 2024).

[16] DTU Wind and Energy Systems. *PyWakeEllipSys v4.0*. https://topfarm.pages.windenergy.dtu.dk/cutt

[17] *Global Wind Report 2024*. April 2024. (Visited on July 31, 2024).

[18] T. Gögmen et al. "Wind Turbine Wake Models Developed at the Technical University of Denmark: A Review". In: *Renewable & Sustainable Energy Reviews* 60 (2016), pages 752–769. ISSN: 1364-0321. DOI: 10.1016/j.rser.2016.01.113.

[19] K. S. Hansen et al. "The Impact of Turbulence Intensity and Atmospheric Stability on Power Deficits Due to Wind Turbine Wakes at Horns Rev Wind Farm". In: *Wind Energy* 15.1 (2012), pages 183–196. ISSN: 1099-1824. DOI: 10.1002/we.512. (Visited on March 19, 2024).

[20] J. F. Herbert-Acero et al. "Linear Wind Farm Layout Optimization through Computational Intelligence". In: *MICAI 2009: Advances in Artificial Intelligence*. Edited by A. H. Aguirre, R. M. Borja, and C. A. R. Garciá. Lecture Notes in Computer Science. Berlin, Heidelberg: Springer, 2009, pages 692–703. ISBN: 978-3-642-05258-3. DOI: 10.1007/978-3-642-05258-3_61.

[21] G. D. Hess. "The Neutral, Barotropic Planetary Boundary Layer, Capped by a Low-Level Inversion". In: *Boundary-Layer Meteorology* 110.3 (March 2004), pages 319–355. ISSN: 1573-1472. DOI: 10.1023/B:BOUN.0000007248.42321.d5. (Visited on August 4, 2024).

[22] E. L. Hodgson et al. “Cross-Code Verification of Non-Neutral ABL and Single Wind Turbine Wake Modelling in LES”. In: *Journal of Physics: Conference Series* 2505.1 (May 2023), page 012009. ISSN: 1742-6596. DOI: 10.1088/1742-6596/2505/1/012009. (Visited on March 7, 2024).

[23] N.O. Jensen. *A Note on Wind Generator Interaction*. Report 87-550-0971-9. Roskilde: Risø National Laboratory, 1983.

[24] I. Katic, J. Højstrup, and N.O. Jensen. “A Simple Model for Cluster Efficiency: European Wind Energy Association Conference and Exhibition”. In: *EWEC’86. Proceedings. Vol. 1* (1987). Edited by W. Palz and E. Sesto, pages 407–410.

[25] L. Lanzilao and J. Meyers. “A Parametric Large-Eddy Simulation Study of Wind-Farm Blockage and Gravity Waves in Conventionally Neutral Boundary Layers”. In: *Journal of Fluid Mechanics* 979 (January 2024), A54. ISSN: 0022-1120, 1469-7645. DOI: 10.1017/jfm.2023.1088. (Visited on February 7, 2024).

[26] L. Lanzilao and J. Meyers. *A Reference Database of Wind-Farm Large-Eddy Simulations for Parametrizing Effects of Blockage and Gravity Waves*. December 2023. DOI: 10.48804/L45LTT. (Visited on February 9, 2024).

[27] G. Larsen. *A Simple Wake Calculation Procedure*. Report 87-550-1484-4. Roskilde: Risø National Laboratory, 1988.

[28] B. E. Launder and D. B. Spalding. “The Numerical Computation of Turbulent Flows”. In: *Computer Methods in Applied Mechanics and Engineering* 3.2 (March 1974), pages 269–289. ISSN: 0045-7825. DOI: 10.1016/0045-7825(74)90029-2. (Visited on May 19, 2024).

[29] B. P. Leonard. “A Stable and Accurate Convective Modelling Procedure Based on Quadratic Upstream Interpolation”. In: *Computer Methods in Applied Mechanics and Engineering* 19.1 (June 1979), pages 59–98. ISSN: 0045-7825. DOI: 10.1016/0045-7825(79)90034-3. (Visited on August 27, 2024).

[30] T. Leweke et al. “Long- and Short-Wave Instabilities in Helical Vortices”. In: *Journal of Physics: Conference Series* 524.1 (June 2014), page 012154. ISSN: 1742-6596. DOI: 10.1088/1742-6596/524/1/012154. (Visited on August 5, 2024).

[31] C. Markfort, W. Zhang, and F. Porté-Agel. “Turbulent Flow and Scalar Flux through and over Aligned and Staggered Wind Farms”. In: *Journal of Turbulence [electronic only]* 13 (April 2012), page 13238. DOI: 10.1080/14685248.2012.709635.

[32] J. A. Michelsen. *Basis3D - a Platform for Development of Multiblock PDE Solvers: Beta - Release*. Report. Technical University of Denmark, 1992.

[33] S. V. Patankar and D. B. Spalding. “A Calculation Procedure for Heat, Mass and Momentum Transfer in Three-Dimensional Parabolic Flows”. In: *International Journal of Heat and Mass Transfer* 15.10 (October 1972), pages 1787–1806. ISSN: 0017-9310. DOI: 10.1016/0017-9310(72)90054-3. (Visited on August 27, 2024).

[34] J. G. Pedersen, S. E. Gryning, and M. C. Kelly. “On the Structure and Adjustment of Inversion-Capped Neutral Atmospheric Boundary-Layer Flows: Large-Eddy Simulation Study”. In: *Boundary-Layer Meteorology* 153.1 (2014), pages 43–62. ISSN: 0006-8314. DOI: 10.1007/s10546-014-9937-z.

[35] F. Porté-Agel, M. Bastankhah, and S. Shamsoddin. “Wind-Turbine and Wind-Farm Flows: A Review”. In: *Boundary-Layer Meteorology* 174.1 (January 2020), pages 1–59. ISSN: 1573-1472. DOI: 10.1007/s10546-019-00473-0. (Visited on November 17, 2023).

[36] F. Porté-Agel, Y. T. Wu, and C. H. Chen. “A Numerical Study of the Effects of Wind Direction on Turbine Wakes and Power Losses in a Large Wind Farm”. In: *Energies* 6.10 (October 2013), pages 5297–5313. ISSN: 1996-1073. DOI: 10.3390/en6105297. (Visited on March 11, 2024).

[37] J. M. Prospathopoulos et al. “Evaluation of the Effects of Turbulence Model Enhancements on Wind Turbine Wake Predictions”. In: *Wind Energy* 14.2 (2011), pages 285–300. ISSN: 1099-1824. DOI: 10.1002/we.419. (Visited on May 29, 2024).

[38] G. Rampanelli and D. Zardi. “A Method to Determine the Capping Inversion of the Convective Boundary Layer”. In: *Journal of Applied Meteorology and Climatology* 43.6 (June 2004), pages 925–933. ISSN: 1520-0450, 0894-8763. DOI: 10.1175/1520-0450(2004)043<0925:AMTDTC>2.0.CO;2. (Visited on November 17, 2023).

[39] P. E. Réthoré and N. N. Sørensen. “A Discrete Force Allocation Algorithm for Modelling Wind Turbines in Computational Fluid Dynamics”. In: *Wind Energy* 15.7 (2012), pages 915–926. ISSN: 1095-4244. DOI: 10.1002/we.525.

[40] P. E. Réthoré et al. “Verification and Validation of an Actuator Disc Model”. In: *Wind Energy* 17.6 (June 2014), pages 919–937. ISSN: 1095-4244, 1099-1824. DOI: 10.1002/we.1607. (Visited on February 28, 2024).

[41] A. Rogers, J. Manwell, and A. Ellis. “Wind Shear over Forested Areas”. In: *43rd AIAA Aerospace Sciences Meeting and Exhibit*. American Institute of Aeronautics and Astronautics. DOI: 10.2514/6.2005-1327. (Visited on August 11, 2024).

[42] C. J. Roy. “Grid Convergence Error Analysis for Mixed-Order Numerical Schemes”. In: *AIAA Journal* 41.4 (April 2003), pages 595–604. ISSN: 0001-1452. DOI: 10.2514/2.2013. (Visited on April 3, 2024).

[43] J. N. Sørensen et al. “Analytical Body Forces in Numerical Actuator Disc Model of Wind Turbines”. In: *Renewable Energy* 147 (March 2020), pages 2259–2271. ISSN: 0960-1481. DOI: 10.1016/j.renene.2019.09.134. (Visited on May 29, 2024).

[44] N. N. Sørensen. “General Purpose Flow Solver Applied to Flow over Hills”. Doctoral Thesis. Risø National Laboratory, 1995.

[45] N. N. Sørensen et al. “Identification of Severe Wind Conditions Using a Reynolds Averaged Navier-Stokes Solver: 2nd International Conference on "The Science of Making Torque From Wind"”. In: *Journal of Physics: Conference Series (Online)* 75 (2007), page 13. ISSN: 1742-6596. DOI: 10.1088/1742-6596/75/1/012053.

[46] R. J. A. M. Stevens, D. F. Gayme, and C. Meneveau. "Large Eddy Simulation Studies of the Effects of Alignment and Wind Farm Length". In: *Journal of Renewable and Sustainable Energy* 6.2 (March 2014), page 023105. ISSN: 1941-7012. DOI: 10.1063/1.4869568. arXiv: 1405.0983 [physics]. (Visited on March 11, 2024).

[47] R. B. Stull, editor. *An Introduction to Boundary Layer Meteorology*. Dordrecht: Springer Netherlands, 1988. ISBN: 978-90-277-2769-5 978-94-009-3027-8. DOI: 10.1007/978-94-009-3027-8. (Visited on July 9, 2024).

[48] R. B. Stull. *Practical Meteorology : An Algebra-based Survey of Atmospheric Science*. University of British Columbia, 2015. (Visited on February 27, 2024).

[49] P. Tavner et al. "Influence of Wind Speed on Wind Turbine Reliability". In: *Wind Engineering* 30.1 (January 2006), pages 55–72. ISSN: 0309-524X. DOI: 10.1260/030952406777641441. (Visited on July 9, 2024).

[50] N. Troldborg et al. "A Consistent Method for Finite Volume Discretization of Body Forces on Collocated Grids Applied to Flow through an Actuator Disk". In: *Computers & Fluids* 119 (September 2015), pages 197–203. ISSN: 0045-7930. DOI: 10.1016/j.compfluid.2015.06.028. (Visited on April 8, 2024).

[51] N. Troldborg et al. "Comparison of Wind Turbine Wake Properties in Non-Sheared Inflow Predicted by Different Computational Fluid Dynamics Rotor Models". In: *Wind Energy* 18.7 (2015), pages 1239–1250. ISSN: 1099-1824. DOI: 10.1002/we.1757. (Visited on February 8, 2024).

[52] M. P. van der Laan, S. J. Andersen, and P. E. Réthoré. "Brief Communication: Wind Speed Independent Actuator Disk Control for Faster AEP Calculations of Wind Farms Using CFD". In: *Wind Energy Science Discussions* (2019). ISSN: 2366-7621. DOI: 10.5194/wes-2019-27.

[53] M. P. van der Laan, M. Baungaard, and M. Kelly. "Brief Communication: A Clarification of Wake Recovery Mechanisms". In: *Wind Energy Science* 8.2 (February 2023), pages 247–254. ISSN: 2366-7443. DOI: 10.5194/wes-8-247-2023. (Visited on July 23, 2024).

[54] M. P. van der Laan, M. Baungaard, and M. Kelly. "Inflow Modeling for Wind Farm Flows in RANS". In: *Journal of Physics: Conference Series* 1934.1 (May 2021), page 012012. ISSN: 1742-6596. DOI: 10.1088/1742-6596/1934/1/012012. (Visited on November 17, 2023).

[55] M. P. van der Laan and N. N. Sørensen. *A 1D Version of EllipSys*. Report. 2017.

[56] M. P. van der Laan et al. "A New RANS-based Wind Farm Parameterization and Inflow Model for Wind Farm Cluster Modeling". In: *Wind Energy Science* 8.5 (May 2023), pages 819–848. ISSN: 2366-7443. DOI: 10.5194/wes-8-819-2023. (Visited on November 18, 2023).

[57] M. P. van der Laan et al. “A Simple RANS Inflow Model of the Neutral and Stable Atmospheric Boundary Layer Applied to Wind Turbine Wake Simulations”. In: *Wind Energy Science Discussions* (March 2024), pages 1–17. DOI: 10.5194/wes-2024-23. (Visited on March 19, 2024).

[58] M. P. van der Laan et al. “An Improved K-Epsilon Model Applied to a Wind Turbine Wake in Atmospheric Turbulence”. In: *Wind Energy* 18.5 (May 2015), pages 889–907. ISSN: 1095-4244, 1099-1824. DOI: 10.1002/we.1736. (Visited on February 2, 2024).

[59] M. P. van der Laan et al. “Fluid Scaling Laws of Idealized Wind Farm Simulations”. In: *Journal of Physics: Conference Series* 1618.6 (September 2020), page 062018. ISSN: 1742-6596. DOI: 10.1088/1742-6596/1618/6/062018. (Visited on November 17, 2023).

[60] M. P. van der Laan et al. “Predicting Wind Farm Wake Interaction with RANS: An Investigation of the Coriolis Force”. In: *Journal of Physics: Conference Series* 625.1 (June 2015), page 012026. ISSN: 1742-6596. DOI: 10.1088/1742-6596/625/1/012026. (Visited on March 27, 2024).

[61] M. P. van der Laan et al. “Rossby Number Similarity of an Atmospheric RANS Model Using Limited-Length-Scale Turbulence Closures Extended to Unstable Stratification”. In: *Wind Energy Science* 5.1 (March 2020), pages 355–374. ISSN: 2366-7443. DOI: 10.5194/wes-5-355-2020. (Visited on February 12, 2024).

[62] M. P. van der Laan et al. “The K-ε-fP Model Applied to Double Wind Turbine Wakes Using Different Actuator Disk Force Methods”. In: *Wind Energy* 18.12 (2015), pages 2223–2240. ISSN: 1099-1824. DOI: 10.1002/we.1816. (Visited on February 28, 2024).

[63] M. P. van der Laan et al. “The K-Epsilon-fP Model Applied to Wind Farms”. In: *Wind Energy* 18.12 (December 2015), pages 2065–2084. ISSN: 10954244. DOI: 10.1002/we.1804. (Visited on December 1, 2023).

[64] A. Vasel-Be-Hagh and C. L. Archer. “Wind Farm Hub Height Optimization”. In: *Applied Energy* 195 (June 2017), pages 905–921. ISSN: 0306-2619. DOI: 10.1016/j.apenergy.2017.03.089. (Visited on November 17, 2023).

[65] L. J. Vermeer, J. N. Sørensen, and A. Crespo. “Wind Turbine Wake Aerodynamics”. In: *Progress in Aerospace Sciences* 39.6 (August 2003), pages 467–510. ISSN: 0376-0421. DOI: 10.1016/S0376-0421(03)00078-2. (Visited on February 28, 2024).

[66] M. H. Vested et al. “Wake Interaction and Power Production of Variable Height Model Wind Farms”. In: *Journal of Physics: Conference Series* 524 (June 2014), page 012169. ISSN: 1742-6596. DOI: 10.1088/1742-6596/524/1/012169. (Visited on January 1, 2024).

[67] L. Wang et al. “Comparison of the Effectiveness of Analytical Wake Models for Wind Farm with Constant and Variable Hub Heights”. In: *Energy Conversion and Management* 124 (September 2016), pages 189–202. ISSN: 0196-8904. DOI: 10.1016/j.enconman.2016.07.017. (Visited on November 17, 2023).

[68] K. L. Wu and F. Porté-Agel. “Flow Adjustment Inside and Around Large Finite-Size Wind Farms”. In: *Energies* 10.12 (December 2017), page 2164. ISSN: 1996-1073. DOI: 10.3390/en10122164. (Visited on August 6, 2024).

[69] Y. T. Wu and F. Porté-Agel. “Large-Eddy Simulation of Wind-Turbine Wakes: Evaluation of Turbine Parametrisations”. In: *Boundary-Layer Meteorology* 138.3 (March 2011), pages 345–366. ISSN: 1573-1472. DOI: 10.1007/s10546-010-9569-x. (Visited on May 23, 2024).

[70] S. Xie et al. “Benefits of Collocating Vertical-Axis and Horizontal-Axis Wind Turbines in Large Wind Farms”. In: *Wind Energy* 20.1 (2017), pages 45–62. ISSN: 1099-1824. DOI: 10.1002/we.1990. (Visited on January 15, 2024).

[71] M. Zhang, M. G. Arendshorst, and R. J. A. M. Stevens. “Large Eddy Simulations of the Effect of Vertical Staggering in Large Wind Farms”. In: *Wind Energy* 22.2 (2019), pages 189–204. ISSN: 1099-1824. DOI: 10.1002/we.2278. (Visited on November 17, 2023).

[72] S. S. Zilitinkevich and I. N. Esau. “On Integral Measures Of The Neutral Barotropic Planetary Boundary Layer”. In: *Boundary-Layer Meteorology* 104.3 (September 2002), pages 371–379. ISSN: 1573-1472. DOI: 10.1023/A:1016540808958. (Visited on February 27, 2024).

{2.7182818284}ϑωερτυθιοπσδφγηξκλ